In the Wake of a Tidal Turbine

Samuel Miller Rose

Department of Mechanical and Aerospace Engineering

University of Strathclyde

A thesis presented in fulfilment of the
requirements for the degree of

Doctor of Philosophy

March 2018

Statement of Originality

This thesis is the result of the author's original research. It has been composed by the author and has not been previously submitted for examination which has led to the award of a degree.

The copyright of this thesis belongs to the author under the terms of the United Kingdom Copyright Acts as qualified by University of Strathclyde Regulation 3.50. Due acknowledgement must always be made of the use of any material contained in, or derived from, this thesis.

Signed: Date:

Abstract

Tidal energy is rapidly developing as a source of renewable energy. Horizontal axis tidal turbines are being installed in arrays, where device spacing is an important issue. Array performance will be affected as the flow from upstream devices (i.e. the wake) interacts with downstream devices. Further experimental data is necessary to understand the characteristics of turbine wakes, in particular the wake far downstream.

This work describes a series of physical tests undertaken to characterise the wakes of scale model tidal turbines. An Acoustic Doppler Velocimeter (ADV) is used to profile the wakes of two turbines operating in six configurations: varying tip speed ratio, blade number, and including a device with contra rotating rotors.

The wakes of various turbine configurations are mapped using velocity and turbulence data. Evidence of the wake can still be detected twenty five diameters downstream of the single rotor device, further than some literature suggests. If this is replicated on full scale devices in sea, this may impact the necessary spacing of devices within an array, or the performance of downstream devices.

Evidence is found of rotational structure in the wake at eight diameters downstream. This is further than is suggested in most literature. The wake from the contra rotating device recovers faster than the wake from single rotor devices, and the rotational aspect of the near wake is diminished. Thus a contra rotating device could be used advantageously to give a smaller wake footprint for a given amount of power captured. This could allow a more efficiently packed array, increasing the performance of the array over a given area.

Acknowledgements

I would like to record my thanks to my supervisors, Cameron Johnstone and Andy Grant. They provided invaluable guidance and assistance throughout, and I am indebted to them both.

Tom McCombes contributed a number of ideas to this thesis, Stephanie Ordonez kindly allowed the use of her turbine (Chapter 6), and Katie Gracie furnished me with papers when they were out of my reach. Equally valuable was their warmth, their conversation and their sanity.

John Redgate was always enthusiastic and willing to help, and offered much appreciated support in the flume tank, as did his colleagues in the Colville Building.

I am grateful to Andy Potter, who assisted me by proofing various sections. Chris Thomson went above and beyond in helping me to plot charts.

I would also like to express my thanks to EPSRC and SUPERGEN who provided funding for this research.

Finally, my wife has been a steady source of encouragement throughout; she means more to me than anything in this world and I owe her more than I can express.

Across the world so wide, the days go on unchanging;
The days go on unchanging, the dawn comes with the tide.

W.D. Cocker

Contents

List of Figures

Symbols and Abbreviations

Abbreviations	
ADV	Acoustic Doppler Velocimeter
BEM	Blade Element Momentum
CFD	Computational Fluid Dynamics
COR	Correlation
DC	Direct Current
DES	Detached Eddy Simulation
DNS	Direct Numerical Simulation
FFT	Fast Fourier Transform
LES	Large Eddy Simulation
NASA	National Aeronautics and Space Administration
NREL	National Renewable Energy Laboratory
PIV	Partical Image Velocimetry
RANS	Reynolds Averaged Navier Stokes
RMS	Root Mean Square
SNR	Signal to Noise Ratio
SODAR	Sonic Detection and Ranging
UK	United Kingdom

Symbols

A	Area
a	Axial induction factor
C_P	Coefficient of performance
C_T	Coefficient of thrust
D	Diameter
D_h	Hydraulic diameter
E	Energy spectrum
f	Frequency
Fr	Froude number
g	Gravitational acceleration
H	Height at which freestream velocity is reached
Hz	Hertz
I	Turbulence intensity
k	Mean kinetic energy
l	Characteristic length
m	Metre
$\dot{m}$	Mass flow rate
mm	Millimetre
n	Manning channel surface coefficient
p	Pressure
R	Rotor
r	Radius
Re	Reynolds number
S	Channel slope
s	Turbine seperation
St	Strouhal number
T	Thrust
T	Turbulence
t	Time
V	Velocity
v'	RMS of mean velocity fluctuations
W	Watt
w	Wake
x	Downstream direction
y	Cross stream direction; Distance from channel wall
z	Vertical direction
ε	Dissipation rate
κ	Wave number
λ	Tip speed ratio
μ	Dynamic viscosity; Uncertainty
ρ	Density
σ	Standard Deviation
ω	Rotational velocity
∞	Freestream

Chapter 1

Introduction

1.1 Tidal Energy

Recently there has been a significant focus on the development of new energy sources. This is spurred on by a desire to slow the increase of carbon dioxide emissions, and to reduce the reliance on fossil fuels by diversifying the energy portfolio. Various renewable energies have seen great advancement in their technological and economical feasibility, although few are mature. One such resource is tidal energy. Tidal energy, as its name suggests, is energy derived from the periodic movement of large volumes of water within the seas. These movements are regular and predictable, making tidal energy unique among renewable energies, increasing its desirability and speeding its development. This energy is of particular interest to the British government and market, as approximately 8 % of the world's tidal resource is situated in British coastal waters.

A working knowledge and understanding of the tides stretches back to prehistoric times. The earliest known use of tidal power comes from the 8th century A.D. and is located on Mahee Island in Strangford Lough, Northern Ireland. A pool was filled during the high tide and the water released in a controlled fashion to power a mill wheel. Aside from scale and power take off, the method used was the same as that used for present day tidal barrages. Tidal barrages are large, man made lagoons within the sea capable of maintaining a difference in water level from the surrounding sea. This head difference can then be exploited by using the kinetic energy derived from equalising the water levels to drive turbines and thus generate electricity. A well known example of an operational tidal barrage is that of the La Rance scheme, in France, constructed in 1966. Further such developments are possible, however they face significant obstacles, such as a sizeable ecological impact and large building costs.

Instead, a more acceptable method of harnessing tidal energy is found in the free turbine model. As opposed to the barrage model, which harvests and then forces the flow of water, the free turbine model makes use of the already existing flow of water. In this there is a clear parallel to conventional wind energy. Within the last twenty years, a wide variety of tidal devices have been proposed. Some of these have been tested at scale, whilst others have gone on to have prototypes tested. Unlike wind turbines, there is not a single, uniform design which has been settled on, and there is unlikely to be one as various devices will be best suited to different resource locations, depending on their strengths.

1.2 Example Devices

Three examples of devices are given below to illustrate the differing nature of designs. All three devices have undergone sea testing and further deployment is planned.

Atlantis

Atlantis resources operate a gravity based, three bladed device with an 18 m diameter rotor, and rated to 1.5 MW. The device has variable pitch and yaw so as to react to changing flow speed and direction during the tidal cycle. The

MayGen project installed four devices in Orkney in 2016, with the intention to install a further 53 devices over the coming years (Atlantis-Resources, 2018b).

OpenHydro

The OpenHydo device is unique in that the blades are located on the inside of the generator, and there is no hub as such (Open-Hydro, 2018). Instead, the stator and generator form a duct through which the flow is accelerated into the blades and the open centre. A 250 kW prototype was installed in Orkney in 2006; since then devices have been installed in France and Canada, and are preparing to install devices in Northern Ireland, Anglesey and Japan. Early iterations of the device have been mounted on two piles, and can be raised and lowered as required, however commercial projects remain fixed to the seabed.

CoRMaT

The Contra Rotating Marine Turbine (CoRMaT) is a contra-rotating tidal turbine designed by Nautricity (Nautricity, 2018). The device consists of two rotors, located on one shaft, spinning in opposite directions. CoRMaT is designed to be direct drive, avoiding the use of a gear box. The contra rotation provides torque balance over the system, eliminating the need for a rigid support structure. Instead, the device is positioned by floating it between an anchor and a buoy, allowing it to freely align with the flow direction. This allows a relatively easy installation and recovery process, making it ideal for deep water resources. Full scale commercial deployment is currently underway.

Although these devices are extremely different in their design and operation, and they may be suited to different types of tidal resource, they are similar in that each developer is using, or plans to use, individual devices as part of a larger array. To take advantage of economies of scale multiple devices will be situated together. This reduces the overall cost of location surveying, installation, cabling and grid connection. It also allows for the maximum utilisation of the high energy areas. Typically these areas are located around headlands and in channels, where the flow is constricted in some way, and the flow speed is higher than in the open sea. The number of attractive sites is limited, and there may be competition to obtain the rights to deploy in them. Furthermore, these areas are by definition limited in space, and so only a certain number of devices may be put in place. The number and positioning of devices is dependent on certain interlinked factors, and it is by no means clear that any standard solution has been given to this problem for any type of device.

The primary objective of any commercial project is to make money, and it is through this consideration that all other constraints are viewed. Money is to be made through the generation of electricity, so electricity generation should be maximised. The manufacture and installation of a device is a significant cost, but if each device added earns more revenue through electricity generation than it costs, then the number of devices should also be maximised. However, it is clear that with a finite resource there must be a point at which adding further devices will no longer increase profit. As each device is added it reduces the energy available to all other devices, by reducing the flow speed, thus reducing the amount of energy any following device may capture. Over a large enough area this reduction may be negligible, but in a channel, or if devices are close together, the impact will be noticeable.

1.3 Wakes

As each device interacts with the flow it leaves a footprint downstream, known as the wake. This may take the form of reduced velocity, increased turbulence or vorticity structures within the flow. A fundamental factor in the consideration of any array of tidal energy devices is the interaction between the wake of a device and the fluid intake of any device further downstream. This has the potential to have a major impact when assessing the economic viability of any proposed array. There are three main ways in which the wake can affect any downstream device:

- A reduction in velocity – this may lead to less power capture.
- An increase in turbulence – this may lead to greater loadings on the device, potentially increasing maintenance costs and shortening the lifespan.
- An intake flow that is significantly asymmetrical – this too may lead to greater loadings on the device, increasing maintenance costs and shortening the lifespan.

Aside from the economic ramifications of wake effects, environmental factors must also be considered. Any change in flow characteristics will impact the surrounding climate. Most plants and animals live within specific tolerances, and a change to flow velocity or turbulence may increase or decrease the survivability of a species. Through scouring of the seabed the local bathymetry may be changed.

The wake of a device is not permanent, rather it recovers as it travels downstream. It is gradually broken down by the surrounding flow until equilibrium is reached. The manner in which this occurs is dependent on the operation of the turbine device and the ambient flow conditions, and is of great interest as it will partly determine the placing of devices within an array. It is with this in mind that this study seeks to investigate the wakes of tidal energy devices.

1.4 Contra Rotation

Working under water presents particular challenges and opportunities. Because water is far more dense than air, devices can be designed which displace a mass equal to their own, i.e. the device can be made neutrally buoyant. This eliminates the need for a weight bearing support structure, though it does not eliminate the need for a station keeping device or a reactive torque to counter the rotation of the blades. If the station keeping is undertaken using firmly anchored mooring lines, the reactive torque can be generated using contra rotation. A contra rotating turbine is one where two sets of rotors are mounted on the same axis and rotate in opposite directions. The rotors are positioned close together, so that they act as a single hydrodynamic system. Applications of this concept can be found on ships, aeroplanes and helicopter rotors. Note that contra rotation is not to be confused with counter rotation, where rotors are mounted in parallel on separate axes.

Contra rotation will have five immediate advantages to it beyond that of eliminating the support structure.

- **Firstly**, for the cost of a second rotor the power output can be increased.
- **Secondly**, the rotation in opposite directions facilitates a direct drive generator, eliminating the need for a gearbox, thus reducing complexity and increasing reliability.
- **Thirdly**, the device can be deployed more easily in deep water or areas with difficult seabeds, as it does not require a solid structure on the seabed.
- **Fourthly**, the device is easily moveable and can be towed using a small boat simply by detaching the moorings. This allows maintenance and checks to be undertaken off site, reducing the need for expensive divers, ROVs or jack up barges, and reducing time lost waiting for suitable weather windows in which to operate.
- **Fifthly**, the lack of a support structure may reduce loading on blades due to shadowing (i.e. when the blade loading changes as it passes behind the

support structure (Frost *et al.*, 2014). This advantage may be offset by the different blade loading brought about when the downstream contra rotating blades pass behind the upstream blades.

Furthermore, there may be a **sixth** advantage. The wake of a contra rotating device is considerably less than the sum of two independently operating devices as the swirl imparted to the fluid by the rotation of the blades is lessened by the contra rotation. If this reduces the impact of the wake, the ability to maximise the resource captured by an array of turbines may be increased. For this reason it was decided to investigate the wake of a contra rotating device.

1.5 Choice of Method

Small scale experimental testing was chosen as the preferred method of testing. The alternatives were large scale testing and Computational Fluid Dynamics (CFD). Large scale testing would be testing on a scale approaching 1:1, and is the only method that would minimise the employment of assumptions and approximations. However, reasons for not undertaking large scale testing are quickly apparent when expense is considered, be it for a large scale flume, tow tank or in sea testing. Boat hire, blade manufacture and equipment would all be prohibitively costly for a wake study. Even if the cost of the device were to be excluded, and an already installed device were to be tested, achieving satisfactory measurement resolution for large scale devices would be difficult . A towed turbine must have some form of extension where the measuring device is also towed, a situation unfeasible beyond a few rotor diameters downstream. Any stationary device may have downstream instruments to take measurements (such as Acoustic Doppler Current Profilers) but these are expensive and difficult to move and reposition, meaning that a simple grid of 15x10 measurements would take multiple days or even weeks to obtain, whereas in a lab they could be taken in one measurement session.

A further consideration is repeatability, as in sea conditions the tide is never in a steady state; the flow velocity is always changing. An in sea experiment can be approximately re-run every 12 hours with each new tide, but even then the strength of the tide will vary throughout the tidal cycle, and an accurate repetition is only possible given a full month (depending on the tidal pattern at any given location).

CFD has been repeatedly used for assessing tidal devices, and can be a cheap alternative to physical testing. In addition, it offers considerably greater resolution, and modelling at scales smaller than is realistically possible for physical model testing. However, to fully capture the wake effects of a turbine using computational methods requires considerable computational power, and simplifications are generally made.

Two such simplifications are generally useful but limit the applicability of computational results. Turbulence is often approximated using models such as k-epsilon or k-omega. These are helpful in that they greatly reduce the computational cost of a simulation, but they are unable to fully represent the exact flow physics, and require verification and validation, which in turn require empirical data. The rotor of a device is often simplified using the actuator disk approach, replacing the spinning rotor with a porous disk of equal thrust. This is very desirable because the three dimensional modelling of a spinning rotor poses many challenges, such as the variation in scale needed to capture flow separation and stall on the blade surface compared to the large distances needed to map the far downstream wake. However, the use of an actuator disk does not account for the rotational aspect of the wake caused by a spinning rotor. This rotational aspect generally lasts through the near wake, and impacts wake breakdown and expansion. In addition to this, the actuator disk method may not fully capture the unique flow of a contra rotating device. For these reasons it was decided that small scale physical testing was the best choice considering the goals of the project.

1.6 Project Goals

There is a need for further understanding of turbine wakes, therefore this project sets out to map the wake of a tidal device. More specifically the following objectives are sought:

- **1.** To quantify the wake recovery of a generic device through three dimensional velocity and turbulence measurements. In particular to determine to what extent the wake can be detected far downstream.
- **2.** To compare the wakes generated by various different configurations of device, by altering variables such as rotational speed, blade pitch angle, and number of blades.
- **3.** To examine the wake of a contra rotating device, and compare it with that of a single rotor device. In particular to investigate the breakdown of the wake and the presence of rotation in the near wake.

These outcomes are to be set alongside comparable results from literature.

1.7 Outline of Thesis

The theory relating to the physics of a turbine wake is introduced in Chapter 2, and then a survey of pertinent literature is presented in Chapter 3. Two sets of experiments are undertaken, and the methodology for both is described in Chapter 4. The first makes use of a basic, generic turbine device. It is used to assess the effectiveness of the device in generating a wake comparable to that of a functioning tidal turbine and to provide a detailed picture of the wake. It is also used to appraise success of the method of data capture, and results are presented in Chapter 5.

The second set of experiments makes use of a more sophisticated generic device, which can be configured to represent a single rotor device or a contra rotating device similar to CoRMaT. The number of blades and the pitch angle of the blades can also be varied. Although no specific full scale device is held in mind, these experimental devices could be scaled to commercial sized devices via tip speed ratio and Reynolds number. The transition between the near and far wake is examined, and the far wake is scrutinised to ascertain the wake progression over a long distance, and investigate the wake breakdown. The wake of a contra rotating device is also examined. Ultimately the implications for array spacing are discussed. Results for this turbine are presented in Chapter 6. In Chapter 7 results from Chapter 6 are compared with those from Chapter 5, and then to similar experimental work found in literature. Finally, project conclusions are presented in Chapter 8.

Chapter 2

Wake Theory

This chapter introduces the theoretical aspects of the wake of a tidal turbine.

2.1 Turbulence

Turbulence is a notoriously complex phenomenon. It is often treated using empirical or semi-empirical relationships or assumptions which only hold for limited cases. Only a brief outline of turbulence will be given here due to the plethora of material available on the subject.

Turbulence is difficult to define, but can be described as irregular, diffusive, involving high Reynolds numbers, three dimensional, dissipative and continuous (i.e. of a continuum) (Tennekes and Lumley, 1972). It is a property of the fluid flow, as opposed to a fluid property. Whilst turbulence is not strictly a random process, it is often treated as such, using statistical rather than deterministic methods. It arises when a flow of sufficiently high Reynolds number is disturbed by some instability, and is maintained by taking energy from shear flow. Turbulence can be thought of as a continuum of eddies. Large eddies are generated which then bleed energy down to smaller eddies, which in turn lose energy to even smaller eddies, as per Richardson's famous poem. This process continues to a very small scale, where viscosity dominates and energy is dissipated as heat. As these eddies are part of the larger fluid flow, turbulence can also be thought of as fluctuations of velocity about the mean flow. These fluctuations occur at all wavelengths down to viscosity scale. Kolmogorov postulated that these fluctuations are independent of initial and boundary conditions, and are determined only by kinematic viscosity and rate of average dispersal of energy, ϵ (Scott, 2005). Furthermore, above the smallest scales viscosity can be neglected, so fluctuations depend only on ϵ, which in turn is dependent on the velocity and length scales (Tennekes and Lumley, 1972). Within the inertial subrange (above viscosity scale) the dissipation rate can be given as

$$E(\kappa) = \alpha \epsilon^{2/3} \kappa^{-5/3} \tag{2.1}$$

where $E(\kappa)$ is the energy spectrum, α is a constant empirically found to be about 1.5, κ is the wave number and ϵ the dissipation rate. This gives rise to a spectrum of energy dissipation, known as Kolmogorov's 5/3s law (Tennekes and Lumley, 1972). Thus

$$E(\kappa) \propto \kappa^{-5/3} \tag{2.2}$$

2.1.1 Scales

Eddy sizes are helpfully described by length, time or velocity scales (Tennekes and Lumley, 1972). The largest length scales, l_T, are determined by the channel diameter, and the smallest by viscosity. The velocity scale can be calculated as

$$V_T \approx k^{\frac{1}{2}} \tag{2.3}$$

where k is the mean kinetic energy in the turbulence,

$$k = 0.5 V'^2 \tag{2.4}$$

Thus the turbulence time scale can be found using the usual speed–distance–time relationship, where l_T is the hydraulic diameter (the ratio of fluid area to channel wetted perimeter,

$$t_T = \frac{l_T}{V_T} \tag{2.5}$$

and the turbulence Reynolds number can also be calculated.

$$Re_T = \frac{u_T l_T}{\nu} \tag{2.6}$$

2.1.2 Relevance to Tidal Energy

The in-sea fluid flows relevant to tidal energy are likely to be exclusively turbulent (rather than laminar), and this turbulence plays a number of roles within the subsea environment (Akwesivie, 2004). Additional turbulence created by a tidal energy device may have significant consequences to a number of areas, primarily due to its tendency to mix flows. **Salinity** generally varies vertically in the water column, depending on bathymetry and local current strength, and additional turbulence could facilitate the mixing of previously unmixed layers. **Temperature** also varies vertically throughout the water column, and certain organisms which only survive within a set salinity and temperature range may be affected by input turbulence. **Sediment** is lifted into the water column, depending on the strength of the current, and transported to less energetic areas or continually kept moving. If severe changes were to occur to the fluid dynamics then the local bathymetry and tidal patterns might change.

2.2 Flume Tank Hydrodynamics

Many flume channels operate within a turbulent regime. An open channel flow is one in which the balance of forces occurs between gravity and friction as opposed to the pressure forces of a closed pipe. This is because of the free surface, which equalises pressure to atmospheric at the topside of the fluid flow, but adds complexity by allowing variation in depth.

Open channels can be classified by depth change with respect to distance. They can also be classified by the Froude number, a number roughly equivalent to the Mach number, which determines whether the flow is sub or super critical. The Manning formula is frequently used as a correction for the friction in an open channel, given as

$$V = \frac{1}{n} Re_h^{2/3} S^{1/2} \tag{2.7}$$

Values of $n = 0.014 \pm 0.003$ for painted steel and 0.010 ± 0.002 for glass are offered in White (1994), where further discussion on flow inside an open channel can be found.

2.3 Turbine Wakes

2.3.1 Generating Power

Aside from the changed working fluid, in Bahaj *et al.* (2007) the differences between tidal energy capture and wind energy capture are highlighted as the array spacing, the existence of the free surface and the boundary proximity. The principles underlying the conversion of tidal energy into electrical power are shared with that of wind energy, and are well documented. Therefore a brief summary will suffice; for a more detailed explanation refer to Hansen (2008). A moving fluid exerts a force upon a rotor, causing it to rotate. This rotor extracts kinetic energy and transforms it into mechanical energy. This rotation is used to turn a generator – either by directly driving a shaft or through a gearbox – which then produces electrical power. As the device takes energy from the fluid, the flow downstream of the device is changed. The resultant flow is the wake, the focus of this study.

2.3.2 Actuator Discs

The development of the wake can be described in various ways, and one of the more common descriptions is that of the actuator disc theory. As it simplifies the system, so as not to require rotating components, it is popular for both physical and computational modelling (e.g. Myers (2005)). Fluid passing through a rotor imparts kinetic energy to it, and this energy transfer manifests itself as a drop in pressure. As the flow approaches the device the pressure begins to rise from freestream. Corresponding to this, and according to Bernoulli's equation, the velocity begins to decrease. Immediately upstream of the rotor the pressure reaches a peak, and drops to a low immediately downstream of the rotor. The velocity continues its gradual decrease, and because of the mass continuity equation (assuming incompressibility), the flow area expands,

$$\dot{m} = \rho A_1 V_1 = \rho A_2 V_2 \tag{2.8}$$

The pressure then gradually recovers to ambient pressure. In this way the rotor can be modelled as a porous disc, also known as an actuator disc. The pressure difference across the disc gives a force acting downstream. As the rotor is stationary, this force is of the same magnitude and opposite direction to the drag, or thrust, of the rotor,

$$T = A(p_w - p_\infty) \tag{2.9}$$

The thrust is non dimensionalised using the following equation, giving a thrust coefficient (Hansen, 2008),

$$C_T = \frac{T}{\frac{1}{2}\rho V_\infty^2 A} \tag{2.10}$$

The reduction in fluid velocity caused by the removal of energy is given by the axial induction factor (Myers, 2005) where V_R is the flow velocity at the rotor,

$$V_R = (1-a)V_\infty \tag{2.11}$$

Downstream the velocity is given as

$$V_w = (1-2a)V_\infty \tag{2.12}$$

Immediately behind the rotor, the velocity of the flow is given in Bahaj, Batten and McCann (2007) as

$$C_T = 1 - (\frac{V_w}{V_\infty})^2 = 4a(1-a) \tag{2.13}$$

Thus the thrust coefficient can be found from the freestream and wake velocities.

2.3.3 Near and Far Wakes

One difference between the actuator disc model and actuality is the latter results in the creation of a vortex system behind the turbine. As the fluid interacts with the rotor blades, vortices are formed from the trailing edge, the root and the tip of each blade (Hansen, 2008). The tip vortices are formed at the edge of the wake and form a boundary between the wake and the ambient flow; the root vortices form the core of the wake, staying in the axis of the turbine. Together these vortices form a helical structure rotating in the opposite direction from that of the rotor. This structure is coherent and discernible, but it does not remain so; its breakdown marks the splitting of two wake areas – the near and far wake

(Vermeer, Soerensen and Crespo, 2003).

The near wake is the area immediately behind the rotor, which is determined by the turbine geometry and determines the performance of the turbine; the far wake is the area downstream of this (Sanderse, 2009). In the near wake there is a discernible coherent structure within the wake, which begins to break down due to shear flow and ambient turbulence from the outside. When the breakdown of this coherence reaches the core of the wake, this signifies the beginning of the far wake. By this distance the wake has ceased expanding. A schematic of the wake is shown in Figure 2.1.

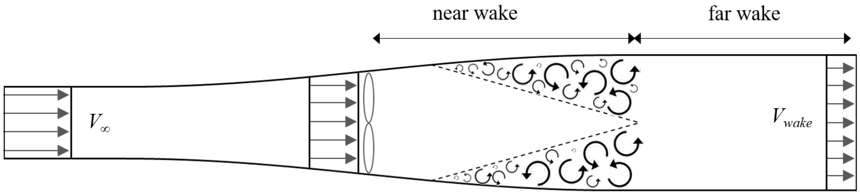

Figure 2.1: Wake of a tidal turbine

The actual distance at which this occurs is variable, and in wind turbine literature Schepers (2003) in Sanderse (2009) gives the expansion region length to be about 2.25 diameters (D), whilst a common approximation given for the end of the near wake is 2 – 5 D (Vermeer, Soerensen and Crespo, 2003).

According to Bahaj *et al.* (2007) the velocity within the wake is primarily (but not exclusively) dependent on the following parameters:

- Free stream velocity
- Turbine coefficient of thrust
- Ambient turbulence
- Depth of flow
- Rotor hub height

- Scale factor

The same paper notes that the most significant factor in the recovery of the far wake is the ambient turbulence.

Previously Ainslie (1988) demonstrated that an increased coefficient of thrust resulted in an increased velocity deficit within the wake. Additionally an increased ambient turbulence resulted in a decrease in the immediate velocity deficit.

2.3.4 Arrays

Myers and Bahaj (2005) mentions that the best tidal energy resources are concentrated around headlands or in straits, and arrays will be required to best harness the energy available. Tidal arrays will differ from wind arrays in spacing and layout, due to these resource constraints, but there is little technical experience of deployment. Wind turbine arrays are better understood. A modern wind farm sustains losses of 10 – 20 % due to wake interaction (Barthelmie *et al.* (2007) in Rethore, 2009), because of increased fatigue loading and decreased kinetic energy. Furthermore, any channel in which a blockage is placed will experience some kind of blockage effect, and this may be significant to any array deployed.

In Frandsen and Thøgersen (1999) the turbulence experienced at each turbine is suggested as

$$I^2 = I_\infty^2 + I_{added}^2 \tag{2.14}$$

where I_∞ is the ambient turbulence, and I_{added} is the turbulence added by the upstream turbine. I is given by

$$I = \sqrt{I_\infty^2 + \frac{1.2C_T}{s^2}} \tag{2.15}$$

where C_T is the coefficient of thrust, and s is the turbine separation in rotor diameters.

Myers *et al.* (2010) states that some of the most important factors to be considered in array deployment are the local current dynamics (including bathymetry and bottom roughness), individual device energy capture, installation access and station keeping. Arrays may be improved by offsetting the downstream devices so that they are not directly behind (i.e. share a centreline with) the upstream devices. This allows any downstream device to avoid some of the impact of the upstream device wake, thus increasing power capture.

2.3.5 Velocity Deficit

Velocity deficity is used (e.g. in Myers and Bahaj (2009a)) as a measure of the behaviour of a wake, and is defined as in Equation 2.16.

$$Deficit = 1 - \frac{V_w}{V_\infty} \tag{2.16}$$

2.4 Scaling

From the continuity and Navier-Stokes equations come three dimensionless numbers which are of use in hydraulic scaling: the Euler number, the Reynolds number and the Froude number (Sabersky, 1999). The Euler number is related to pressure and is only relevant when the absolute pressure, as opposed to the relative pressure, is of importance. As this is not the case for most incompressible flows (assuming cavitation is not present), the Euler number will not be considered here.

2.4.1 Reynolds Number

The most desirable method of scaling is Reynolds scaling. The Reynolds number is the ratio of inertial to viscous forces,

$$Re = \frac{\rho V D_h}{\mu} \tag{2.17}$$

Similarity in Reynolds number guarantees similarity in certain flow characteristics. For example, the onset of turbulence is solely dependent on Reynolds number, regardless of fluid or scale. To achieve Reynolds scaling when the scale is reduced, the density or velocity must be increased, or the viscosity reduced, in order to maintain similitude. This makes Reynolds scaling inappropriate for almost all conceivable scaled tidal turbine testing. Changing the density or viscosity would require a pressurised flume or a change in fluid, an impractical task for most test equipment. Increasing the velocity would require the rotor to operate at a very high rotational speed, resulting in significant blockage, blade stall and cavitation. Thus Reynolds matched scaling is rarely used for laboratory scale tidal testing. A concession is made to this parameter by ensuring that the flow falls within the same Reynolds number regime. When the critical Reynolds number is exceeded the flow will be turbulent in character. Both the scaled model and the prototype device should operate in a regime where this value is exceeded. However, this value is usually sufficiently low so as to pose no constraint on either laboratory or prototype testing, with both scales comfortably above the critical Reynolds number.

2.4.2 Froude Number

A further scaling parameter used in fluid dynamics is the Froude number, the ratio of inertial to gravitational forces of a submerged body,

$$Fr = \frac{V}{\sqrt{gl}} \tag{2.18}$$

The Froude number is analogous to the Mach number in that flows can be sub or supercritical ($Fr < 1$ or $Fr > 1$). A subcritical flow is one in which the wave velocity exceeds that of the flow velocity, and a supercritical flow is one in which the wave velocity does not exceed that of the flow velocity. The Froude number greatly influences the drag on objects at the free surface, and determines whether there is a hydraulic jump at any point. The shape of any free surface waves will be directly affected by the gravitational force, thus the Froude number plays an important role in their shape (Shames, 1962). Given that tidal flow involves a free surface, the Froude number is clearly relevant. However, if there is no surface piercing part of the device being tested, then there will be no 'bow' waves. Furthermore, if the flow is subcritical there will be no hydraulic jump, as hydraulic jumps can only occur in supercritical flow. In Bahaj and Myers (2013) it is noted that submerged objects are independent of Froude number when the channel Froude number is less than 0.25.

2.4.3 Strouhal Number

A further non dimensional number is the Strouhal number. This is used to describe the vortex shedding frequency of an obstruction in the flow,

$$St = \frac{fl}{V_\infty} \tag{2.19}$$

where f is the frequency of vortex shedding, D the characteristic length (the diameter in the case of a cylinder) and V the freestream fluid velocity (White, 1994).

2.4.4 Coefficient of Thrust

The coefficient of thrust is the non dimensionalised amount of energy removed from the rotor area and can be calculated using Equation 2.10. Similar thrust coefficients at different scales would be expected to produce comparable wakes.

2.4.5 Tip Speed Ratio

The tip speed ratio is the ratio of the blade tip velocity to the free stream velocity,

$$\lambda = \frac{\omega r}{V_\infty} \tag{2.20}$$

and is often used (e.g. Myers (2005)) in scaling rotating devices at a λ ratio of $1 : 1$ (i.e. by keeping the tip speed ratio the same in model and prototype). For any given blade geometry and blade number, the coefficient of performance is related to the tip speed ratio. The desired tip speed ratio is practical to implement, for any given flow speed the corresponding rotational speed can be determined and prescribed. The coefficient of thrust is a function of the tip speed ratio and the Reynolds number. As the far wake is a function of the coefficient of thrust, scaling by tip speed ratio and by Reynolds number is appropriate. Furthermore, for high Reynolds number flows the influence of the Reynolds number is low, as the Reynolds number inversely measures the effect of viscosity (Henderson, 1966). For regimes with a Reynolds number in the order of 10e6, the coefficient of thrust can become independent of the Reynolds number, being solely a function of the tip speed ratio (Mason-Jones *et al.*, 2012). By scaling using this parameter, some similarity with full scale modelling can be maintained at small cost of time or effort.

2.4.6 Acceptable Minimum Scaling

According to Myers and Bahaj (2009b) there is a minimum scale in which to work in order to keep acceptable levels of thrust and power. Any scaled model must be of sufficient size as to not be unduly influenced by surface tension, blockage, cavitation or fluid density.

2.4.7 Array Spacing

When considering array spacing it should be remembered that the decision is not purely one of wake recovery. For instance, local geography may mean that the ideal array in laboratory testing may perform differently on location. Limited space may exclude certain configurations. The positive use of blockage acceleration would be considerably harder to achieve in a bathymetrically varied environment. Furthermore, the device spacing must not be prohibitive for maintenance and installation access. Myers and Bahaj (2009b) gives a minimum of 240 metres as the distance required for vessel manoeuvring, which would correspond to 12 diameters for a 20 metre turbine.

Chapter 3

Literature Review

This chapter reviews literature relevant to the area of study, highlighting pertinent papers.

3.1 Resource Availability

Approximately 50 % of the Europe's tidal resource is dissipated around the British isles (BEIS, 2013). The main areas of resource concentration are as follows:

- Inter Island Channels
- Open Sea
- Headlands
- Sea Lochs
- Estuaries

The Significant Impact Factor (SIF) is a value ascribed to a location determining the amount of energy which can be exploited before there is a significant environmental or other impact. Some groups of sites are mutually exclusive, in that the same kinetic energy runs through different geographical points, and should not be counted twice. Polagye (2009) also notes that the energy capture within one strand of a multi branch estuary could be less than expected as the marine current turbines change the flow characteristics of the estuary.

Of the total energy present in the waters around the British isles, only a fraction can be expected to captured. An estimate by the Crow Estate (Crown Estate, 2012) estimates there is 95 TWhrs/year available to tidal stream devices (not including energy available for tidal barrage or lagoon schemes). This equates to power generation of 32GW. Main areas of resource are situated in the Pentland Firth, and locations on the West coast of Great Britain. Some areas of shallower water may prove less suitable for energy extraction when examined in detail, as exampled in O'Doherty *et al.* (2010). Most of the resource assessments undertaken have used navigational data, which is not the high resolution data required prior to deployment (Blunden and Bahaj, 2007). Thus there is a large amount of uncertainty, and the figures used come with a high level of uncertainty.

3.2 Wind Energy – Experimental

A near comprehensive review of wind turbine wake experiments between 1978 and 2003 can be found in Vermeer, Soerensen and Crespo (2003), which includes many of the papers mentioned in this section. Experimental work tends to be subdivided into laboratory testing and full scale testing.

3.2.1 Laboratory Testing

In Whale *et al.* (2000) particle image velocimetry (PIV) was used to examine the wake of a scale model wind turbine operating between tip speed ratio (λ) = 3–8 in a water channel. Wake expansion did not occur between $\lambda = 3$–4, but beyond this it took place immediately behind the rotor. At $\lambda = 8$ the device was operating in the turbulent wake state, meaning a high blockage. As was expected, the tip vortex spiral strength increased with λ.

In Kawahashi (2007) an array of 25 small wind turbines were tested in water, at low ambient turbulence, up to 31 diameters (D) downstream. Immediately behind a single device the velocity dropped to below zero, but was recovered to 90 % of the initial velocity by 20 D downstream. By about 10 D the flow within the wake was almost uniform and the turbulence had disappeared. When the array was tested areas of accelerated flow were found between the devices, but the flow had become uniform in velocity by 12 D downstream. It was suggested that the wake profile could be broken into three lateral sections: the inner region (wake), with an approximate velocity deficit of 0.6, the outer region (freestream) with a maximum deficit of 1.05, and an intermediate region between these where the deficit increased with radial distance from the core.

According to Massouh and Dobrev (2007) tip vortices are the most important feature of the near wake. Here PIV and hot wire anemometry were used to map the near wake vortex structure of a wind turbine operating at $\lambda = 3$.

The NREL study (Hand *et al.*, 2001) tested a large scale wind turbine at high Reynolds numbers in the NASA Ames test facility. Although most of the data gathered related to turbine performance, some small attention was also give to the near wake behaviour. The data is further examined in Schreck (2008). A similar project was undertaken in the Deutsch-Niederlandische Windanlage (Schepers and Snel, 2007). Detailed PIV measurements were taken from 1 D upstream to 1.25 D downstream of the device. Although both these projects are limited in their treatment of turbine wakes, they are important in that they are the only large scale tests conducted in laboratory conditions.

In Ebert and Wood (1997), Ebert and Wood (1999) and Ebert and Wood (2001) PIV was used to build an elaborate picture of the near wake of a two bladed turbine, and provided phase locked graphs of the flow velocity in the rotor area behind the blades.

It has been shown that after several rows of turbines the turbulence reaches an equilibrium, and there is a shift in the energy spectrum towards higher frequencies (Vermeulen PEJ (1982) in Vermeer, Soerensen and Crespo, 2003).

3.2.2 Full Scale Testing

In Magnusson (1999) a wind farm of four 180kW turbines was instrumented using two meteorological masts. These masts experienced time in and out of the turbine wakes depending on the prevailing wind direction. The coefficient of thrust was used instead of the flow velocity, as higher flow velocities exceeded the rated speed of the turbines, and stall regulation would stop the rotor from turning faster (thus limiting the energy extracted from the flow). Travel time was used instead of downstream distance. In the near wake, two peaks of velocity deficit were seen behind the mid-points of the blades. With increasing travel time these peaks merged into one peak in the centreline, at the end of the near wake. Travel time to the near wake end was inversely proportional to the rotational frequency of the turbine and ambient turbulence intensity, and proportional to the wake radius and hub height. For far wakes, the centreline velocity deficit decreased with the logarithm of time travelled, and was dependant on the travel time to the near-far wake transition and the coefficient of thrust. Two wakes combined had a lower velocity deficit than one on its own, as the travel time to the near-far wake transition of the second device was inversely related to the ambient turbulence intensity. This will have increased compared to the ‘true ambient’ turbulence due to the addition of turbulence by the upstream device.

In Barthelmie *et al.* (2003) wake measurements were taken at an offshore wind farm using sonic detection and ranging (SODAR). Measurements were taken in the wake of a turbine, then further measurements taken in the same position, having turned off the turbine. The wake deficit was clearly detectable, and its decay followed a relationship set out in Equation 3.1 (Magnusson and Smedman, 1996), when the correct roughness parameter was used

$$\frac{\Delta V}{V_\infty} = 0.4 \ln(\frac{t_0}{t}) + C_T \tag{3.1}$$

where t_0 was the timescale and t the travel time.

3.3 Wind Energy – Computational

In Sanderse (2009) some advantages are given for computational modelling over physical testing. In computational modelling devices can be tested at full scale, and the atmospheric conditions can be dictated easily. Array layouts can be changed and tested repeatedly, something almost impossible for most experimental regimes. However, the lack of accuracy when modelling turbulence is a disadvantage, and developing a mesh which can cater for the rotating blades in sufficient resolution is difficult.

A number of different options are available to those modelling turbine wakes. Direct numerical simulations (DNS) such as large eddy simulation (LES) and detached eddy simulation (DES) are accurate but come at great computing expense. Blade Element/Momentum (BEM) methods are simple and Vermeer, Soerensen and Crespo (2003) highlights them as the only approach used for the prediction of wind turbine performance and loading, due to accuracy and ease of use. However, they require empirical data and need corrections to deal with yawed flow or stall. In between these methods are Reynolds Averaged Navier Stokes methods, probably the most common tool employed for wake measurements. A plethora of models are used, making different assumptions appropriate for varying scenarios.

In Rethore (2009) designing a steady state wind farm wake model using computational fluid dynamics (CFD) is discussed. The author suggests Crespo, Hernandez and Frandsen (1999), Vermeer, Soerensen and Crespo (2003), Troldborg (2008) and Sanderse (2009) as a comprehensive summary of wind turbine wake modelling. It is also suggested that the k-epsilon turbulence method over predicts the near wake recovery compared to LES, both in the axial direction and the tangential direction.

In each of the four previously mentioned papers the work done in modelling wind turbine wakes is catalogued, with the latter two reviews showing a bent towards CFD.

In Baidya Roy, Pacala and Walko (2004) a very large scale array was approximated to investigate its impact on atmospheric dynamics. Although this study was preliminary and the array size larger than that of any current wind turbine arrays, it began an interesting line of thought of which the corollary will no doubt be developed in the tidal sector.

Myers *et al.* (2010) suggests that numerical simulations under predict the power loss within an array of wind turbines due to wake effects.

3.4 Tidal Energy – Experimental

3.4.1 Actuator Discs

In Bahaj and Myers (2013) a 1/15th scale model is tested to characterise the wake of a rotating device, and justify the use of actuator discs for array testing. Some differences between the two methods are noted. Because the swirl facilitates mixing, actuator discs have a greater velocity deficit in the near wake for the same value of thrust coefficient (C_T). The transition point from near to far wake is noted as between 5 and 6 D downstream, although it is anticipated that this will decrease in sea conditions, due to the higher ambient turbulence.

In Bahaj *et al.* (2007) some results of an actuator disc experiment are given. A 100 mm diameter disc was suspended in the water on a load cell, and wake measurements taken using an acoustic doppler velocimeter (ADV). The ambient turbulence was approximately 6 %. At 2.5 D downstream the velocity deficit was

> 0.6, and by 15 D downstream the deficit had reduced to 0.1. The centreline of the wake was noted to be below the centreline of the disc. When the free stream velocity was changed, the velocity deficit remained approximately constant.

Myers and Bahaj (2009a) investigates the effects of C_T, rotor depth and seabed roughness, on the wake of an actuator disc. In the far wake there was an insignificant difference between wakes of rotors with different C_T values. If the rotor was positioned low down in the channel it lacked flow under it to re–energise the wake further downstream, so the wake recovery was less. Similarly, if the seabed roughness was increased the fluid on the seabed was slowed down, and the same effect of a lack of re–energising flow under the wake was observed. This is an example of an increase in ambient turbulence not leading to an increased wake recovery. The authors suggest that a deficit of 0.1 or less would be an acceptable flow in which to position a downstream device in an array.

Daly, Myers and Bahaj (2010) investigates the flow effects of a tidal fence, and it is found that if the actuator disc was positioned close to the flume wall then the downstream deficit was decreased. It is suggested that this may be due to flow acceleration around the device increasing the shear between the wake and free stream velocities, thus dispersing the wake more quickly.

Sun (2008) details the testing of an actuator disc in a tow tank and an open channel, however, velocity measurements are limited to 6 D downstream of the disc.

3.4.2 Rotors

In Myers and Bahaj (2006) a 400 mm diameter rotor was tested. As this device operated at a high Froude number there were significant impacts on the depth of the flow downstream of the rotor. Immediately behind the rotor the depth decreased, whilst further downstream and upstream of the rotor there were small depth increases.

In Myers and Bahaj (2009b) the near wake of a tidal turbine was examined using an ADV. It is mentioned that previous work gave a recovery of 85 - 92 % by 15 - 20 D downstream. It is also mentioned that the swirl associated with the turbine blades was dissipated within 4 - 5 D, and was solely a feature of the near wake, although this has only been shown for wind turbines. A 0.8 m diameter, three blade turbine was used. The downstream flow was separately normalised against the free stream flow and the wake of the structure, with the latter giving a slightly reduced velocity deficit up to 6 D downstream where the effect of the structure ends and the wake deficit measurements converge. This method assumes the superimposition of the structural wake on the rotor wake. Unusually, the wake centreline rose in height by 0.1 D - other experimental work has recorded the maximum deficit below the rotor axis. However, this was likely due to structural interference.

Maganga *et al.* (2010a) describes further tidal turbine tests, examining a 700 mm diameter turbine performance and wake characteristics during different flow regimes. Both laser doppler velocimetry (LDV) and PIV were used to take wake measurements. Turbulence intensities of 8 % and 25 % were implemented, a horizontal velocity gradient was added and the distance from the hub to the free surface was varied. For different ambient turbulence levels, the turbine performance remains constant at low and medium tip speed ratios, though a higher turbulence intensity increased load on the turbine. For very high turbulence intensity the deficit is recovered to < 0.1 by 5 D downstream, but not until beyond 10 D for the low turbulence intensity. This high ambient turbulence intensity resulted in a faster wake recovery, and a narrower wake. Further results of the same experimental work regarding performance can be found in Maganga *et al.* (2009) and Maganga *et al.* (2010b).

Wake PIV examination of a small scale tidal device is outlined in Good *et al.* (2011), and the preliminary findings from the wake experiments of a device towed through Montgomery Lough are given in Rose *et al.* (2011). Both of these testing regimes are primarily focused on the near wake.

The influence of wake interaction within an array is discussed in Stallard *et al.* (2011), where physical tests were undertaken involving multiple devices. Velocity measurements were taken between 2 – 20 D downstream of a device running at $C_T = 0.82$, and significant deficit (0.12) was noted 20 D downstream. The individual wakes of three and five parallel devices were found to have merged by 8 D downstream.

In Stallard *et al.* (2013) experimental work investigates the effects of the free surface and boundary layer on turbine wakes. A 27 cm diameter rotor is tested in a flume 45 cm deep, with a flow velocity of 47 cm/s. Turbulence intensity varies within the flume from 10 % to 8 %, and velocity by 3 cm/s . Deficits were found to be 20 % and 10 % at 10 D and 20 D downstream respectively. The same paper gives experimental results for interaction between wakes of up to five turbines. The lateral spacing of turbines is shown to impact the wake behaviour when the spacing is 2 D or less.

Chen *et al.* (2017) examines the wake of a 3 blade, 30 cm diameter turbine. By 20 D downstream the velocity deficit had returned to within 5 % freestream, but the turbulence was 3 % higher than ambient turbulence. Rotation was noted in the flow to 4 D downstream.

3.5 Tidal Energy – Computational

The majority of predictions made about tidal turbine wakes are based on computational, rather than experimental, results. This is due to the relative cheapness of computational work compared to experimental, and the relative scarcity of available physical testing facilities.

3.5.1 Actuator Discs

In Myers (2005) a wind turbine blade element momentum (BEM) tool was used to create simple two dimensional and three dimensional models. This work was directed at rotor and turbine performance, but the data was used to inform an array simulation (Myers and Bahaj, 2005). In Harrison *et al.* (2009) the use of actuator discs is justified, and their application using a commercial CFD package is discussed. The CFD model gave acceptable agreement with experimental testing done on an actuator disc. As an example, for a coefficient of thrust of 0.8, the wake recovered to 90 % free stream by 20 D downstream. Blunden *et al.* (2009) simulates an array using a distributed roughness model and a CFD model.

Bai, Spence and Dudziak (2009) uses CFD to assess the impact of actuator discs on one another depending on their placement. The authors observed an increased performance in certain devices in the wake of others, due to flow accelerated through blockage (as predicted by Fraenkel (2002)), but it should be noted that blockage adds no energy, and momentum is conserved, so there was an overall net decrease in velocity in the wake. A trade off between increased performance due to blockage and wake recovery is suggested.

In Polagye (2009) it is noted that the shear effects from the channel bottom make a non-negligible difference to the wake recovery. For a device close to the bottom the wake recovered to 90 % of free stream by 20 D, but less than that for a channel of large depth.

Roc, Conley and Greaves (2010) offers a correction for the momentum sink turbulence method used in most CFD, as the latter over predicts the recovery of the wake. In Sun, Chick and Bryden (2008) the authors have used CFD to focus on the local effects of the energy extraction. The model was simulated in two and three dimensions. Immediately behind the device there was a drop in free surface height, and a corresponding increase in velocity above and below the device, with the expected decrease in the wake velocity. The device extracted 10

% of the available energy, and the wake velocity had returned to 80 % of free stream by 8 D downstream.

3.5.2 Rotors

In McCombes (2014) and McCombes, Johnstone and Grant (2009) a panel method is presented as a specific tool to model marine current turbine wakes. This code is then used to model tidal turbine arrays (McCombes, Johnstone and Grant, 2010).

O'Doherty *et al.* (2009) uses a commercial CFD package to model a contra rotating device, comparing it with a single rotor device. The increased thrust and the zero torque of the contra rotating device are noted. The overall wake recovery was similar for both devices (90 % after 15 D in shallow water and 90 % after 40 D in deep water) but the contra rotating device has a faster initial recovery. In the same set of simulations Willis *et al.* (2010) notes that when the rotors are placed close together in the contra rotating device, significant gains are made in the wake recovery (87 % wake recovery after 10 D downstream, compared to 52 % recovery for the conventional device at the same point). There is no mention of the effects on swirl within the wake.

Liu (2010) develops a panel method from screw rotor simulation, though the authors note a lack of experimental wake data to validate against.

Ebdon *et al.* (2016) compared two turbulence models with experimental testing, and concluded that though DES and RANS give similar results for performance, the DES model gives a closer match the the experimental work when considering wake recovery.

Currie, Osbourne and Grouix (2016) uses CFD to model a 3 blade turbine equipped with NREL S814 profile blades. The tip speed ratio is plotted against $C[T]$, giving a peak thrust at $\lambda = 4.5$, and a sharp drop in thrust for $\lambda < 3.25$ (which corresponds to experimental results given in Clarke *et al.* (2007)). Wake velocities are plotted to 20 D downstream. It is noted that for the higher $C[T]$ simulations (e.g. for $\lambda = 4.5$) the wake has not recovered by 20 D downstream.

3.5.3 Arrays

Myers *et al.* (2010) categorises arrays into first and second generation. A first generation array is a single or double row of turbines, whilst a second generation array is one which exceeds this. Assuming the first generation devices are offset from each other, only in second generation arrays do wake dynamics come to the fore.

Myers and Bahaj (2005) used wind energy modelling software to simulate a single turbine device, then extrapolated from this to design a large array in the Alderney Race. Devices were axially separated by 15 D based on previous work (Myers, 2005), and this distance is viewed by the authors as conservative.

In O'Doherty *et al.* (2011) an assessment is made of a four turbine array in various configurations, and a description is given of the effects of certain changes to spacing and positioning of turbines. By rotating a line of turbines in alternating directions the power coefficient is raised and the turbulence across the overall width is decreased.

In Malki *et al.* (2011) modelling of arrays is undertaken in CFD, and devices are spaced between 1 and 10 D apart. Complete recovery does not occur until almost 40 D downstream.

The benefits of situating arrays in constricted channels is explored in Smeaton *et al.* (2016). A constricted channel gives a higher power capture to number of turbines ratio, and the optimum place to place an array may be in the most constricted section of a channel due to blockage effects.

3.6 Blockage

Blockage effects are noted when the flow behind the turbine travels at speeds greater than free stream, having been accelerated around the rotor. Whilst obvious, it is important to note that this effect does not add any new energy into the flow, and the net energy downstream of the turbine must be lower than the energy upstream. The blockage ratio of a channel is the ratio of rotor area to the total cross sectional channel area, as defined in Equation 3.2,

$$Blockage\ Ratio = \frac{A_{Swept}}{A_{Swept} + A_{Free}} \cdot 100 \tag{3.2}$$

Chen and Liou (2011) outlines the concept of the blockage factor, which is used to determine the increase in a wind turbine's coefficient of performance, C_P, due to blockage in a wind tunnel. This is expanded in Mason-Jones *et al.* (2012) to give blockage factors for C_T and λ, where the blockage factor corrections are

$$C_{Tcorrected} = C_T(\frac{V_T}{V_\infty})^2 \tag{3.3}$$

and

$$\lambda_{corrected} = \lambda(\frac{V_T}{V_F}) \tag{3.4}$$

where V_T is the freestream velocity in the flume containing the blockage, and V_∞ is the freestream velocity in the empty flume.

In Whelan, Graham and Peiro (2009) a blockage correction for free surface flumes testing tidal devices is proposed, to be applied to BEM simulations. This correction is limited to low tip speed ratios, and has not been verified for low blockage ratios. The blockage caused by a rotor is a function of the blockage ratio and the power extracted from the flow. Chen and Liou (2011) suggests that no correction for blockage is required if the blockage ratio of a rotor is around 10

% or less.

Lartiga and Crawford (2010) gives a correction for blockage of actuator discs, involving only the coefficient of performance and the axial induction factor.

It has been suggested (Fraenkel, 2002) that blockage may act positively to increase the flow through a tidal turbine, but there has been little experimental work done to ascertain the practicality of this.

Myers, Bahaj and Germain (2008) notes that without a large blockage ratio and a high velocity there is unlikely to be any visible change in the surface elevation of the fluid. Furthermore, wake characteristics will be different depending on the proximity of the free surface and the channel bottom. If the flow depth is less than four diameters then the rate of recovery is reduced due to the mass flow beneath the rotor being inhibited by the bottom boundary layer. However, the acceleration around the rotor caused by a constrained flow helps to break down the near wake more quickly, thus facilitating faster wake recovery. Myers *et al.* (2008) finds that wake recovery is slowed when the rotor is located close to the bottom of the channel, but not effected when the rotor is in the middle or towards the surface in the water column.

Chapter 4

Experimental Methodology

This chapter outlines the design and setup of the two experimental testing regimes which were employed. In the first, a basic turbine model was run in a laboratory flume tank, whilst velocity measurements were taken in the wake. The equipment used, some challenges encountered, and the data capture process are all described, and the results are presented in Chapter 5. This device will be refered to as the Pile Mounted device.

In the second experimental testing regime, a 'wire hung' device was run in the same laboratory flume tank, with velocity measurements being taken in the wake. In this chapter the device is introduced and different configurations are discussed. Changes to the operating conditions of the flume and the data capture process are described. This device will be refered to as the Wire Hung device, and the results are presented in Chapter 6.

4.1 Pile Mounted Experiments

4.1.1 Pile Mounted Device

The first device to be used is shown in Figures 4.1 and 4.2. This is a generic device, not based on any specific technology, although it bears resemblance to many

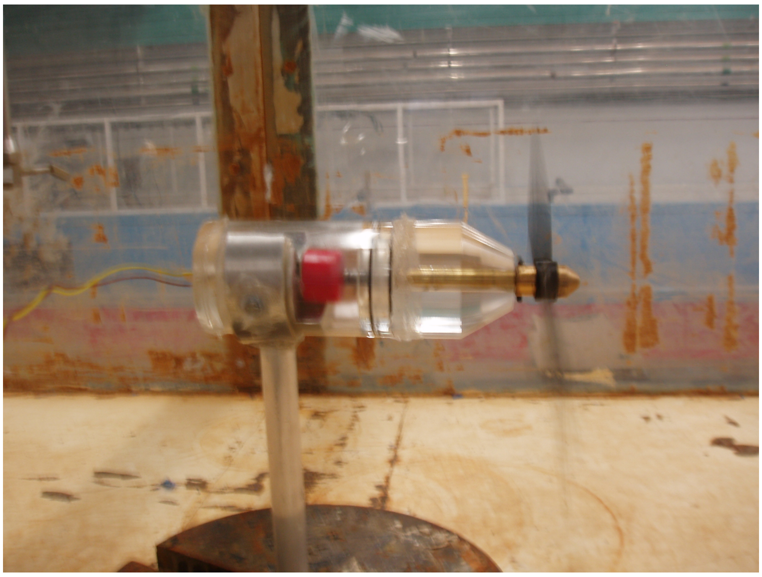

Figure 4.1: Pile mounted device in flume

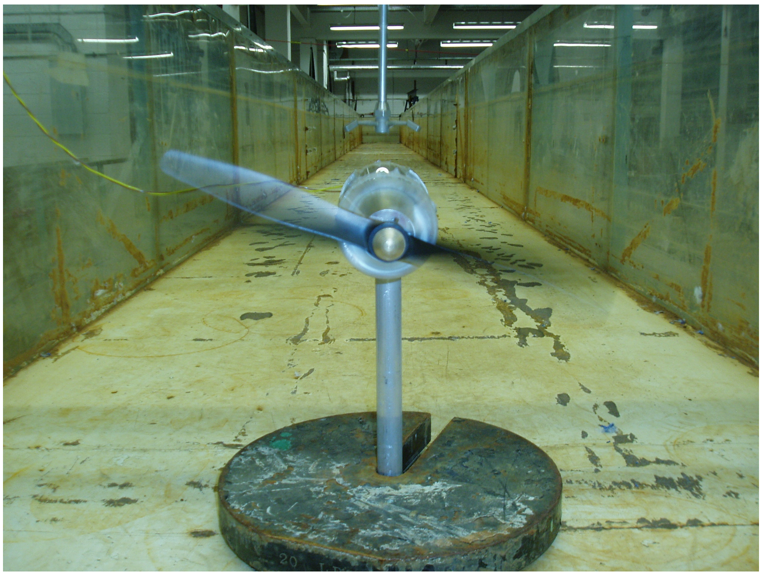

Figure 4.2: Pile mounted device in flume

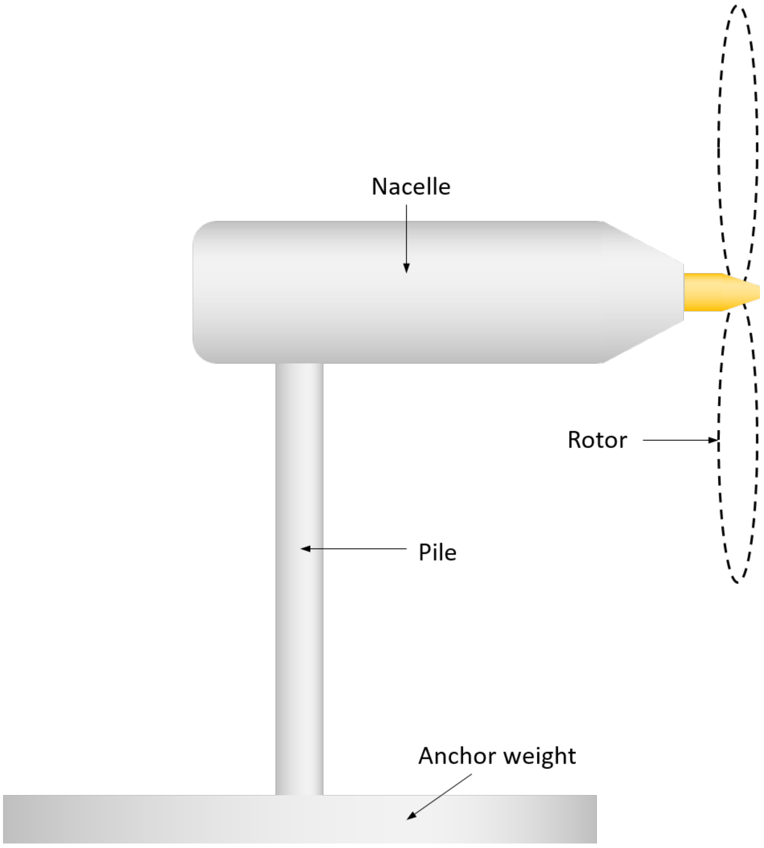

Figure 4.3: Pile mounted schematic, showing the location of the rotor, nacelle, pile and anchor weight

first generation tidal energy concepts in that it is a gravity anchored monopile structure, suitable for deployment in shallow waters (e.g. as described in Fraenkel (2002)). An aluminium strut held in place a Perspex housing, which contained a geared 5 volt DC motor. Station keeping was fulfilled using a solid weight on the base of the structure. A schematic highlighting the main parts of the device is shown in Figure 4.3.

The blade used was an inverted model aircraft propeller of 25 cm diameter. Using an inverted propeller in place of a turbine would considerably lower the performance of the device, with the trailing and leading edges, and the pressure and non-pressure sides swapped. However, the flow obstruction caused by the rotor would still generate a rotational wake for measurement (further experimental work using bespoke profiled rotor blades is discussed in Chapter 6). A device of

25 cm diameter gave a blockage ratio of 13 %. Given the presence of a free surface this was unlikely to cause significant blockage across the whole channel. Blade clearance from the top of the channel was 4.5 cm and 10.5 cm at the bottom of the channel, thus some localised blockage might be expected above the device, between the rotor and the free surface. The device position in the flume is shown in Figure 4.4.

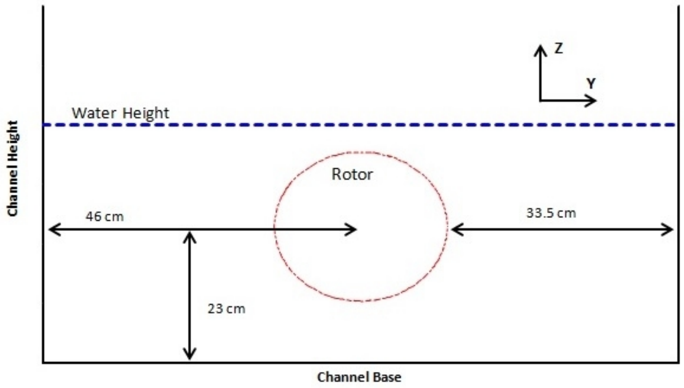

Figure 4.4: Schematic of pile mounted device position in the flume channel

The rotor was not free spinning, nor was it power generating (as per e.g. Doman *et al.* (2015)). The decision not to use a free spinning or power generating model was taken in light of the small scale of operation – the torque generated would be small, and would struggle to overcome the resistance of the shaft and motor. The rotational speed of the rotor would also be subject to variability from the turbulence in the flow, which would introduce further complexity in the wake models. Instead the blades were driven by the DC motor housed within the nacelle. This would provide the torque required to overcome the stiffness of the motor and shaft, and give a smooth and consistent rotation of the blades.

4.1.2 Tip Speed Ratio

During the first pile mounted experimental run, the primary variation of configurations was obtained by changing the tip speed ratio (the ratio of the speed of

Table 4.1: Exact tip speed ratio measurements

Measured λ	Rounded λ
3.03	3
3.99	4
4.96	5

the blade tips to flow speed).

The tip speed ratio, λ, is a non dimensional number which has been used for scaling when Reynolds number scaling is inappropriate (Doman *et al.*, 2015). λ is also related to C_T, in that it has a direct bearing on the thrust (Myers, 2005). Because the wake is directly linked to the thrust of the device, C_T is often used. Although C_T might be considered more instructive with regard to wake generation and development, λ is substantially easier to measure. As the blade used was an inverted propeller, the blade properties had not been defined through physical or computational testing and an approximation was made as to the likely peak of C_T for a given λ. In lieu of data on the performance of the rotors in their inverted configuration, tip speed ratio was chosen to align with other, similar experiments. Currie, Osbourne and Grouix (2016) gives a peak thrust corresponding to $\lambda = 4.5$, Stallard *et al.* (2013) uses $\lambda = 4.7$, Ebert and Wood (1997) gives an optimum $\lambda = 4$. These experiments encompass a range of blade types and flow speeds, therefore an initial value of $\lambda = 4$ was chosen for the pile mounted experiments, with sensitivities of ± 1.

The testing of round numbers of 3, 4 and 5 was subject to the ability of the operator to achieve the correct rotational speed, and the exact values were not achieved. The exact tip speed ratios tested are presented in Table , however throughout this text they are rounded to the nearest whole number. This rounding has been undertaken for ease of reference, and as the primary value of the testing lay in the qualitative relationship (i.e. higher or lower) between the three λ configurations.

λ was varied by altering the rotational speed of the blades rather than the flume flow speed (rotational speed was altered by varying the voltage supply). Any variation of the flume flow speed resulted in a change in water height within the flume, and the turbulence intensity within the flume, making it difficult to keep these variables steady.

A further set of tests examined the impact of the structure of the device by examining the wake behind the nacelle, pile and anchor. This was done by removing the blades from the device.

Although the test devices used in this work are not designed to model any specific full scale device, certain comparisons can be drawn. For λ similarity to be upheld a device of 18 m diameter in a fluid flow of 2 m/s would rotate at 8.5 rpm. This is comparable to Atlantis Resource's AR1500 rotor diameter of 18 m and rotational speed of 7–15 rpm (Atlantis-Resources, 2018a).

4.2 Wire Hung Experiments

4.2.1 Turbine Design

Although any full scale device was to be neutrally buoyant and tethered, it was not possible to make the scale model so. At small scales the balance of buoyancy in three dimensions was impractical and as the blades were free spinning a torque balance between rotors was also impractical. Furthermore, a tethered device would be constantly moving and adjusting itself to small variations in the flow. As measurements were taken as averages at stationary positions over a period of time any device movement would require a corresponding measurement movement, an impractical demand. Instead, the device was made slightly buoyant and secured with three wires and a strut so as to stop all movement apart from the rotation of the blades, as shown in Figure 4.5. A streamlined strut was suspended in the flume and attached to the nose of the device using a metal tie. At the rear of the device one wire was secured to a gravity based anchor and a further two wires secured to the near and far upper flume walls respectively (only one of the upper wires is shown in Figure 4.5 for clarity). By keeping these wires taut the device could be held rigid.

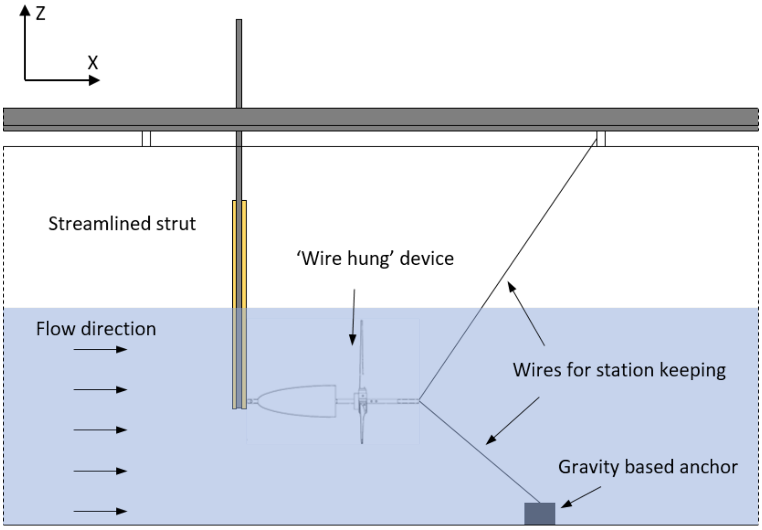

Figure 4.5: Schematic showing the support arrangement for the wire hung device

The blades used were NREL S814 profiles, with twist. They were constructed using a high resolution 3D printer, from Veroblue, an acrylic polyjet resin. Because this low strength material was used, the blades were prone to bending after repeated use. The blades were also prone to fracture at the root when subjected to high stresses. Due to the cheap manufacturing cost they were easily replaceable and regularly changed. The total diameter of the rotor was 30 cm. As can be seen in Figure 4.6 the device itself was made up of a shaft, a rotor hub and blades, and a nose cone. The rotor was held in place with a small collar. A spring brake can also be seen in Figure 4.6, but this was not employed, due to a lack of sensitivity. Two separate rotor hubs were employed, one with three blade mounting positions at 120° intervals, the other with four blade mounting positions at 90° intervals. Only two of the mounting positions were used for the latter hub. Acrylic blocks offset to the specified angles were mounted on the hub, and the blades were then mounted on the acrylic blocks. The device could be set up with either hub, or with both hubs mounted (both hubs mounted are shown in Figure 4.7).

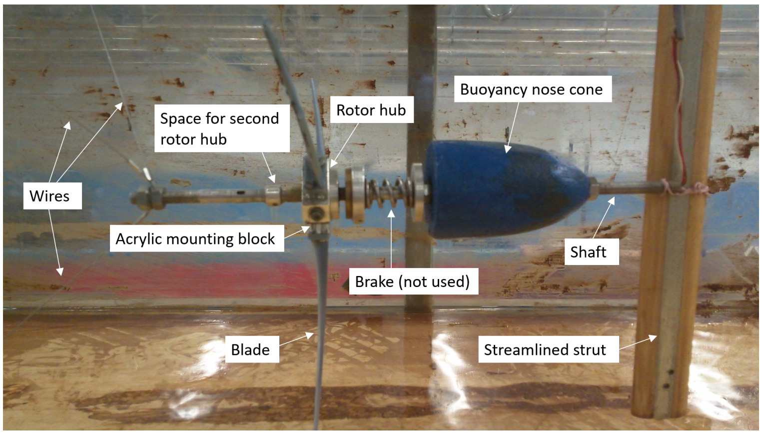

Figure 4.6: The wire hung device in situ with three blades attached

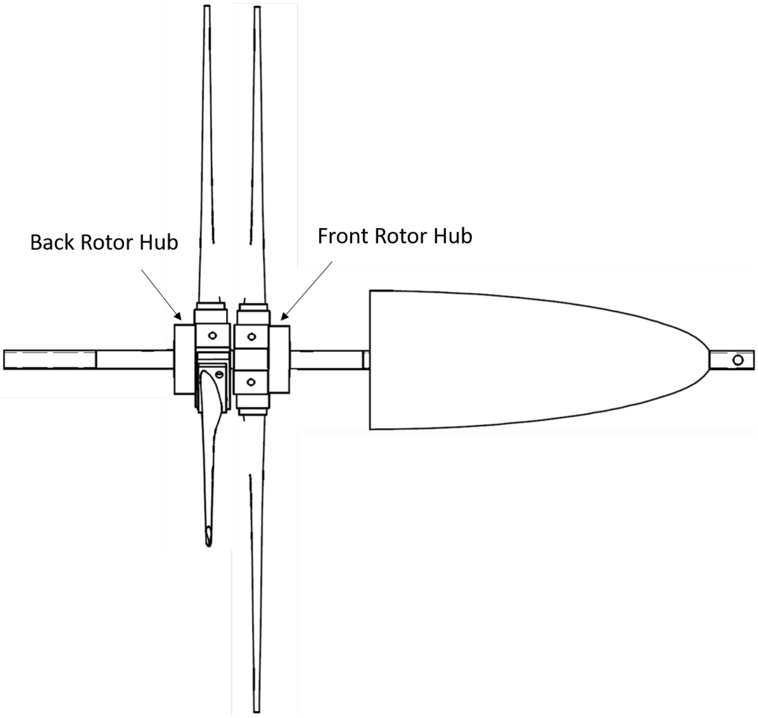

Figure 4.7: The wire hung device in contra rotation configuration, with both hubs attached

To test contra-rotating configurations both rotor hubs were mounted on the shaft at once, separated by approximately 5 cm. Blades with different directionality were attached for each rotor hub so as to achieve contra rotation.

4.2.2 Blade Numbers

For the Wire Hung set of experiments the rotor was varied between a two blade, a three blade and a two-three blade contra-rotating configuration. This variation facilitated the wake comparison of the different configurations running in similar scenarios. Two and three blades were chosen as the simplest choices, and are reasonable possibilities for rotor configurations used in full scale devices (there is some degree of constraint to keep the blade numbers low due to the large cost of blade manufacture). In order to control the rotational speed of the blades and thus change the tip speed ratio (λ), the blade pitch angles were variable. Variable pitch is a well established speed control tool used frequently in wind turbines, and has already been employed in first generation tidal energy devices. Pitch was varied manually by the manufacture of a series of offset blade mounting blocks. Each blade was attached to the device via a small acrylic block which held the blade at an angle between $0-6\,^{\circ}$. Whilst testing a single configuration (including contra-rotating) all blades were mounted at the same angle.

There were twelve configurations tested:

- Two blades at 0, 2, 4 and 6 ° pitch
- Three blades at 0, 2, 4 and 6 ° pitch
- Two-three contra-rotating blades at 0, 2, 4 and 6 ° pitch

4.2.3 Tip Speed Ratio

Unlike the previous set of experiments, the rotational speed of the blades was not directly controlled. Instead, it was indirectly controlled: mechanical resistance to rotation came from the friction of the bearings (a similar setup, where blades are freespinning, is given in Kawahashi (2007)). λ was varied by changing the pitch setting angle of the blades and the number of blades. Again λ acted as a proxy for C_T, and gave an indication of whether it was increasing or decreasing

Table 4.2: λ for different configurations

Configuration	Pitch Angle	λ
2 Blade	0°	5
2 Blade	2°	4.7
2 Blade	4°	2.3
2 Blade	6°	2.3
3 Blade	0°	4.7
3 Blade	2°	2.9
3 Blade	4°	2.3
3 Blade	6°	1.2
Contra 2 Blade	0°	4
Contra 2 Blade	2°	4.2
Contra 2 Blade	4°	1.5
Contra 2 Blade	6°	2.3
Contra 3 Blade	0°	4.1
Contra 3 Blade	2°	3.6
Contra 3 Blade	4°	3.4
Contra 3 Blade	6°	2.5

between configurations. λ was changed by varying the rotational speed of the blades, whilst leaving the fluid flow speed unchanged. The tip speed ratios for each configuration are given in Table 4.2.

4.3 Equipment Used

4.3.1 Flume Tank

Experimental work was based around the University of Strathclyde's re-circulating water flume (seen in Figure 4.8). The flume measured 35 m long, 0.92 m wide and 0.7 m high, with Perspex walls, a steel bottom and an open top. The 35 m length included a 2 m flow settling area immediately downstream of the inlet. The flow was driven by a pump situated beneath the flume and passed through a settler prior to entering the flume channel. The flow speed and depth were set by adjusting the weir height at the outlet of the flume, and by adjusting the pump. These two controls were interdependent: a change in either control resulted in a change in both flow speed and depth. For example, if the weir was raised the cross sectional area of the flow would increase, and the flow velocity drop so as to conserve momentum within the flume. However, as the inlet head would have increased, the conservation of energy within the system would require a further decrease in velocity in the flume. Similarly, any change in the pump's behaviour would result in a non linear change in both the flow speed and the flow height. This made slight adjustments to the flow cumbersome.

As the same flume channel was used throughout the experimental work, wall roughness remained constant throughout. The Perspex sides extended to the base of the channel, and were smooth and free from obstruction, with the exception of six bolts protruding 1-2.5 cm into the flow, at 4.3 m downstream of the nominal turbine position, and a further six bolts at 4.9 m downstream. Panel section joins occurred every 1.83 m, and were smooth on the walls, but caused a slight increase in roughness on the channel floor. The base of the flume was coated, giving it a smooth finish, but at certain points the coating was worn and the steel was exposed to the flow, increasing the roughness over lengths of approximately 5 cm. This likely had some local effect on the flow within the turbulent boundary layer, but a negligible effect anywhere more than a few centimeters from the base. A numerical approximation of the roughness is given in Section 2.2.

4.3.2 Cloudy Water and Flotsam

Due to the age of the flume channel, dust was deposited in the flow from the sump brickwork. Various attempts to clean this gave some success, however the visibility in the flow remained poor. The dust particles acted as seeding for the measurement equipment, ensuring an excellent signal strength at all times. In addition to the dust particles, the detritus of previous experimental work was sporadically found within the flume. Most often this had no effect beyond pricking the authors curiosity, but occasional debris could interact with the turbine device.

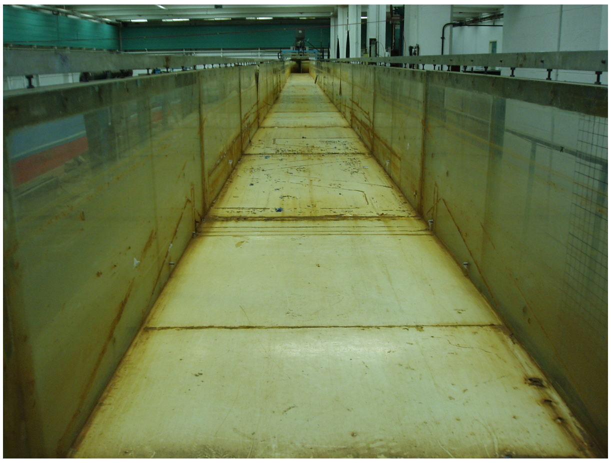

Figure 4.8: Flume without water, showing walls and base

Thus for all experiments the device was regularly cleaned, and for the wire hung experiments a mesh filter was put in place (see Section 4.3.5 for further discussion of the mesh filter).

4.3.3 Asymmetry

As the flow of the flume was altered by the introduction of the mesh filter, two separate descriptions of the flow characteristics are contained in the discussions of the pile mounted experimental results (in Chapter 5) and the wire hung experimental results (in Chapter 6). However, one aspect of the flow consistent for both set-ups shall be mentioned here. Although the flume was geometrically symmetrical, the flow was found to be asymmetrical across the channel, that is, from the near wall to the far wall. At all depths measured and for all distances downstream the axial velocity was greater on the far wall side than on the near wall side. This was caused by the manner in which the flow was introduced into the channel by the pump, and can be considered a feature of the channel. Although this difference was primarily one of V_X changing with distance in the Y direction, V_Y and V_Z were also asymmetrical. A quantitative description is given in Section 5.1.

4.3.4 Tank Vibration

Driving the fluid flow was a 3 phase, 2.5 horse power (1.9 kW) pump, running at a constant speed of 2,900 revolutions per minute (giving a frequency of 48.3 Hz). Ideally the pump frequency would be compared to a Fast Fourier Transform (FFT) of the velocity data from the unimpeded flume so as to ascertain any fluid flow fluctuation due to vibration. However, the Nyquist frequency dictates that the highest frequency of signal that can be detected is equal to half the sampling frequency (Luke, 1999). As the pump frequency far exceeded that of the Nyquist frequency of the measurement instrument (12.5 Hz), any vibrations induced by the pump are undetectable.

4.3.5 Mesh Filter

After the pile mounted experiments had been completed, but prior to the commencement of the wire hung experiments, fibrous contaminants were inadvertently added to the flume system. Due to the wire hung device's sensitivity to contamination within the fluid, which fouled the blades and slowed the rotation of the device, a mesh filter was added upstream of the working section for experiments using this device. This was made up of a coarse wire mesh filter overlaid with a fine netted filter. The wire filter was mounted on a wooden frame, and held rigid using bolts protruding from the channel wall, 5 m downstream of the inlet. The netted filter was made up of 1 mm square holes and held in place by the wire mesh filter, and was periodically removed and cleaned during the course of testing. This greatly improved the quality of the fluid flow in the working section. However, due to the pressure differential created by the mesh, a head difference was established across the mesh.

Upstream, on the inlet side, the head was increased, whilst it remained constant downstream. Despite the increase in model blade diameter, the depth of fluid in the working section could not be increased without the fluid overtopping

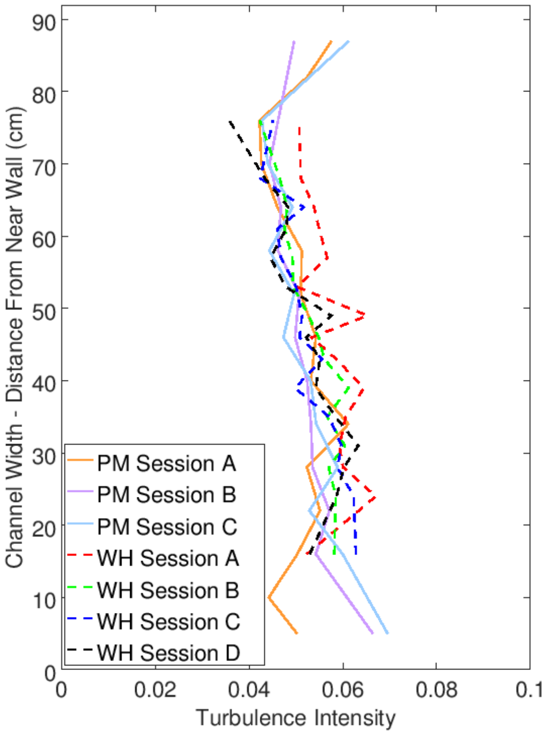

Figure 4.9: Comparison between unimpeded flume turbulence intensity before and after the addition of a mesh filter

the channel walls upstream of the mesh. Therefore the flow height and flow speed were maintained at 40 cm and approximately 40 cm/s. The addition of the mesh also changed the flume characteristics by adding small scale turbulence to the flow.

In Figure 4.9 a comparison is made between the turbulence in the unimpeded flume before and after the addition of a mesh filter. Results compared here are those shown individually in Figures 4.26 and 6.4, without and with the mesh respectively. It appears that the turbulence intensity increases very slightly with the addition of the mesh filter, but the increase is small, less than the fluctuation between measurement points. It is possible that these small scale eddies could facilitate mixing more efficiently than the larger scale turbulence and eddies of the pile mounted experiment. However, the initial Pile Mounted experiments were not rerun, and so further testing would be required to confirm this.

4.3.6 Working Section - Pile Mounted Device

The flume used was open topped and so accessible at any distance downstream. The maximum range used within the 35 m flume was 6.25 m (for the Pile Mounted experiments), equivalent to 25 D. As both the inlet and the outlet would affect the flow far upstream and downstream respectively, the working section was chosen to be in the mid section of the flume. It was determined by positioning the device 16 m downstream of the inlet (and consequentially 19 m upstream of the flume outlet). Thus the working section was from 16 – 22.25 m downstream of the inlet. All measurements for the pile mounted experiments (found in Chapter 5) were taken within this section. Any further references to the nominal turbine position in Chapter 5 refers to this. Further characteristics of the flume are discussed in Section 5.1.

4.3.7 Working Section - Wire Hung Device

The mesh generated significant turbulence in its immediate vicinity. Therefore, the position of the working section had to be reassessed in order to ascertain at what point the turbulence intensity level became steady in the X direction. With this in mind a series of measurements were taken in the unimpeded centre of the channel, from 12 m downstream of the inlet to 30.5 m downstream of the inlet, and the results can be seen in Figure 4.10 and Figure 4.11.

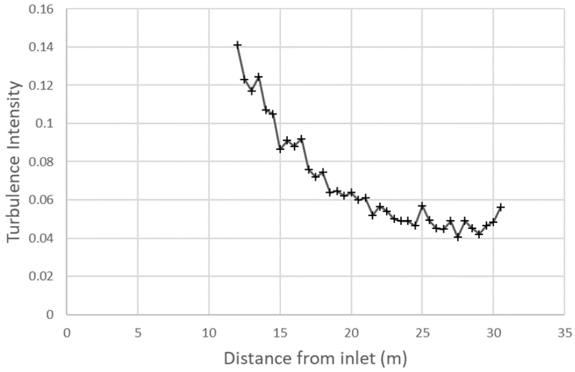

Figure 4.10: Turbulence intensity downstream of the mesh

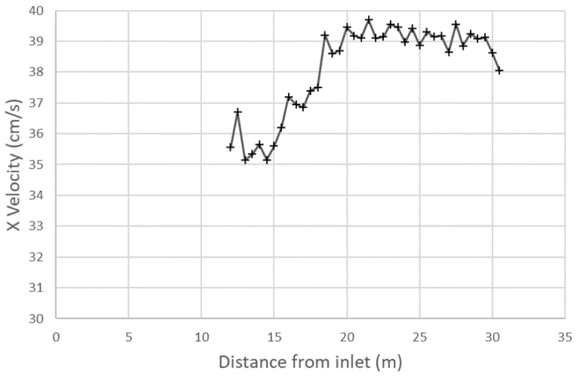

Figure 4.11: V_X downstream of the mesh

Figure 4.10 shows the turbulence clearly decreasing travelling downstream, from a maximum of 14% to a minimum of 4%. There is a slight suggestion that the turbulence may be rising at the end of the measurement point (presumably due to the approaching outlet), but this is inconclusive. An alternative reading of the graph may be that the turbulence has become steady by 21.5m downstream, and the variations downstream of this are natural variations due to the flume tank rather than the filter. Whichever reading is correct, it seems likely that the turbulence will not drop any further beyond the minimum already reached. Close to the filter there is a high level of ambient turbulence, which gradually decreases with distance downstream. It is unclear whether this decrease is reversed or merely halted further downstream. If a 2 % variation in ambient turbulence is deemed acceptable, there is a significant portion of the flume which is usable (21.5 – 30.5 m downstream of the inlet). This is the area in which further data capture took place.

One important point to notice about Figure 4.11 is that the variation in V_X is small when compared with the variation in turbulence intensity. However, within the smaller variation it seems that the velocity rises with distance downstream, immediately after the mesh. As with the turbulence intensity, it is unclear whether the V_X begins to drop towards the end of the test area, or is remaining approximately stable.

4.4 Instrumentation

4.4.1 Methods of Measuring Velocity

There are a variety of possible tools used for measuring velocity within a flume, such as hot wire anemometers, laser doppler velocimetry (LDV), particle imaging velocimetry (PIV), electromagnetic current meters and acoustic doppler velocimetry (ADV). Of these, only ADV devices offer three dimensional measurements, high sample rates, a small sample volume and easy deployment, whilst avoiding zero-drift (Voulgaris and Trowbridge, 1999). A further advantage is that unlike light signals, acoustic signals are not limited by murky or excessively turbid water, as might be found in certain field testing locations or even certain flumes. Unlike LDV, ADV is an intrusive measurement technique in that it has a physical presence which disrupts the flow, but the intrusion is so small that it can safely be considered negligible in most flows (Cea, Puertas and Pena, 2007).

4.4.2 Acoustic Doppler Velocimetry

The Acoustic Doppler Velocimeter (ADV) was designed in the early 1990s after demands for a measurement device that would provide sub-centimetre resolution at 25 Hz for less than $10,000 (Lohrmann, Cabrera and Kraus, 1994). Although the exact settings can vary depending on the device model, the following description covers the general aspects of all ADV devices, whilst specifically describing the model used within this research. The ADV is comprised three modules: the measurement probe, the signal conditioning module and the signal processing module. The probe head is submerged in the water, with three receiving ‘ears’ positioned so as to face a sample region 5 cm from the probe head. The majority of the instrumentation is kept out of the flow in a waterproof cylinder, using a long rigid stem so as to minimise flow disruption. The conditioning module is attached by cable to the signal processing block, which in turn outputs to a computer.

The system works by sending a sound signal from the probe head to the sample volume, where a small portion of the signal is reflected back to the receivers by the particles in the flow. The Doppler shift observed in the returning signals can be interpreted as being due to the velocity of the particles in the direction of the returning signal, thus with three probe ears the three dimensional velocity of the flow can be established. This quantity is an average of the velocity within the sample area. As well as returning a velocity measurement, each probe ear returns a value for the signal strength, the correlation (COR) and the signal to noise ratio (SNR) (Chanson, 2008). The SNR is a measure of the quality of the sound signal received by the probe, and the COR indicates how consistent the velocity is during the sample period of each measurement, higher being more consistent (Cea, Puertas and Pena, 2007). It should be noted however, that measurements with low turbulence will have a higher COR than measurements with high turbulence.

A Nortek ADV was used as the primary mechanism for data capture. The ADV was mounted in the following way to allow three dimensional movement of the probe between measurements. Rails were attached to the tops of the flume walls, and a trolley was run along them (for X direction translation). The ADV was held in position on this trolley using a clamp (for Y direction translation) and a collar (for Z direction translation). The device was manually mounted, and aligned with the flume direction. The mounting arrangement is shown in Figures 4.12 and 4.13. For the ADV to be able to operate, the probe head had to be completely submerged. Furthermore, a blanking distance immediately beneath the probe head was required and measurements could not be taken within it. Therefore, no measurements could be taken within 10 cm of the flow surface. The impact of this on measurement positioning can be seen in Figure 4.14.

To mitigate this, the turbine device could have been made smaller, which

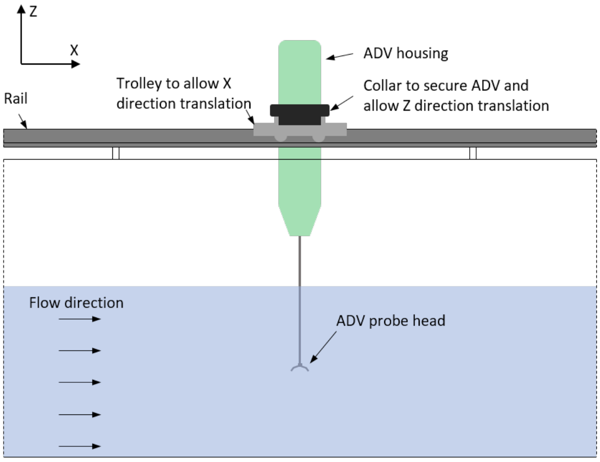

Figure 4.12: Elevation view of a section of the measurement arrangement

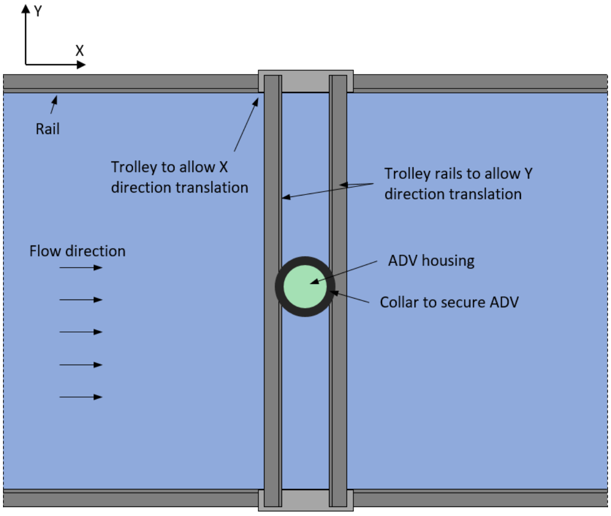

Figure 4.13: Plan view of a section of the measurement arrangement

would have allowed measurements to be taken at and above the top of the rotor swept area. The rotational speed of a smaller device would need to be proportionally higher in order to maintain similarity in tip speed ratio. Achieving consistency with higher rotational speeds provides some increase in difficulty in the control and measurement of the blade rotation, and can in some cases result in cavitation. Making the experiment smaller would also increase the uncertainty within results, as the equipment would be subject to larger relative errors and limitations. The impact of the unrecorded section on the results is mentioned in Section 5.3.4.

The data was recorded using NDV Data Acquisition and Nortek CollectV software, and was exported to WinADV (Version 2.027) for processing. Data was processed using the commercially available software Matlab.

4.4.3 Sources of Error

An unwanted side effect of using Doppler measurement is Doppler noise, which causes a problem by making the turbulent kinetic energy appear greater than it actually is (Cea, Puertas and Pena, 2007). This noise can be approximated as Gaussian white noise, and experimental testing reveals that it is significantly greater in the horizontal plane than in the vertical direction. Therefore the horizontal component spectra may deviate from the $-\frac{5}{3}$ power law (Equation 2.2), whilst the vertical component remains a good fit (Nikora and Goring, 1998).

Another type of error in ADV measurements is caused by aliasing, which takes effect if the set velocity limits are exceeded (Cea, Puertas and Pena, 2007). This can be avoided by ensuring that the velocity range specified to the device is appropriate and is unlikely to be exceeded.

Salinity and temperature are input in order to calculate the adjusted speed of sound. If the temperature is known to within 1 degree the error is limited to 0.2 % (Lohrmann, Cabrera and Kraus, 1994).

4.4.4 Filtering

Erroneous measurements caused by Doppler error or by aliasing will appear as uncorrelated spikes, and so are removable by a filter. Filtering data is a common technique used far beyond the extent of ADV measurement. It does not attempt to reconstruct a dataset, but to provide an ‘equivalent’ dataset with respect to certain parameters (mean kinetic energy, turbulent kinetic energy, power spectra etc.) (Cea, Puertas and Pena, 2007). Basic filtering occurs when data points which fail to meet acceptable levels of SNR and COR are removed. A minimum

SNR of 15 dB is given by Lohrmann, Cabrera and Kraus (1994) as the lower threshold for measurements at 25 Hz, though Cea, Puertas and Pena (2007) suggests that this limit is flexible, and hard to determine absolutely. Chanson (2008) offers a minimum value of 60 % for COR, though Bahaj *et al.* (2007) gives a higher threshold of 70 %. Both the SNR and the COR can be improved by adding dye or seeded particles into the flow to improve the acoustic backscatter.

Once the samples which fail to meet the specified criteria are removed, a second, 'de-spiking' stage of filtering is applied. A threshold is set with respect to the mean velocity and standard deviation, and any point outside of this is either removed or replaced. This process is iterative, as the properties of the data set change after each removal; de-spiking is continued until all data points fit inside the threshold (Cea, Puertas and Pena, 2007).

In Giles *et al.* (2011) it is suggested that filtering does not have a large impact on mean flow velocities, as flow spikes are equally negative and positive. Filtering is of more significance for turbulence, where the root mean square of fluctuations is calculated. In these experiments filtering was applied by the processing software by removing data which fell below a specified value of signal to noise ratio or correlation. Phase space threshold de-spiking was also applied to remove erroneous data points.

4.4.5 Sampling Frequency and Size

In order to get an accurate reading at each measurement point the sampling frequency and sample size were considered. Because all points in the flow were turbulent, any measurement would have to sample at a frequency high enough to ensure that the mean result was not unduly influenced by individual fluctuations. In Chanson (2008) a very large sample size is recommended to ensure accuracy over the four statistical moments (above 5,000 for the first two moments, and above 60,000 – 90,000 for the second two). However the collection of large amounts of data increases the length and complexity of any experiment.

The mean kinetic energy in the turbulence is discussed in Section 2.1 and Equation 2.5 gives a method of calculating the turbulent length scale.

For the unimpeded flume the turbulent time scale was calculated as 0.0983 s. With a measurement frequency of 25 Hz, the time between samples was 0.04 s, less than half that of the turbulence time scale. This suggested that whilst some small scale turbulence would escape detection, larger turbulence would be captured. As stated in Lohrmann, Cabrera and Kraus (1994), a 25 Hz resolution ‘is sufficient to capture a significant fraction of the turbulent kinetic energy.’ The sample size is further discussed in Section 4.7.1.

4.5 Data Capture Process

4.5.1 Grid Positions - Pile Mounted Device

Data was gathered for individual points within the flume, which would be built up into a series of grids, which then formed a three dimensional flow. Measurement positions were spaced so as to capture the relevant aspects of the wake as it developed. For the pile mounted experiments (standard configuration), 15x6 grid points were taken at 10 distances downstream, giving 900 measurement points. Figure 4.14 shows the measurement grid for the standard case ($\lambda = 4$), taken at a variety of distances downstream. All width (Y direction) distances referred to indicate the distance from the near wall. As mentioned above, the ADV was unable to take measurements within the 10 cm closest to the surface due to the requirement for the probe to be submerged and the blanking distance. Thus the top section of the rotor path was not recorded. Figure 4.15 shows the distances downstream at which the measurement grid was taken.

For the further configurations the positions of measurement points were biased towards the centreline of the rotor, as this was the relevant area of interest for

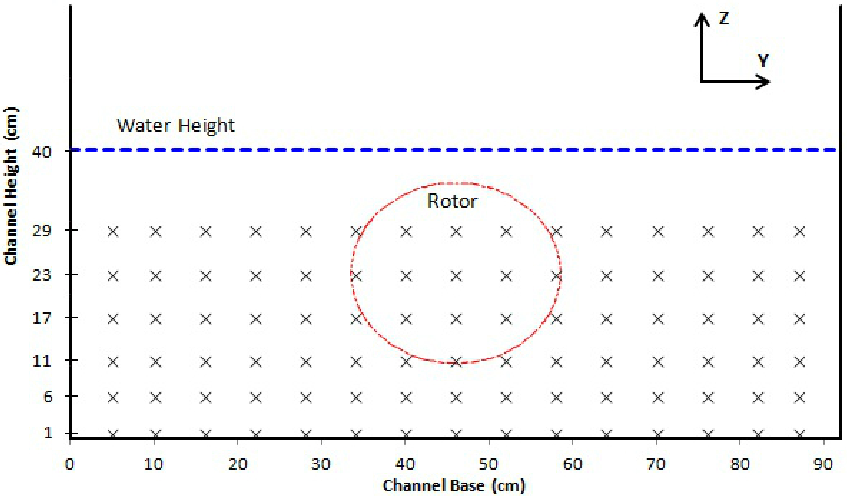

Figure 4.14: Measurement Positions Grid for the Standard Case ($\lambda = 4$)

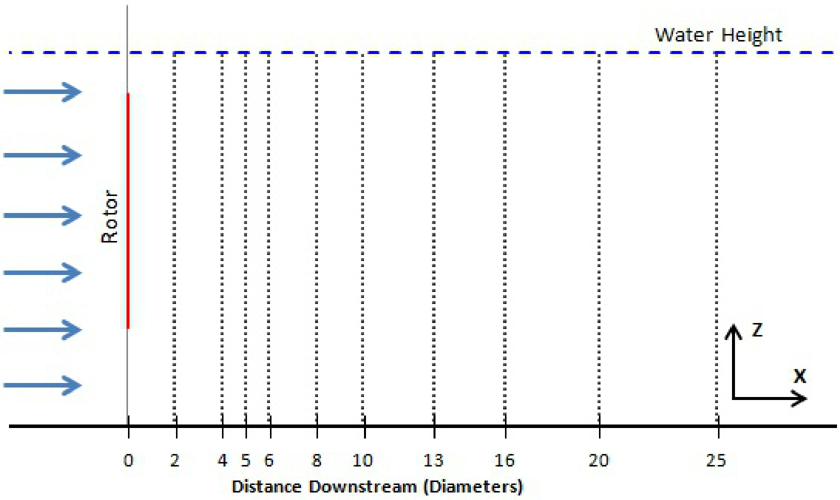

Figure 4.15: Measurement Positions Downstream for the Standard Case ($\lambda = 4$)

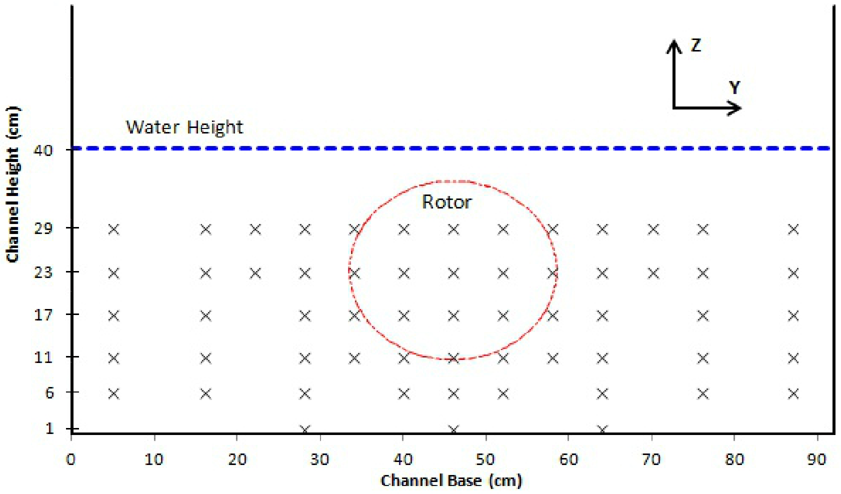

Figure 4.16: Measurement Positions Grid for the Non Standard Cases ($\lambda = 3, 5$ and 0)

assessing the turbine wake. Furthermore, fewer measurement grids were taken downstream. Whilst this reduction decreased the total number of data points, it did not significantly decrease the number of data points from the key areas of comparison (i.e. at hub height). The cross sectional measurement grid is shown in Figure 4.16, and the downstream measurement points are shown in Figures 4.17, 4.18 and 4.19.

At each measurement position two readings were taken: one with the turbine in place (device wake measurement), then one with the turbine removed but with the flow regime held the same ('unimpeded' flume measurement). Thus for the standard configuration of $\lambda = 4$, 900 measurements were taken behind the turbine, and a further 900 measurments were taken in the flume with the device absent. This data was used to characterise the flume without the device in it, and to normalise the turbine wake data against. Only one set of 'unimpeded flume' measurements was taken between the $\lambda = 3$ and $\lambda = 5$ configurations, and they were both normalised against the same measurement points.

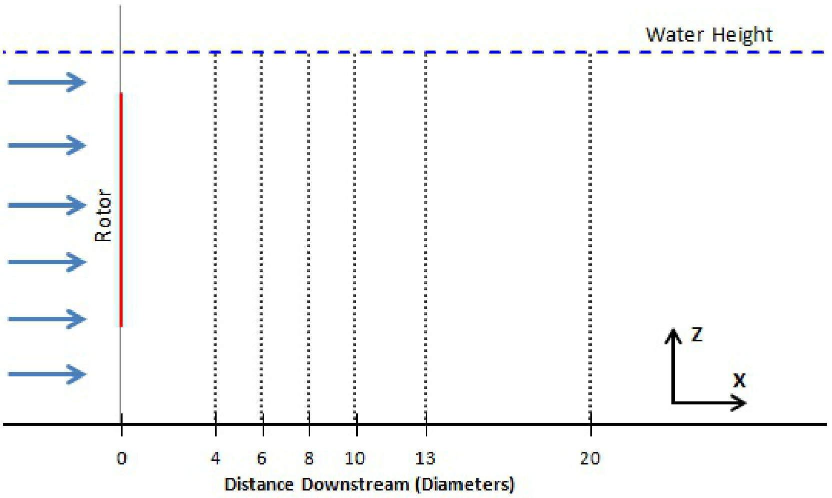

Figure 4.17: Measurement Positions Downstream for the Case $\lambda = 3$

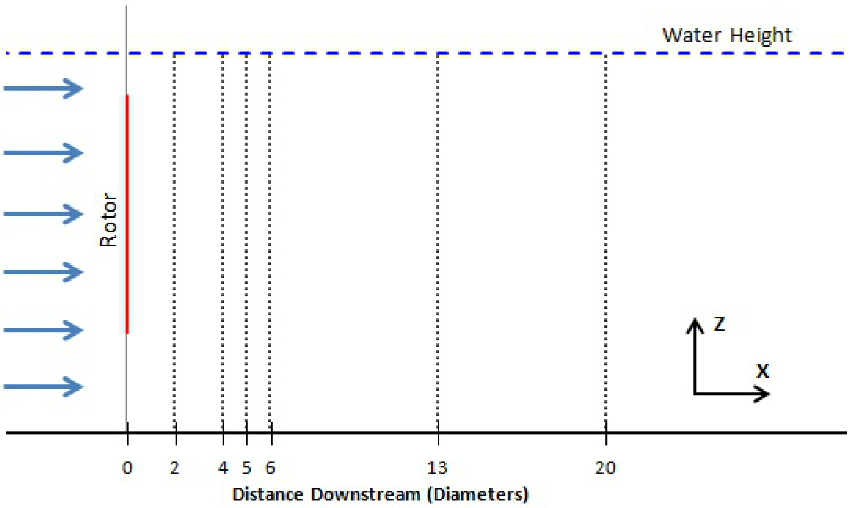

Figure 4.18: Measurement Positions Downstream for the Case $\lambda = 5$

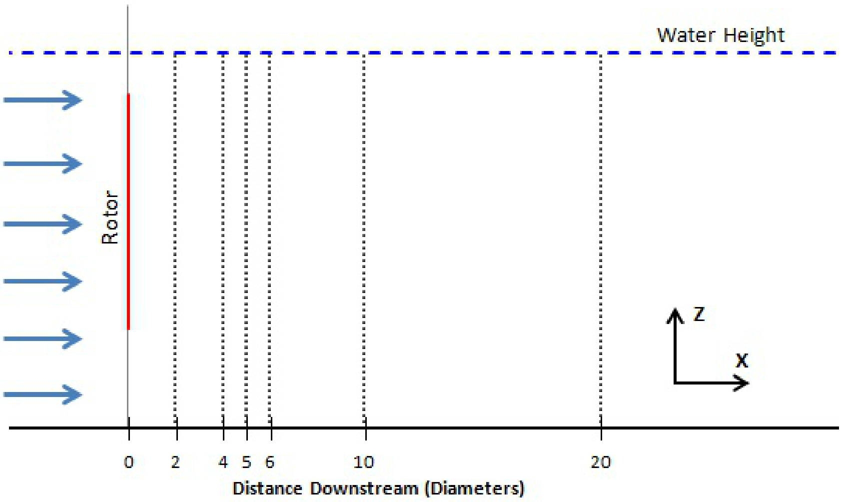

Figure 4.19: Measurement Positions Downstream for the Case $\lambda = 0$ (Structure Only)

4.5.2 Grid Positions - Wire Hung Device

As with the Pile Mounted experimental setup, a measurement grid was applied for the Wire Hung setup and repeated at different distances downstream. However, unlike previously, the grid did not vary in height. Instead it was a single horizontal line of points neglecting the lower and upper parts of the channel in favour of the hub height. This allowed profiles to be taken at multiple distances downstream within a single measurement session, reducing the effect of any flume inconsistency. For each configuration the points measured at hub height were as shown in Figures 4.20 and 4.21, the former showing the cross sectional grid, the latter showing the downstream distances at which that grid was applied.

Thus for each blade configuration 105 measurements were taken (not including unimpeded flume measurements), and there were 12 unique configurations. As with the previous experimental setup, in each test session measurements were also taken for the unimpeded flume to provide data for normalisation.

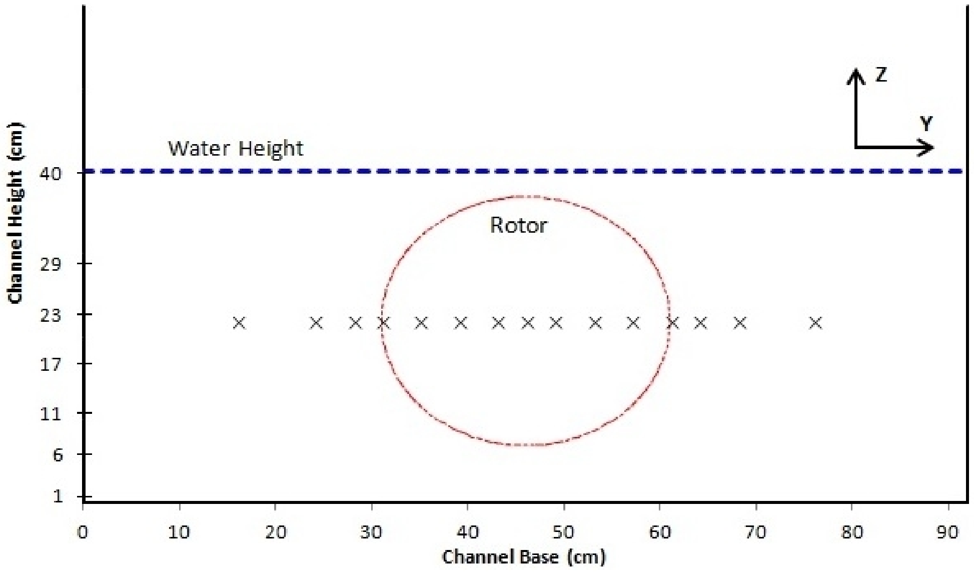

Figure 4.20: Cross sectional measurement grid for wire hung device (all measurements at hub height)

4.6 Typical Test Runs

4.6.1 Pile Mounted Device

The steps involved in a typical test run are numerated below for the pile mounted device.

1. Set flume velocity and level using sluice gate and pump speed. Flow height was measured against markings on the flume channel wall, and flow speed was measured using the ADV probe.

2. Position the turbine device (as described in Section 4.1.1) in the flume; the position was marked on the flume floor to ensure consistent location across measurement sessions.

3. Set the rotational speed of the turbine blades by varying the power supplied to the turbine motor.

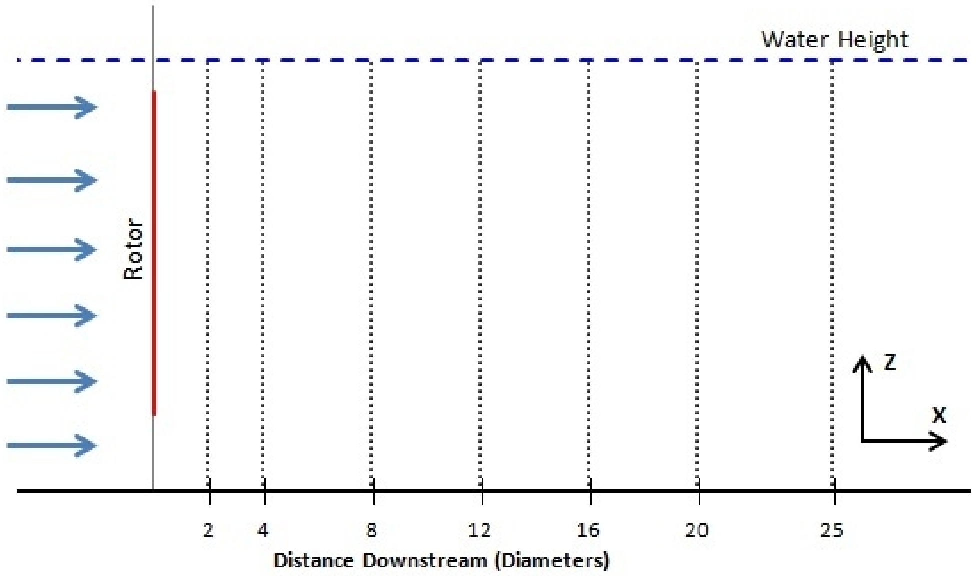

Figure 4.21: Meaurement positions downstream for wire hung device

4. Measure the rotational speed of blades, by counting blade rotations over a 15 second period. For faster blade rotational speeds this was done by taking video footage of the turbine, and reviewing it in slow motion. Rotational speed was always measured a minimum of three times.

5. Position the probe in the location of the first measurement point. The lateral, downstream and rotational locations of the probe were marked on the flume and device, and the measurement software gave distance to channel base.

6. Record velocity measurements at 25Hz over 33s at the measurement point.

7. Repeat steps 5 and 6 for each subsequent measurement point in the measurement grid (e.g. for all points in Figure 4.14).

8. Remove the turbine device and repeat measurements in identical positions to the previous measurement run.

9. Drain flume.

The order of measurements was varied, with either the device wake being measured first, then the same locations with the device removed measured second (as described above), or the flume without device measured first, then the device wake. This ensured that any decay in velocity of the flume throughout the course of a measurement session would not result in a systematic error throughout all results. (It should be noted that no decay in velocity of the flume during measurement sessions was noted throughout testing). For pile mounted experiments a single measurement grid (such as shown in Figure 4.14 or Figure 4.16) was taken within a measurement session; thus a single configuration required multiple measurement sessions.

4.6.2 Wire Hung Device

The steps involved in a typical test run are numerated below for the wire hung device.

1. Set blade pitch angle for device by mounting blades on defined acrylic blocks.

2. Set the flume velocity and level using sluice gate and pump speed. Check the flow speed in flume centre using the probe.

3. Position the turbine device (as described in Section 4.2.1) in flume; the position was marked on the flume to ensure consistent location across measurement sessions).

4. Measure the rotational speed of blades by counting blade rotations over a 15 second period. For faster blade rotational speeds this was done by taking video footage of the turbine, and reviewing it in slow motion. Rotational speed was always measured a minimum of three times.

5. Position the probe in the location of the first measurement point. The lateral, downstream and rotational locations of the probe were marked on the flume and device, and the measurement software gave distance to channel base.
6. Record velocity measurements at 25 Hz over 33 s at the measurement point.
7. Repeat steps 5 and 6 for each subsequent measurement point in the measurement grid (e.g. for all points in Figure 4.20).
8. Remove the turbine device and repeat measurements in identical positions to the previous measurement run.
9. Drain flume.

For wire hung experiments all measurements required for any one configuration were taken within a single measurement session.

4.7 Errors and Uncertainties

Any experimental work will be subject to errors and uncertainties. Three basic types have been identified and are discussed in turn below.

4.7.1 Velocity Fluctuations Due to Turbulence

A brief description of turbulence has been given in Section 2.1, where it is said that turbulence can be thought of as random velocity fluctuations about a mean. The true mean is the actual mean of the flow velocity, as would be found with an infinite sample size. The measured mean is that which is found with a finite sample size. If the sample size is small, the measured mean may deviate from the true mean due to the influence of the turbulent fluctuations in the flow. As the sample size increases the measured mean will tend towards the true mean.

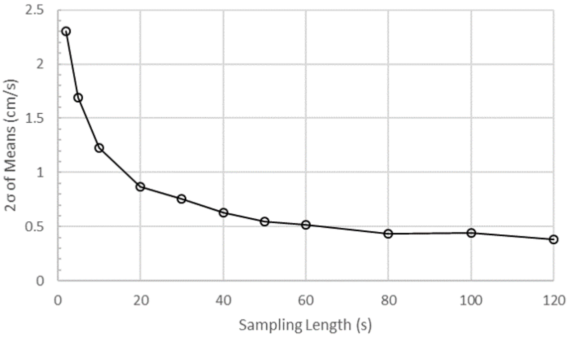

Figure 4.22: Standard deviation of means for different sampling lengths

A large data series was taken over 30 minutes at a frequency of 25 Hz, and the sample mean was assumed to be representative of the true mean. The data set was then broken into a series of 10 second samples, and the V_X mean calculated for each one (giving 185 different measured means). The standard deviation, σ, over these means was then calculated. This was repeated for sample sizes between 2 seconds and 120 seconds long, and the results are plotted in Figure 4.22. An uncertainty value of $\pm 2\sigma$ was chosen as the value which would encompas 95 % of all values (Schenck, 1968).

The uncertainty decreases as the sampling length increases, in an inverse power relationship. To half the uncertainty the sample size must be increased by a factor of four. A small sample size would be preferable so as to take less time for the collection of multiple data points. However, the sample size dictates the uncertainty, with a smaller sample size resulting in increased uncertainty.

A sample size duration of 33 s was chosen as one which would allow for approximately 200 measurements per day (including set up and instrumentation). This sample size resulted in an uncertainty of $\pm 0.7 cm/s$, i.e. 95 % of all measurements would be within $\pm 0.7 cm/s$ of the measured mean, or $\pm 2\%$ of the velocity in the centre of the flume.

When calculating velocity deficit there is an error in both the wake and freestream measurements. These errors can be combined through quadrature: the square of the error is equal to the sum of the squares of the errors of the

Table 4.3: Expected error in the centre of the flume from a sample size of 33s at 25Hz

Variable	2σ
V_X	0.7 cm/s
V_Y	0.46 cm/s
V_Z	0.37 cm/s
I	1.1 %

constituent parts (Schenck, 1968), as stated in Equation 4.1.

$$\mu^2 = \mu_{wake}^2 + \mu_\infty^2 \tag{4.1}$$

This gives the error as a percentage of $\frac{V_X}{V_\infty}$. Errors in deficit due to turbulence are therefore calculated individually for each point.

From a 33 s sample size the errors for I, V_Y and V_Z are also calculated, using the same method, and are presented in Table 4.3.

Sampling errors are proportionally larger for V_Y and V_Z than they are for V_X.

4.7.2 Instrumentation and Experimental Setup

There are various possible sources of error from instrumentation and experimental setup which are discussed below.

4.7.2.1 ADV Signal Error

Signal error in the ADV measurements can be caused by Doppler noise or aliasing, as described in Sections 4.4.3 and 4.4.4. However, the signal to noise ratio (SNR) and correlation (COR) values were excellent throughout. Over 10,000 data points selected at random the SNR exceeded 25 dB at every single measurement (a lower threshold of 15 dB is recommended in Lohrmann, Cabrera and Kraus (1994)). For the same data points the COR exceeded 95 in 99.8 % of data points (lower thresholds of 60 and 70 are used in Chanson (2008) and Bahaj, Batten and McCann (2007) respectively). Signal errors are therefore dismissed as negligible.

4.7.2.2 Temperature

During testing the outside temperature ranged from around -10 to 20 degrees Celsius. Laboratory temperatures were not taken, however the variance would be considerably less than this. Water temperature variation would be lower still, as water was held in a sump below ground. A conservative estimate of the water temperature range of $\pm 5°C$ results in a measurement error of $\pm 1\%$ (as discussed in Section 4.4.3). However, temperature of the water was not expected to vary meaningfully within a measurement session, and therefore this error is only applicable between measurement sessions, and forms part of the error discussed in Section 4.7.3.

4.7.2.3 Rotational Misalignment

To ascertain the accuracy of the probe alignment, the ADV was rotated by 110° and measurements were taken at 10° intervals in the centre of the channel. It was visually apparent that the large part of the flow travelled in the X direction, parallel with the flume walls, and any component travelling otherwise was small. Thus as the ADV was rotated, the velocity recorded by the ADV, V_X, decreased, whilst V_Y increased, in a sinusoidal form. When mapped graphically against a sine wave, the V_X and V_Y gave an offset value of 2.26° against what would be expected if there were no V_Y component. This could mean either that the probe was misaligned by 2°, or that there was a small component of velocity present in the Y direction. It was visually confirmed that the flow in the flume contained a V_Y component in the central column of the flume. However, were there to be a 2° offset, this would result in 99.9 % of V_X being measured as V_X (since $sin(90 - 2) = 0.999$). As this error is orders of magnitude lower than others discussed, it is not considered further.

4.7.2.4 Blade imperfections

Turbine blades for the Wire Hung experiments (Chapter 6) were manufactured using a high resolution 3D printer, from Veroblue, an acrylic polyjet resin, and differences in blades at manufacture are negligable. On occasion, blades were prone to sudden fracture at the root. This was due to incorrect installation procedure, and never occurred during operation. Blades could also be susceptible to bending at the tip after prolonged useage. To mitigate this each blade was visually checked prior to each experimental run, and any blade displaying bending under no load was discarded. Bending which was not apparent on visual inspection was not mitigated, and may contribute to error. In addition, any permanent bending of the blades which may have occurred within a single test run was also not accounted for. This could have affected the performance of the blades, and thus the rotational speed of the turbine during operation. This error is not quantified, and is noted qualitatively only.

4.7.3 Flume Consistency

Measurements were taken over the course of many days, at different times. Although every effort was made to set the equipment up in the same way each time, certain uncontrollable variables meant that there was the potential for variation in measurements between days. The sump was found to have a leak in it which would, over time, result in an increased head being required to move water to the flume. It was not possible to refill the sump prior to every experiment, but as the leak was small it was decided to continue with tests and refill the sump irregularly. The pump was old, and may have been subject to some variation in its output. Water temperature fluctuations may also have impacted the performance of the pump.

Although this uncertainty is a subset of that discussed in Section 4.7.2, due to its significance and the different approach taken to provide a resolution it has

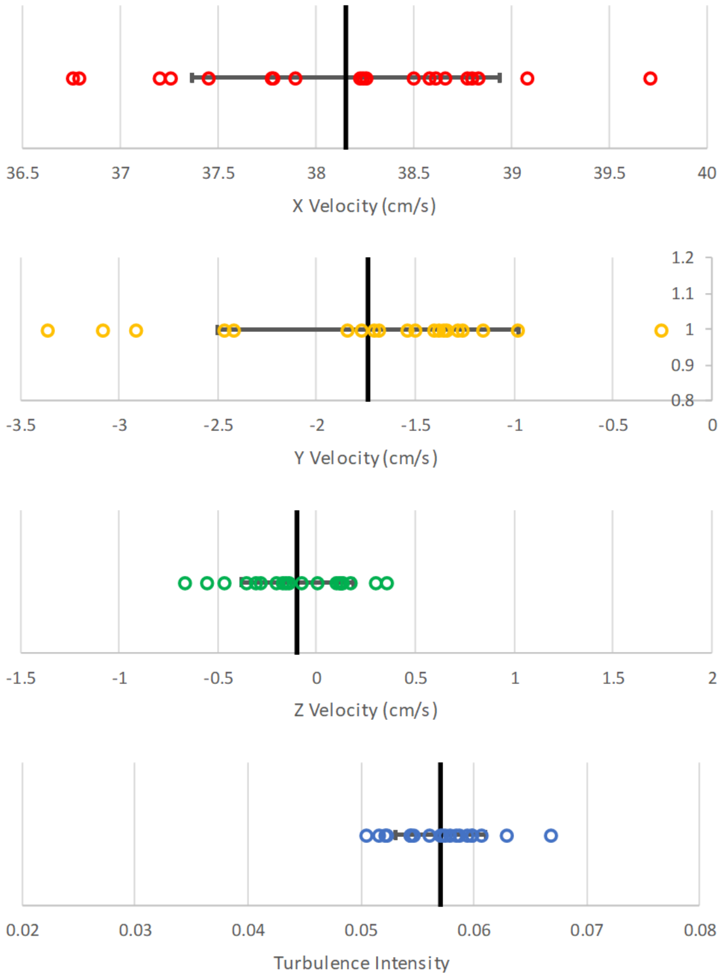

Figure 4.23: V_X, V_Y, V_Z and I measurements in an identical location over 20 measurement sessions

been analysed seperately here.

4.7.3.1 Measurement Session Comparison

To ascertain the magnitude of the difference, configuration measurements were taken in the flume during 20 measurement sessions. These measurements were taken at the same location in the flume (2 D upstream of the nominal turbine position at hub height), under test conditions, with no device in the flume. Figure 4.23 shows the spread of the velocity and turbulence measurements over the 20 measurement sessions.

Average V_X direction velocity measurements are shown in red, and the plot is

Table 4.4: Statistical variation of measurements due to flume inconsistency

Quantity	Mean	Absolute Range	2σ
V_X	38.16 cm/s	2.95 cm/s	1.52 cm/s
V_Y	-1.74 cm/s	3.1 cm/s	1.48 cm/s
V_Z	-0.10 cm/s	1.02 cm/s	0.54 cm/s
I	0.057	0.016	0.008

dissected by the mean of all measurements (vertical black line). A one σ variance is also shown (horizontal error bar). Results for V_Y, V_Z, and I are also shown in yellow, green and blue respectively. $\pm\sigma$ encompasses 68 % of all measurements within a normal distribution, and $\pm 2\sigma$ encompasses 95 % of all measurements (Schenck, 1968).

Results are tabulated in Table 4.4 where it can be seen that there is considerable variation within the flume V_X over different measurement sessions. A range of almost 3 cm/s is required to cover all the measurements taken, and it is likely that 95 % of all measurements will be within ±1.52 cm/s (i.e. within 2σ). The range of results in V_Y is similar, with a similar 2σ, whilst differences in V_Z are smaller. Differences in turbulence intensity range from 0.050 to 0.067. This is again a range which highlights the inconsistent performance of the flume.

In Figure 4.24 the V_X results are shown in the chronological order in which they were taken. Results do not show a trend based on the order in which they were taken, strongly implying that the cause of the inconsistent behaviour of the flume is not a predictable trend over time.

A further comparison looks at example velocity profiles in the unimpeded flume at 2 D and 20 D downstream of the nominal turbine position. Figure 4.25 presents the velocity profiles at hub height, 2 D downstream from the nominal turbine position, taken on three non-consecutive days. These measurements were taken in the unimpeded flume, and ideally values should be identical, but are not. Instead, a difference exists between each of them, but most strikingly between Series A and the others. Series B and C are distinguishable, but all the points in

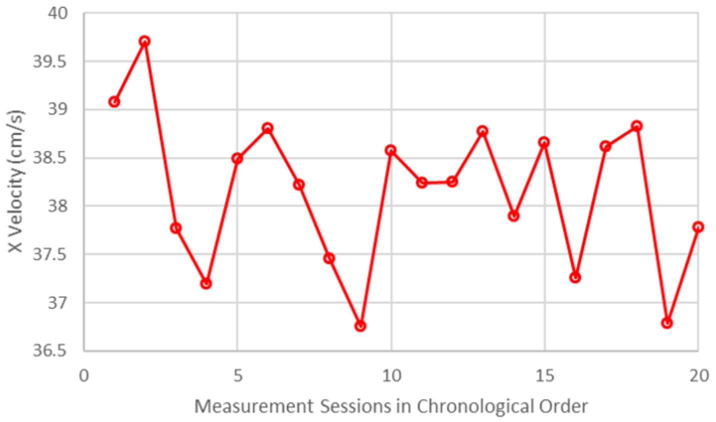

Figure 4.24: V_X plotted in order of measurement session

Series B are within one standard deviation of the corresponding points in Series C. This is not the case for Series A, where only 9 of the 13 points are within one standard deviation of the corresponding points in Series C.

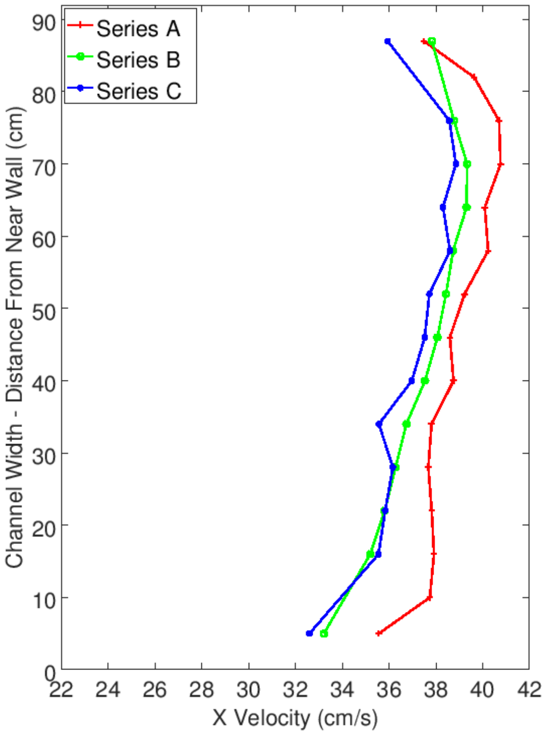

Figure 4.25: V_X over three measurement sessions at 2 D downstream

Figure 4.26 shows a further three hub height V_X profiles taken on different days, this time at 20 D downstream. Once again the profiles are not identical, with the Series A velocities exceeding the other two, which are more closely matched. In this example all the points on the Series B profile are within one standard deviation of Series C, but only 9 of the points from Series A are within one standard deviation of the points in Series C.

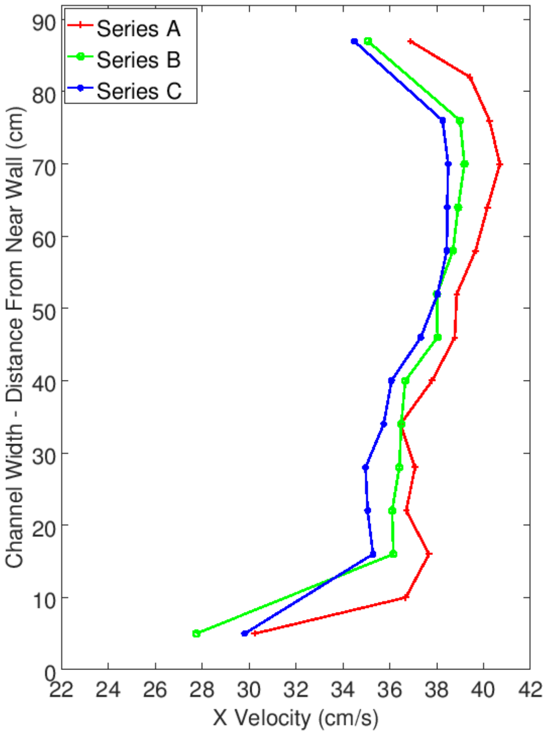

Figure 4.26: V_X over three measurement sessions at 20 D downstream

After the mesh (discussed in Section 4.3.5) was added, further comparison was done between measurement sessions. Similarity in profile shape can be seen from the plots shown (Figures 4.27a to 4.27d), though it can be seen that a small variation in magnitude exists. Taking the average velocity across the flume at 2 D downstream of the proposed turbine position, the first two examples are slightly slower than the third, which is slightly slower than the fourth. Quantitatively this has been expressed in Table 4.5.

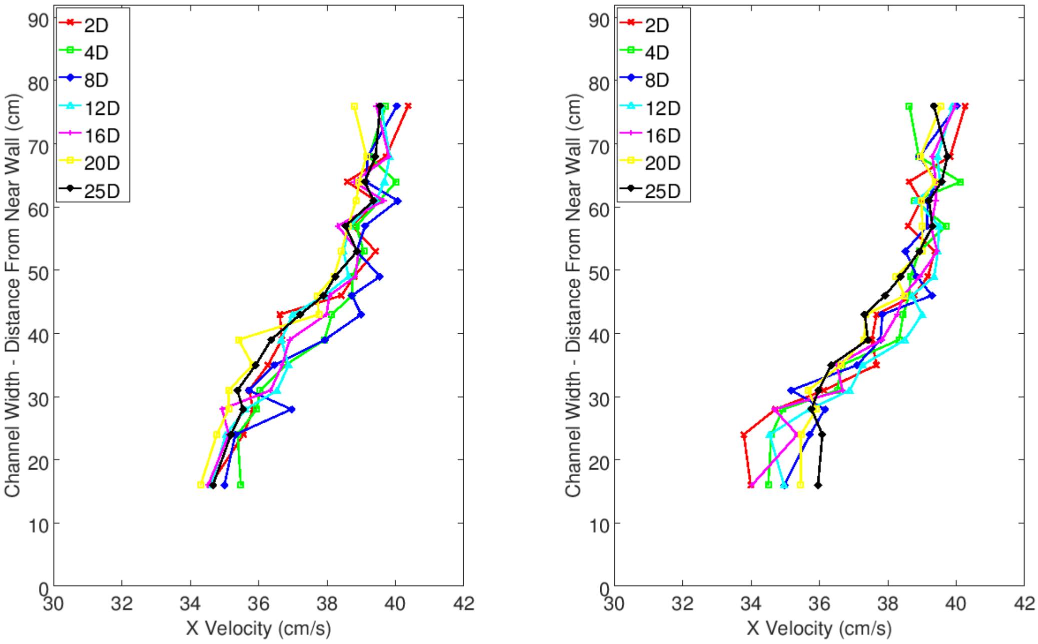

(a) V_X from Measurement Session A (b) V_X from Measurement Session B

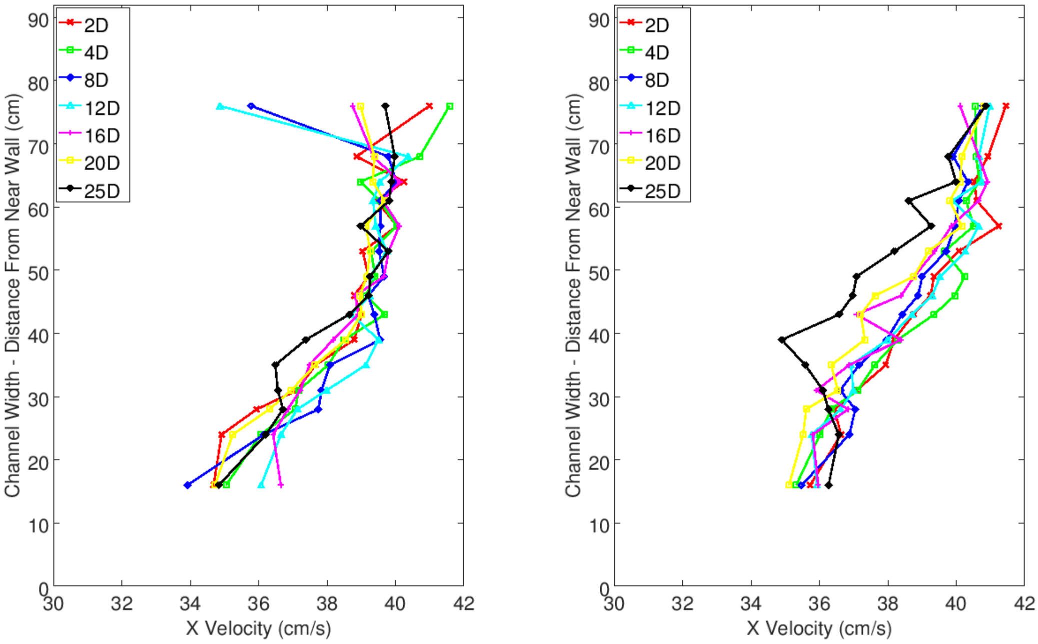

(c) V_X from Measurement Session C (d) V_X from Measurement Session D

Figure 4.27: Unimpeded flume V_X over different measurement sessions

Table 4.5: Comparison of V_X over different measurement sessions

Test Date	Average V_X at 2 D Downstream (cm/s)	% Difference from Session A
Session A	37.65	(0)
Session B	37.67	0.05
Session C	38.31	1.75
Session D	38.95	3.45

4.7.3.2 Quantification

If the velocity error between measurement sessions is defined as $\frac{\pm 2\sigma}{V_\infty}$ and a range of two standard deviations from the V_X mean gives a range of $\pm 1.5 cm/s$ on a mean of $38.2 cm/s$, the error is calculated to be ±4%. That is to say, comparing two V_X values taken over different measurement sessions have an expected error of ±4% due to the flume inconsistency.

Considering a hypothetical regime which was subject to this change in flume characteristics between every measurement, the deficit error would be the quadrature of the above error in V_w and V_∞ (i.e. $\sqrt{\mu_\infty^2 + \mu_{wake}^2}$). However, if each deficit is calculated using V_w and V_∞ from the same measurement session, the error may be taken as the error for V_∞ alone, i.e. ±4%. This error applies only to comparisons of deficits across measurement sessions.

The velocity deficit definition is given in Equation 2.16 and is repeated here for clarity.

$$Deficit = 1 - \frac{V_w}{V_\infty} \tag{4.2}$$

4.7.3.3 Experimental Method

Because of the variation within the flume during testing, it was decided to base results primarily on normalised data, rather than raw data, where possible. For every measurement taken as part of a wake profile, a corresponding measurement was taken in the unimpeded flume, at the same position, in the same measurement session. Thus during a single measurement session, data points were taken for the relevant configuration behind the device, then further measurements would be taken at exactly the same points with the device removed, but the flow regime kept the same (i.e. the 'unimpeded flume'). In this way the results could be normalised against the flow regime and differences caused by uncontrollable variations within the flume tank could be accounted for. Thus for V_X, velocity deficit is relied upon rather than absolute velocity, although not to the latter's exclusion.

Although the discrepancy in flume behaviour means that any direct comparison must be treated with caution, it does not exclude that comparison. When turbulence intensity is used, it is not normalised, but rather used in its raw state, and the differences of flow regime must be borne in mind. Direct comparisons are made for turbulence intensity, however these are made by comparing points within a cross flume profile, rather than making comparisons between measurement sessions. For example, it can be said that a peak exists within a turbulence profile (e.g. due to the presence of the wake), without drawing conclusions from the exact magnitude of the peak (which may be influenced by the flume inconsistency).

Both velocity deficit and turbulence intensity (defined in Equation 2.16 and Equation 5.2 respectively) are stated as decimals, where 1 is equivalent to 100 %. V_Y and V_Z measurements are also not normalised, but are presented in their raw state.

4.7.3.4 Implications

The following implications can be drawn from the above discussion on flume inconsistency:

- Indirect comparisons, for example using velocity deficits, and direct comparisons from within a single measurement session are the most accurate and trustworthy methods of data analysis.

- Velocity deficit will be the primary method of analysing wakes within the flow regime

- Turbulence intensity will also be used, but primarily through comparisons within a measurement session.

- Turbulence intensity may still be compared across measurement sessions, however at all instances when this occurs it will be noted that this is a comparison across measurement sessions.

- Similarly, where V_Y and V_Z are compared across measurement sessions it will be noted that this is a comparison across measurement sessions.

- Conclusions will be drawn from velocity deficits and comparisons across single measurement sessions.

4.7.4 Error Summary

Errors and uncertainty within the experimental setup are high, due to turbulent fluctuations and flume variability. The former applies to all velocity measurements; the latter applies only when comparing across measurement sessions. When errors are combined, they are combined in quadrature. It should be noted that comparisons are often made between profiles, and between sets of profiles, which comprise multiple points. This decreases the likelihood of errors significantly impacting the results.

Chapter 5

Pile Mounted Results

This chapter displays the results of the experiment outlined in Chapter 4. First the flume channel is profiled without any device present. Following this the wake of the device structure (with no rotor attached) is presented. Then wakes are presented for the device operating in a series of configurations: tip speed ratios of 3, 4 and 5.

5.1 Flume Channel Results (No Device)

5.1.1 Cross Sectional Profiles

Measurements were taken in the flume with the flow running at operating condition, without any turbine device or flow obstruction in place. This allowed the analysis of the flow in free stream conditions and will be referred to throughout as the unimpeded flume, the channel being empty of any impediments to the flow. Unimpeded flume measurements were taken at each point corresponding to every intended measurement point behind the turbine or structure, and these were used to analyse the flow of the channel.

Figure 5.1 shows the absolute V_X readings in the channel varying with height and width, where 0 cm is the 'near wall' of the channel and 92 cm the 'far wall'. This is taken 2 D downstream of the nominal turbine position, i.e. 2 D downstream of where the turbine would be positioned were it in the channel. It is instantly observable that there is a significant degree of non-uniformity across the channel, both in height and width.

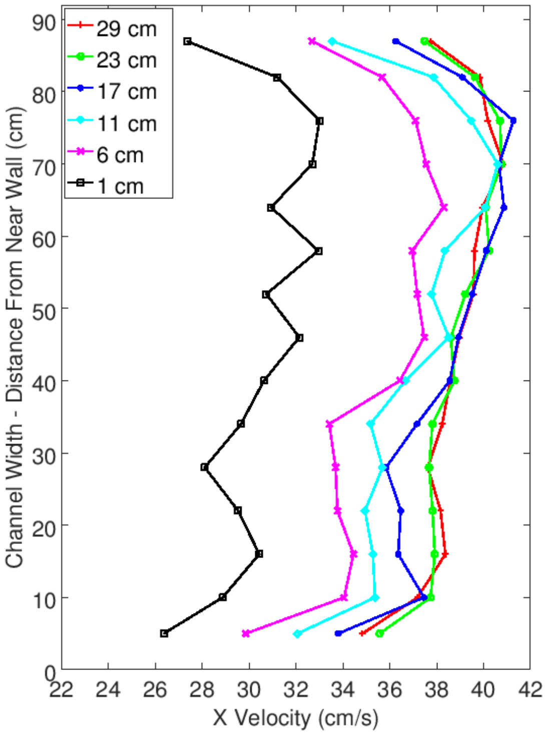

Figure 5.1: Unimpeded flume V_X at different heights, 2 D downstream of nominal turbine position

Of first note is that the velocity does not reach a peak in the centre of the channel width, but is faster close to the far wall, and slower close to the near wall. This is the case at all heights and from other results appears to be true for all distances downstream. At the height at which the turbine hub would sit if it was in place (23 cm), the peak velocity occurs 70 cm from the near wall, at 40.8 cm/s, whilst the minimum velocity (aside from the slower flow found beside the walls) is 28 cm from the near wall, at 37.8 cm/s, giving a difference of 3 cm/s across the flow. The cause of this discrepancy is likely to be the inflow of the channel: the rotational nature of the pumped flow accelerates the flow on one side of the channel slightly more than on the other. A further 25 D downstream of this, similar results occur, with a difference of 3.5 cm/s between the peak and trough at hub height (shown in Figure 5.4). This is an indication that the flow is non-uniform all the way downstream, and that this is not unique to this section of the flume.

At the top of the channel (23 – 29 cm height) the flow behaves in a similar fashion throughout. However, beneath 17 cm the flow speed decreases with depth, and the lowest speeds are recorded at 1 cm from the channel bottom, which is within the boundary layer. The velocities within the lower part of the flume are also less consistent across the width of the flume. This may be due to imperfections in the channel bottom material where small bumps occur or sections of paint are peeling, or it may be a function of the velocity intake far upstream. Further boundary layers are encountered at either wall of the flume, where the velocity slows considerably.

The same measurement points are displayed in Figure 5.2 in terms of V_Y and V_Z, drawn as a vector plot looking downstream. As explained in Section 4.5.1 measurements above 29 cm were not taken due to the probe head requiring full submersion and a blanking distance for operation. This shows further evidence of considerable asymmetry in the flow of the unimpeded flume channel, as there appears to be an eddy present. A clockwise rotation appears at the base of the channel, closer to the nearside wall. In the top portion of the channel the flow is almost uniformly moving away from the near-side, and close to the far-side wall it moves downwards. These vectors are an order of magnitude less than the velocity in the X direction. This is in keeping with Figure 5.1, where it is clear that there is a faster V_X towards the far side of the channel wall.

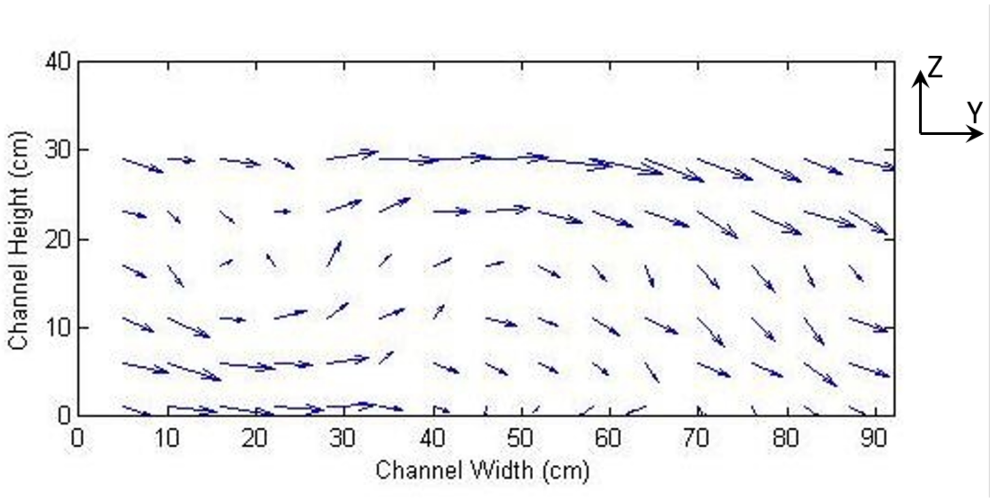

Figure 5.2: Unimpeded flume YZ velocity vectors 2 D downstream of nominal turbine position

5.1.2 Variation With Height

As can be seen from the previous figures, the velocity at the surface is higher than that at the base of the channel. This is highlighted in Figure 5.3, where the vertical velocity profile at the centre of the channel is plotted. It is shown against a 1/9th power law, commonly used to approximate boundary layers,

$$\frac{V}{V_\infty} = \frac{z}{H}^{\frac{1}{9}} \tag{5.1}$$

where V is the velocity at distance z from the channel base, V_{infty} is the freestream velocity and H the height at which the flow reaches freestream velocity. The theoretical model gives a reasonable approximation of the flow speed within the shear layer; beyond the shear layer the velocity stays reasonably constant as z increases above H.

5.1.3 Upstream Vs Downstream

A further profile was then plotted, showing the V_X profile in the unimpede flume $25D$ downstream of the nominal turbine position (Figure 5.4). As with Figure 5.1 above, the flow is faster on the far wall side, and slower on the near wall side. At

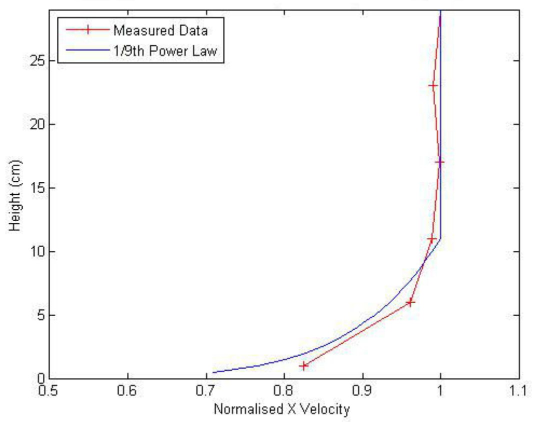

Figure 5.3: Measured and theoretical vertical velocity profiles

Table 5.1: Flume depth at different distances downstream

Distance Downstream of Nominal Turbine Position (m)	Depth (mm)
-4	395
0	402
4	406
8	416

all heights the velocities at 25 D downstream are slightly slower than those at 2 D downstream. This is likely due to viscous effects and other losses in the channel. In theory any velocity loss due to viscosity will cause a small head increase in the flow, as mass flow rate must be conserved. Although small leakages were present within the flume (in the order of cm^3/s), height measurements taken do show an increase with distance downstream, as displayed in Table 5.1. At the walls this difference is more pronounced, which is seen by much lower velocities. It is unclear whether this is a local effect caused by uneven wall surface, or whether it is the growth of the boundary layer as it travels downstream. In either case, it does not extend to the rest of the channel width. This downstream velocity difference is, along with the flume inconsistency across measurement sessions, the reason for the continued taking of unimpeded flume measurements corresponding to the wake measurements, and the use of a local normalisation value as opposed to a single upstream free stream value against which to normalise.

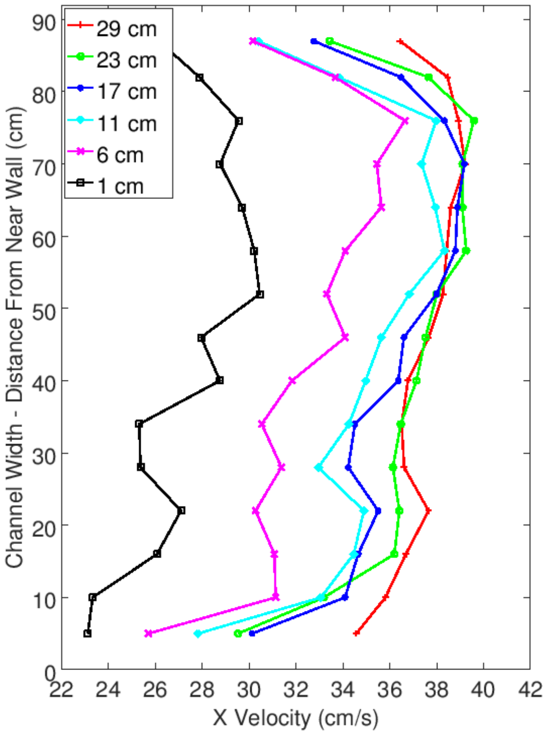

Figure 5.4: Unimpeded flume V_X at different heights, 25 D downstream of nominal turbine position

5.1.4 Turbulence Profiles

The turbulence intensity profiles within the channel have also been plotted. Turbulence intensity, I, is the ratio of the root mean square of the velocity fluctuations to the mean velocity, as given in Equation 5.2,

$$I = \frac{v'}{V} \tag{5.2}$$

where

$$v' = \sqrt{\frac{1}{3}(v_x'^2 + v_y'^2 + v_z'^2)} \tag{5.3}$$

and

$$V = \sqrt{(\bar{V}_x^2 + \bar{V}_y^2 + \bar{V}_z^2)} \tag{5.4}$$

Figure 5.5 shows the turbulence intensity across the channel at different depths, 2 D downstream of the nominal turbine position. Turbulence intensity is stated as a decimal, where 1 is equivalent to 100 %. The turbulence intensities at the bottom of the channel are much higher than those at the top. At the channel base (1 cm) the turbulence is almost 0.1, and like the velocity (Figure 5.1) is varied and inconsistent across the width of the channel. For the turbulence intensity to remain constant throughout the channel, the fluctuations would have to be lower at areas of low velocity, so as to match the higher areas of velocity proportionally. Or put another way, if the eddy sizes (and thus fluctuations) are constant throughout the cross section of the flow, the turbulence intensity will be higher at areas of low velocity, as fluctuations are proportionally larger. This is why the turbulence intensity is larger in the lower velocity areas of the flume (particularly at the walls and at the base of the flume). The turbulence decreases roughly as height increases until 11 cm from the channel bottom on the far side, and 23 cm on the near side. This further highlights the asymmetry in velocity across the width of the flume.

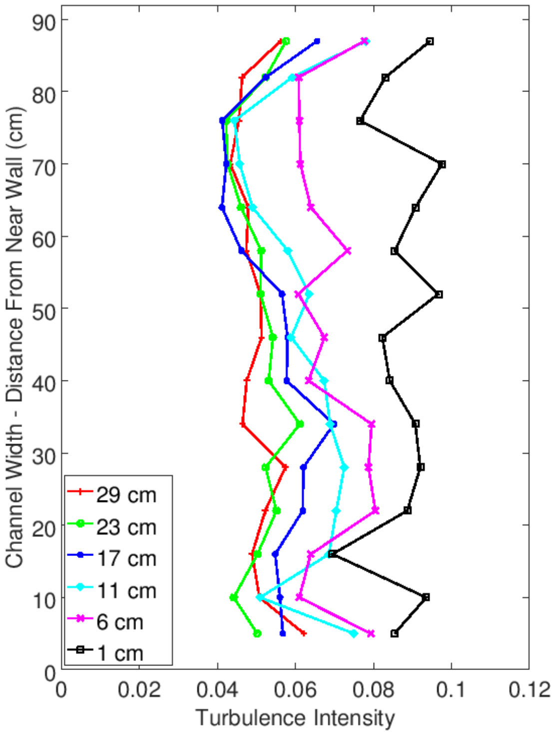

Figure 5.5: Unimpeded flume turbulence at different heights, 2 D downstream of nominal turbine position

5.1.5 One Dimensional Turbulence Intensity

Turbulence is by its very nature a three dimensional phenomenon, and anything limited to one or two dimensions is not turbulence in the strictest sense. However, it can be a useful exercise to break up the turbulence into its constituent parts. A further characteristic of turbulence in an ideal situation is that it is isotropic – the mean oscillations in each direction are the same. Isotropy occurs when the flow is a sufficient distance from screens, honeycombs or boundaries. The above Equation 5.3 is modified to contain only the fluctuations in a single direction, e.g. where

$$v'_x = \sqrt{v'^2_x} \tag{5.5}$$

The three dimensional mean velocity is retained as the denominator to give

$$I_x = \frac{\sqrt{v'^2_x}}{V} \tag{5.6}$$

In Figure 5.6 the 1D turbulence was plotted for X, Y and Z directions, at 2 diameters downstream of the nominal turbine positions in the unimpeded flume at the nominal rotor hub height. This is also compared to the 3D turbulence intensity. As can be seen I_X exceeds I_Y for most points, and I_Y in turn exceeds I_Z for most points. This demonstrates that the turbulent eddies have a larger rotation in the X direction than the other directions, and the flow is not isotropic. As eddies are formed through sheer layers it is likely that they derive from the side walls of the channel, where there is a boundary layer, and possibly from inflow conditions. The 3D turbulence lies between the higher and lower bounds of the 1D turbulence, as would be expected from an amalgamation of individual turbulence values.

As with the 3D turbulence it should be noted that 1D turbulence is a function of the mean flow velocity, and the size of fluctuation does not necessarily correspond to this. Therefore areas of low mean velocity (e.g. the far channel wall) have a high turbulence intensity, which may not be an indication of increased fluctuations, and areas of high mean velocity (e.g. inside the near channel wall) have a lower turbulence intensity, which may not be an indication of decreased fluctuations.

5.1.6 Reynolds, Froude and Turbulence Calculations

To ascertain whether the turbulence intensity values for the unimpeded flume were reasonable, an expected turbulence value was calculated. The Reynolds

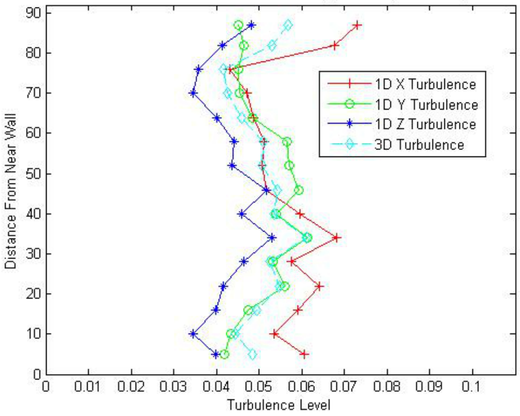

Figure 5.6: Unimpeded flume one dimensional and three dimensional turbulence, 2 D downstream of nominal turbine position, at nominal hub height

Table 5.2: Calculated approximate value for turbulence

Mean Velocity (m/s)	0.38
Area (m^2)	0.368
Perimeter (m)	2.64
Density (kg/m^3)	999
Viscosity $(Pa.s)$	0.001
Hydraulic Diameter (m)	0.5576
Reynolds Number	2.12 e05
Turbulence Intensity (%)	3.45

number of the flume was calculated as given in Equation 2.17, using the hydraulic diameter, D_h (White, 1994). Using the following formula an approximate value for the turbulence intensity could be calculated (Fluent-Inc., 2003),

$$I = 0.16 Re_{D_h}^{-\frac{1}{8}} \tag{5.7}$$

This formula assumes that the flow is fully developed, but this is unlikely to be the case due to the effects of the pump input and the inconsistencies in flume wall and base, as mentioned in Section 4.3.1.

The calculated value of turbulence (Table 5.2) is lower than the $\approx 5\%$ measured in the centre of the flume at nominal hub height (see Figure 5.6), but stands as a reasonable approximation. Both the calculated and measured values are classified as medium level turbulence (between 1–5 %).

The Froude number of the flume tank was also calculated using Equation 2.18 and found to be approximately 0.2. This is less than the 0.25 mentioned in Section 2.4.2, and the Froude number is not considered further.

5.1.7 Points of Note

The unimpeded channel is non uniform in a number of ways:

- The V_X is higher on the far wall side, and lower on the near wall side (there is a difference of 3 cm/s across the flume at hub height, Figure 5.1).
- V_X increases with height up to 23 cm (Figure 5.1).
- V_Y and V_Z contour profile shows further asymmetry in the form of an eddy in the flume (Figures 5.2).
- The V_X profile in the water column can be approximated using a 1/9th power law (Figure 5.3).
- Upstream and downstream profiles are very similar, though downstream flow is slightly slower and deeper (Section 5.1.3).
- The turbulence (or velocity fluctuation) is not isotropic (Figure 5.6).
- The most useful data comparisons will therefore be those using normalised values, i.e. velocity deficits.
- There is an opportunity to verify (or otherwise) results produced here using a flume with consistency across its profile and across measurement sessions.

5.2 Structure Results

Before examining the wake of the model tidal turbine, the impact of the structure on the flow was considered. This was achieved by removing the rotor from the device and taking measurements behind the static structure. The static structure comprises the nacelle, the pile and the anchor weight shown in Figure 4.3 (the rotor is shown in the Figure, but not present in the results of this section). A photo of the device is shown in Figure 4.1, and it is described in Section 4.1.1.

5.2.1 Velocity Profiles

As with the unimpeded flume, velocity profiles were plotted downstream of the structure to assess the wake. It was expected that the effects of the structure would be limited to the centre of the channel, so measurements were focused on that area. For further details on the measurement grid taken refer to Section 4.5. Figure 5.7 shows the V_X deficit profiles 2 D downstream of the device position at six different heights. Velocity deficit is stated as a decimal, where 1 is equivalent to 100 %. At the base of the channel, in the centre of the flow, there is a very large deficit, by far the maximum observed here. A few centimetres either side of it, towards the near or far wall, the deficit is considerably less. This large deficit is caused, not primarily by the device itself (though no doubt it is a factor), but by the anchor holding it in place. The anchor is circular, and centrally aligned, with the turbine pile rising from its centre. Therefore, with a diameter of 25 cm the anchor is only 15 cm away from the measurement point in the centre of the channel. The measurement points either side of this are much further away from the anchor, and so its effect is considerably less.

At the next height up there is also a large deficit in the centreline, but it is less than at the base. Again either side of the centreline the deficit drops, this time close to zero. Above this the centreline continues to show a deficit which quickly drops approaching either near or far wall. When measuring on the centreline at 6 cm height the probe is directly behind the pile. However, it is likely that the large deficit is caused by a mixture of the pile immediately upstream, and the anchor, which is upstream but below the measurement point. The extent to which one dominates the other is difficult to determine, but might perhaps be gauged by the deficit at heights 11 and 17 cm, where the points may be too high to be greatly affected by the anchor, and the velocity deficit is broadly consistent. At the hub height the peak deficit is very small, and beyond the hub height there appears to be no peak.

Looking at the device in place, in particular the size of the nacelle compared with the size of the pile, it might be reasonable to think that the nacelle would create a larger wake than the pile. However, this does not appear to be the case. The deficit behind the nacelle (23 cm) is considerably lower than that behind the pile, even allowing for the effect of the anchor. The highest measurement point in the centreline gives a deficit close to zero, which is consistent with expectation given that it is above the entire structure. There is, however, a small peak at this height one measurement point in from the centreline, towards the nearside wall.

Outside of the structure area the deficits are generally slightly below zero, which indicates a flow acceleration due to the structure. This is surprising as the structure is small relative to the area of the channel, with a blockage ratio of less than 4 % (including anchor).

In Figure 5.8, the YZ velocity vectors are presented, corresponding to the V_X deficit profiles given in Figure 5.7, above. Unsurprisingly, the largest vectors are those found at the base of the channel, by the anchor. The effect of the anchor manifests itself here in large V_Z values, positive in the centre, and negative on either side. As the flow travels up from the base, it also travels down from the nacelle, as the measurements behind the pile attest. The flows seem to meet just below 6 cm, and it would be reasonable to suggest that the momentum at this

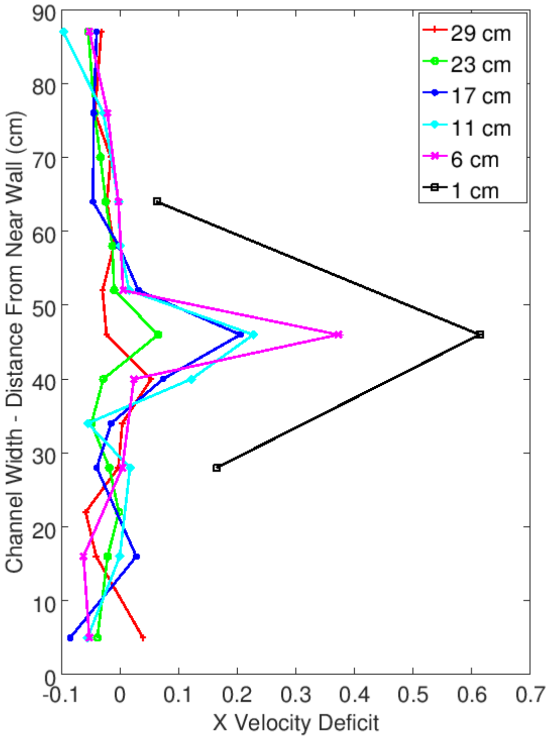

Figure 5.7: V_X deficit 2 D downstream of structure

point moves the flow towards the far wall. This plot is interesting in that whilst Figure 5.7 shows a large difference between the V_X deficits behind the pile and the behind the nacelle (e.g. at 17 cm and 23 cm height), the vector plot shows that they are very similar in the Y and Z directions.

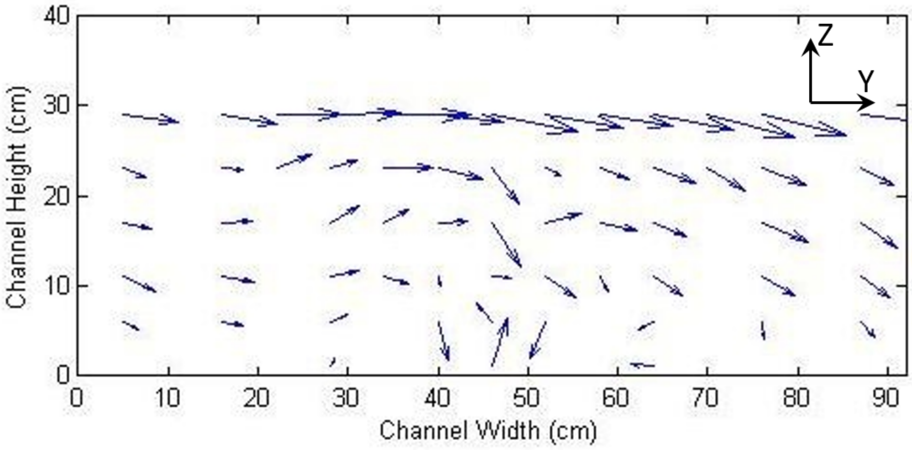

Figure 5.8: YZ velocity vectors 2 D downstream of structure

Of primary interest is the distance downstream to which the wake effects of the structure persist, and the following three plots chart this at different heights. At 1 cm from the base of the channel only three measurements were taken across the breadth of the flume, as shown in Figure 4.16. In Figure 5.9, the high immediate velocity deficit is followed by almost complete recovery a further 2 D downstream. Although this measurement was recorded 2 D downstream of the turbine position, it was less than 1 D from the anchor. This was due to the circular shape of the anchor, with the device in its centre. Immediately behind the anchor the velocity drops considerably, as it acts as a bluff body, but recovers quickly beyond this. Beyond 2 D downstream the deficits vary a small amount but show no indication that this is due to the structural wake. It appears that the wake caused by the anchor breaks down quickly and will have little bearing on the turbine measurements.

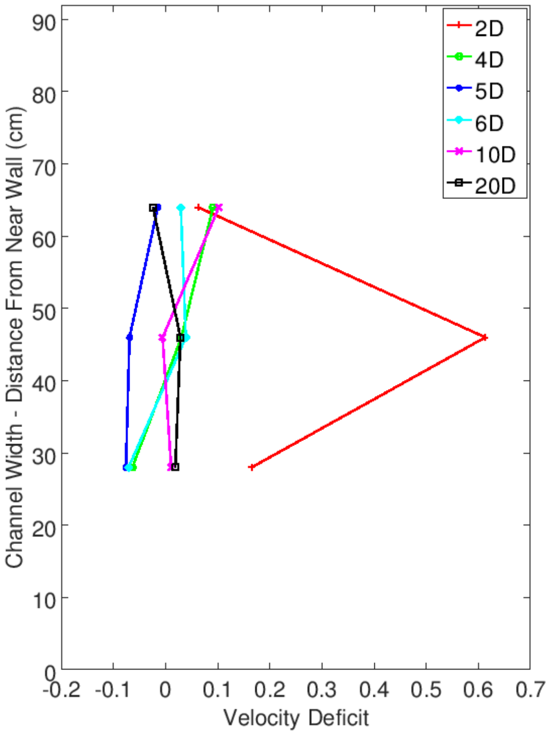

Figure 5.9: V_X deficits 1 cm from the base of the channel, behind the structure

Figure 5.10 shows the velocity deficit profiles at 6 cm height, which is behind the pile. Unlike the previous plot, the deficit is still visible from 4–6 D downstream, remaining above 0.1 whilst showing gradual recovery. Beyond this the deficit drops well beneath 0.1 and might be considered recovered. At 10 and 20 D downstream there does appear to be a small bulge at the centreline, which may be sign of the continued presence of a wake, however it should be remembered that this occurs at small deficits close to zero, and whilst it will be borne in mind during comparisons to other configurations, it is unlikely to be the result of the persistent wake of the structure. At the nearside of the flume there is evidence of an area of variability in the flume section, 16 – 26 cm from the near wall. This area of increased variability is also visible to a lesser extent at hub height (Figure 5.11) and is a feature of the flume, which may be caused by the caused by the flume inlet. The lower flow speed on this side of the channel magnifies the variance within the velocity measurements.

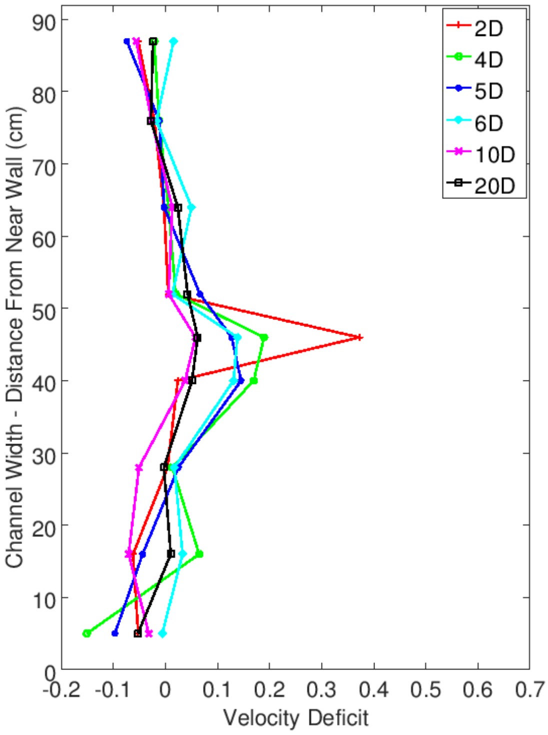

Figure 5.10: V_X deficits 6 cm from the base of the channel, behind the structure

Figure 5.11 shows the same plot for a height of 23 cm, the hub height. As mentioned above, the deficit immediately behind the device was small, therefore any wake further downstream would also be small. All measurements fall between 0.1 and – 0.1, with most being close to zero. In the centreline there is an area of recovery to 4 D downstream, but beyond this the points are scattered within a small range around zero. On the far side of the turbine area there is agreement between all distances downstream, but on the nearside there is a wider spread, as part of the increased variance in the flume at this point. Variance at hub height is not as large as the variance seen at 6 cm depth.

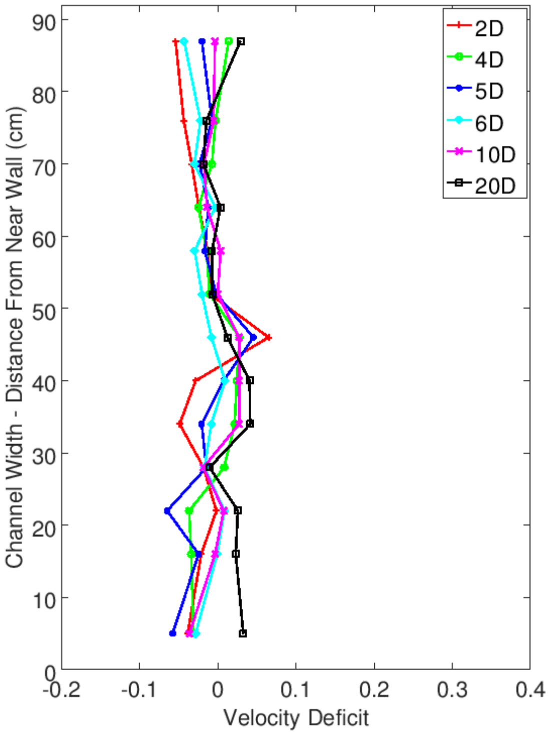

Figure 5.11: V_X deficits 23 cm from the base of the channel, behind the structure

Though it appears that the pile contributes the most significant part of the wake of the structure, no measurements were taken of the wakes behind the individual constituent parts of the structure (the anchor, the pile and the nacelle). A theoretical approximation for the rate of velocity deficit recovery in the wake behind a cylinder in a turbulent flow is given by Schlichting (1979) as

$$Deficit \propto x^{-\frac{2}{3}} \tag{5.8}$$

where x is the distance downstream. In Figure 5.12 this is compared to the wake measurements in the central width of the flume at 17 cm from the base of the channel (i.e. behind the pile). The theoretical prediction is normalised against the measured result at 2D downstream.

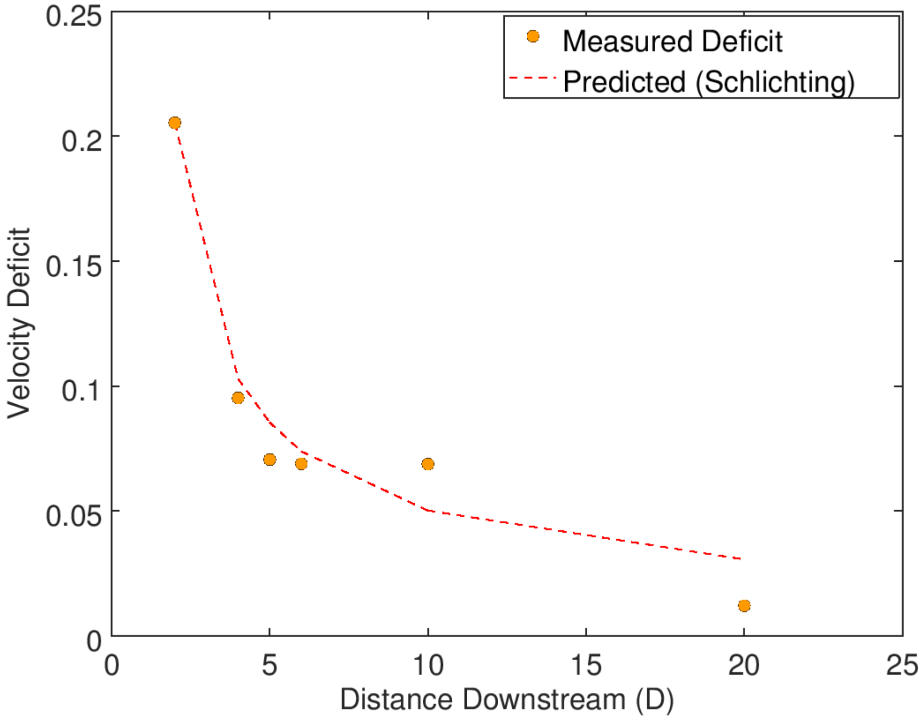

Figure 5.12: Velocity deficit in the wake of the pile at 17 cm height (circles) and theoretical prediction (solid line)

Here it can be seen that the wake recovery of the whole structure corresponds approximately to that of the predicted wake of a cylinder, which supports the possibility that the pile makes the most significant contribution. It is likely that the cylindrical pile induces vortex shedding (as occurs around a cylinder), at a magnitude that the nacelle does not.

5.2.2 Turbulence Profiles

The turbulence profiles behind the structure were then compared to those of the unimpeded flume to ascertain the magnitudes of turbulence generated by the de-

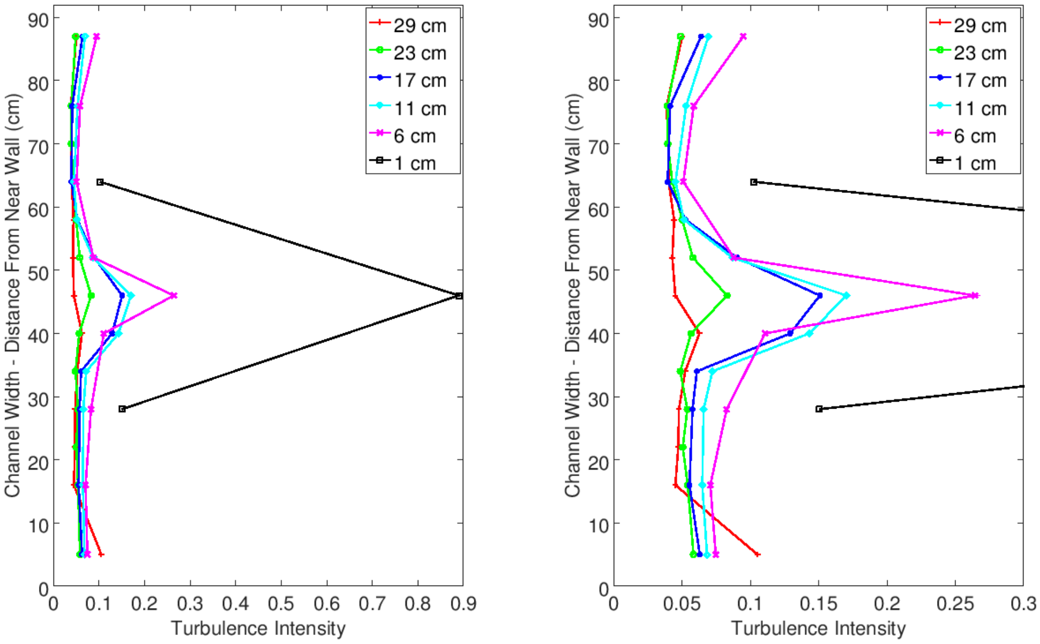

(a) Showing all measurements

(b) Scale reduced to exclude maximum

Figure 5.13: Turbulence intensity 2 D downstream of the structure at different heights

vice and to assess its break up. Figure 5.13 shows the turbulence intensity profiles at different heights, 2 D downstream of the structure. Again, the turbulence is largest at the base of the channel, immediately downstream of the anchor, where it approaches one. This means the fluctuation term is almost as large as the mean velocity term. Similar to Figure 5.7 the turbulence is markedly lower at every other point, indicating that the peak is caused by the anchor.

In the vertical centreline the turbulence decreases with height, though minimally between 11 and 17 cm, where the turbulence generated by the pile is close to constant, and not affected by the anchor. Recalling Figure 5.5, the turbulence intensity in the unimpeded channel decreases with height until 17 cm, explaining the small difference between the points at 11 and 17 cm in Figure 5.13. At hub height there is a turbulence intensity of 0.083, compared to the corresponding value of 0.054 taken in the unimpeded flume during the same measurement session.

The turbulence intensity at 6 cm height was plotted to further visualise the breakup of the wake (Figure 5.14). Corresponding to Figure 5.10 there is a large peak immediately downstream of the pile, followed by a much smaller peak at 4 D downstream, then a gentle recovery beyond. By 10 D downstream the turbulence from the pile has dissipated. Note that this compares turbulence across multiple measurement sessions.

It is interesting to note that the peak turbulence intensity caused by the pile is relatively much larger than the peak velocity deficit. In the centre of the channel the velocity deficit decreases by 49 %, whilst the turbulence intensity decreases by 70 % (assuming a datum turbulence intensity of 0.06). This is likely to be because the turbulence follows the Batchelor spectrum as it breaks down, where energy passes to higher and higher frequency eddies (Tennekes and Lumley, 1972). As soon as energy passes to eddies of a frequency higher than the Nyquist frequency (in this case 12.5 Hz), it becomes undetectable (Luke, 1999). Whilst this energy is still within the system, it cannot be seen and so appears to have dissipated; though in reality it is still present in the form of small scale rotation. Therefore in this experimental configuration it may be more appropriate to consider the velocity deficit over the turbulence intensity as a quantity in which to search for evidence of the longevity or otherwise of the wake.

The above has shown that the structure had little influence at the hub height, and it was expected that the rotor would have most influence at that height. Therefore, for most analyses the hub height was used as the primary indicator of the wake of the blades, although other heights were also examined.

5.2.3 One Dimensional Turbulence

As with the unimpeded flume, the three dimensional turbulence was divided into three constituent parts (Figure 5.15, below). Again, in the free flowing areas of the channel, I_X is generally higher and I_Z generally lower than I_Y and the

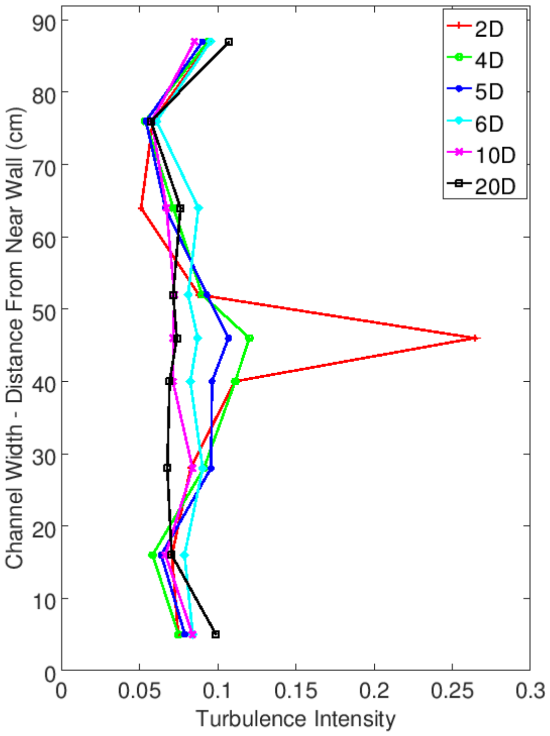

Figure 5.14: Turbulence intensity 6 cm above the channel base, behind the structure

3D turbulence. However, behind the device structure I_Y is larger, indicating an increased relative fluctuation in the Y direction. The absolute flow velocity in the Y direction is also greatly increased as the fluid is forced around the structure. It might have been expected that a similar trend would be observed in I_Z as the fluid is forced over the symmetrical structure of the nacelle, however it is not nearly so pronounced. It is postulated that this effect is a result of interference from the pile, as the pile is a symmetrical cylinder, liable to the shedding of vortices which will share the axis of the pile. However, no measurements were taken of the pile on its own to confirm this.

A point directly behind the pile, at 2 D downstream, can be seen in Figure 5.16, where V_Y is shown in the frequency domain, indicating evidence of the vortices. Here there are a series of large spikes at approximately 2, 4, 5.5 and 6 Hz, which is likely due to vortex shedding. A vortex shedding frequency of 2 Hz corresponds to a Strouhal number (as described in Section 2.4) of approximately 0.1.

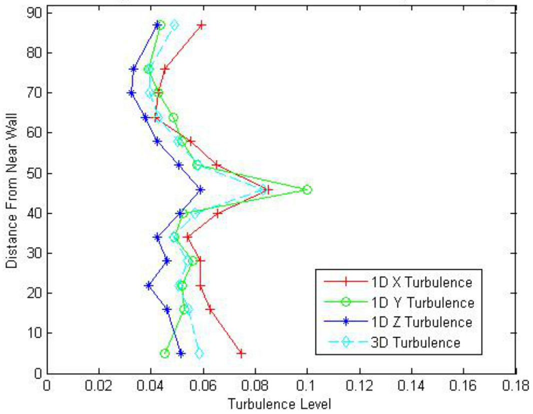

Figure 5.15: One dimensional turbulence intensity, 2 D behind the structure

5.2.4 Points of Note

- The wake of the pile is postulated to be more significant than that of the nacelle, however further experimental work would be required to confirm

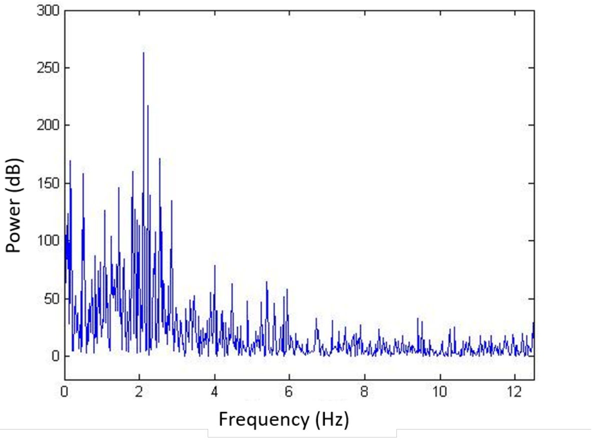

Figure 5.16: Fast Fourier Transform (FFT) of V_Y directly behind the pile, with the turbine not operational and blades removed

this.

- At hub height the deficit never goes above 0.1 (i.e. it is very small; Figure 5.7).
- The wake of the structure is small, the majority of the flow having recovered between 6–10 D downstream (or earlier at the rotor height; see Figure 5.11).
- The wake of the structure at hub height is small, though below the nacelle vortex shedding is observed from the pile (Section 5.2.3).

5.3 Standard Device Results ($\lambda = 4$)

The turbine blades were then attached and the device was set to run at a tip speed ratio of four, with wake measurements being taken as before. The turbine was run at a rotational speed of 116 rev/min. This gave a tip speed of 1.5 m/s. With a free stream velocity, V_∞, of approximately 0.38 m/s, the tip speed ratio was four.

As with previous tests, velocity measurements were taken at various points behind the device, building up a series of cross sectional grids. These were complemented by measuring the same points and building up the same grids with the turbine removed. V_X in the wake could then be normalised, and V_Y, V_Z and the turbulence intensity could be directly compared with the corresponding point in the unimpeded flume.

5.3.1 Velocity Profiles

Normalised V_X profiles were plotted at hub height across the flume for varying distances downstream, shown in Figure 5.17. The measurements stretch from 2 D downstream of the device to 25 D downstream of the device, and from 5 cm from the near wall to 5 cm from the far wall. At 2 D downstream of the device there is a large deficit at the centreline, and a close to free stream velocity in line with the blade tips, i.e. no deficit. Beyond this, on either side of the rotor there is a negative deficit, which shows there is some flow acceleration due to the device. Further downstream the measurements within the rotor area tend to decrease in deficit, and the measurements out with the rotor area tend to increase, thus both are recovering to free stream.

The lowest measurements of deficit in the rotor area occur at 25 D, the furthest distance downstream, demonstrating continuous wake recovery from 2 to 25 D. Figure 5.18 gives the velocity deficit in the centreline of the flume, directly behind the device. In it the deficit drops from 0.26 at 2 D downstream, to 0.04 at 25 D downstream. With two exceptions, there is continual recovery. In the near wake the recovery is quick, whilst in the far wake it is more gradual. Velocity deficit has recovered to < 0.1 by 13 D downstream. This is comparable to results found in Stallard *et al.* (2013) (by 14 D) and Chen *et al.* (2017) (by 12 D). However, there is significant uncertainty present, due to the comparison between different measurement sessions and the turbulent fluctuations in the velocity (Section 4.7).

Given the measurement resolution, any quantification of wake expansion becomes troublesome. However, some evidence may be seen on the nearside, behind the rotor tip. Figure 5.19 shows the location of a measurement point proximate

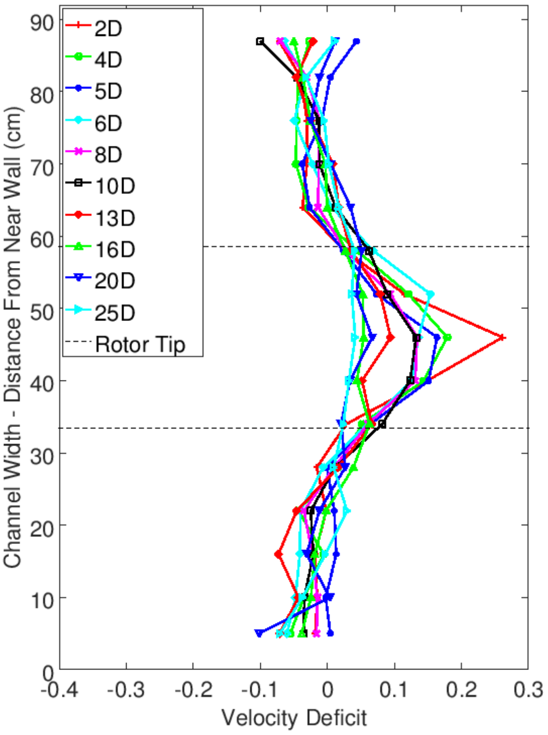

Figure 5.17: V_X deficit profiles at hub height for standard case ($\lambda = 4$)

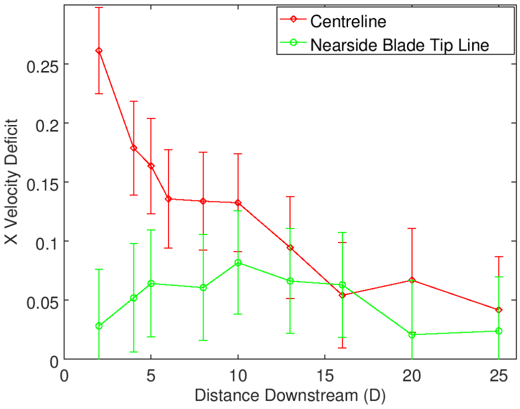

Figure 5.18: V_X deficits in the channel centre and the nearside blade tip line at hub height for standard case ($\lambda = 4$)

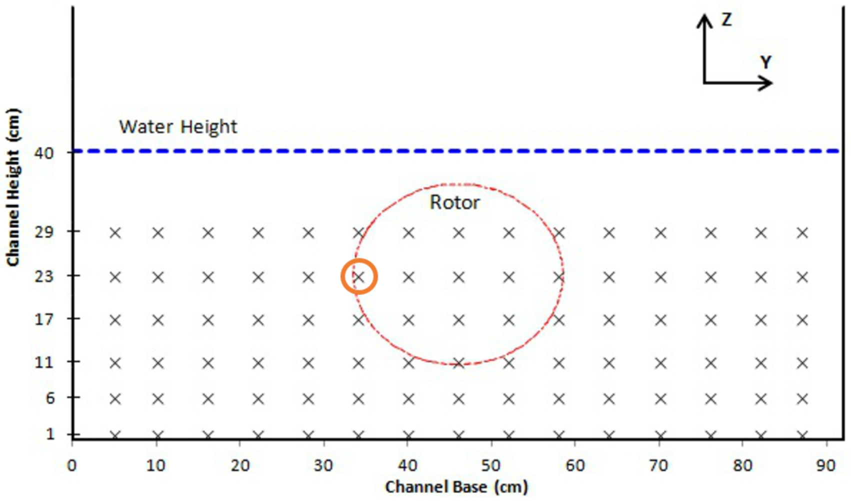

Figure 5.19: Measurement grid positions (as per Figure 4.14) highlighting the nearside blade tip measurement location

to the nearside rotor tip. In Figure 5.18, the deficit behind the nearside rotor tip increases until 10 D downstream, where it begins to decrease. It is expected that within the first 10 D the wake is spreading out from the centreline to the blade tip line, and beyond this the wake is recovering at the blade tip line.

The acceleration caused by the device appears to extend from the first points outside of the rotor area to the points by both channel walls. There is a large dispersion of results at both channel walls. Whilst a majority of the points are negative, thus the flow is accelerated, no obvious relationship presents itself. Instead, it can be explained by the lower free stream velocities at the walls. The deficit is calculated by dividing the wake velocity by the unimpeded flume velocity at the corresponding point, for reasons explained in Section 4.7.3. Therefore, at a point where the unimpeded flume velocity is lower, the deficit will be susceptible to larger changes when the wake velocity varies. A further reason for the wide spread of results at the walls is the varying surface qualities at different areas downstream. At some measurement points the wall is smooth and clean, whilst close to others there are joins in panels, steel supports and even small bolts. These are not expected to greatly vary the channel flow as a whole, but may slow down or speed up the local flow. As previously stated, a change in the free stream velocity means a change in sensitivity of the velocity deficit.

At 20–25 D downstream, the flow has recovered much of its velocity, but there is still a deficit. Figure 5.20 compares the absolute velocities at the furthest two distances downstream with the corresponding unimpeded flume velocities. From this the flow in the wake of the device is clearly slower than the flow of the unimpeded flume in the rotor area. Out with the rotor area there is still evidence of flow acceleration at 20 D downstream, but this appears to have been dissipated by 25 D, where it cannot be seen.

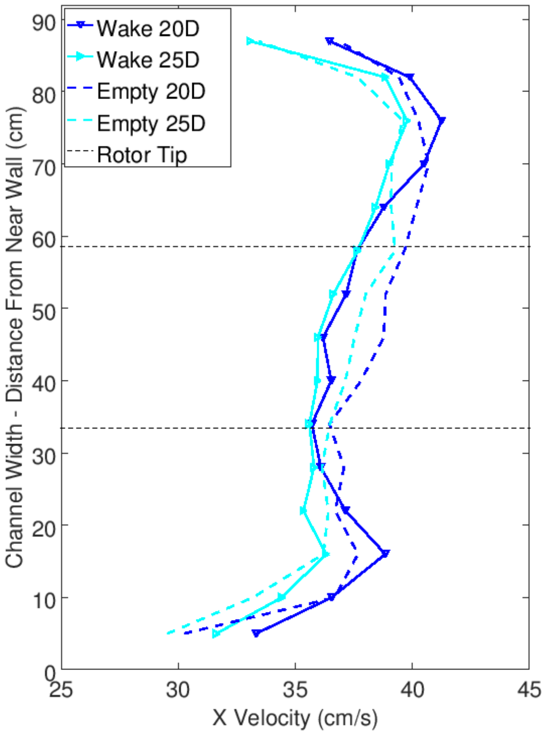

Figure 5.20: Comparing absolute V_X values for the unimpeded flume and the standard case ($\lambda = 4$) far downstream

5.3.2 Turbulence Profiles

In a similar fashion, the turbulence intensity profiles at hub height were plotted (Figure 5.21). This compares different measurement sessions, and it should be remembered that whilst velocity deficit is a normalised value, turbulence intensity is absolute in that it is not benchmarked against the unimpeded flume, or already present turbulence.

At 2 D downstream of the device there is high intensity in the centreline of the channel, at 0.14. This is greater than the turbulence intensity of the structure in Section 5.2, which is 0.08. Within the rotor area the turbulence intensity drops considerably in either direction (towards the near or far wall). Downstream of this the centreline peak is not nearly so pronounced, and by 8–10 D there is no peak as such, but a raised turbulence intensity across the rotor area. The intensity then falls with distance downstream. On either side of the rotor area there is a clear curve where the turbulence drops to a local minimum before increasing again at the wall. The curve on the far wall side displays a good level of consistency regardless of distance downstream, and whilst the curve on the near wall side is more disparate there appears to be no obvious relationship with respect to distance downstream. The similarities of the turbulence intensities in these areas indicates that the device has little effect on the turbulence in these areas.

The increase in turbulence intensity at both walls is due to the lower velocities in these areas. That the turbulence intensities in these regions are more spread out is again attributable to turbulence being more sensitive in lower velocity regions. This is also why the curve by the far wall is more uniform than the curve by the near wall; it is situated in a higher velocity area.

Figure 5.22 shows the turbulence intensity in the channel 20–25 D downstream of the turbine position at hub height, comparing the turbulence in the unimpeded flume with that in the wake of the turbine. Although the profiles are similar, there is noticeable difference. In both instances the near side of the channel, the slower side, shows no difference in turbulence, but on the far side of the channel the unimpeded flume turbulence is lower than that behind the turbine. This is further indication of the presence of a wake far downstream. That the wake is found on the far side of the channel as opposed to the near is in line with the analysis of the unimpeded flume. The inherent flow in the Y direction (towards the far wall) will push the wake away from the centreline.

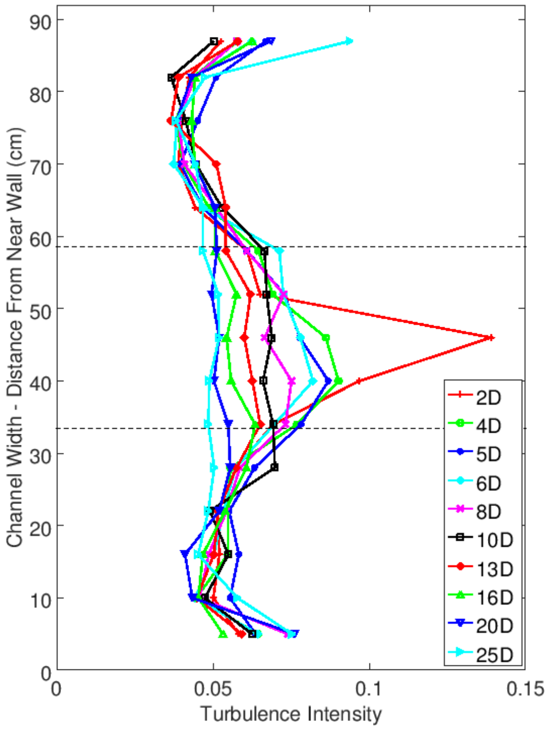

Figure 5.21: Turbulence intensity profiles at hub height for the standard case ($\lambda = 4$)

5.3.3 One Dimensional Turbulence

Figure 5.23 below plots the 1D turbulence intensity for the standard case. As with the previous examples, the measurement points are taken across the flume channel at hub height. As is shown in Figure 5.21 the turbulence behind the operating device is much greater than behind the static structure. Again I_Y exceeds the turbulence in other directions. Taking the unimpeded flume results (Figure 5.6) as the base case, the turbulence levels behind the structure can be compared to those behind the standard case (Table 5.3). Behind the device, on

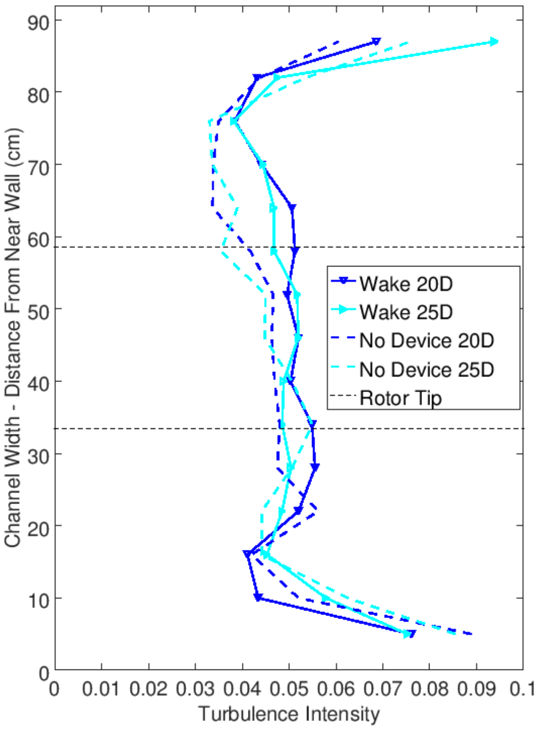

Figure 5.22: Comparing turbulence intensity values for the unimpeded flume and the standard case ($\lambda = 4$) far downstream

Table 5.3: Turbulence increase from the structure to the standard configuration

Turbulence	% Increase from Structure to Standard Configuration
I	196.6
I_X	160.4
I_Y	147.9
I_Z	794.8

the rotor rotational axis, the 3D turbulence increases by 197 %. I_X and I_Y also increase, by a smaller amount, whilst I_Z increases greatly. The increase in I_Z is due to the turbulence added by the rotor, which generates fluctuations in all directions.

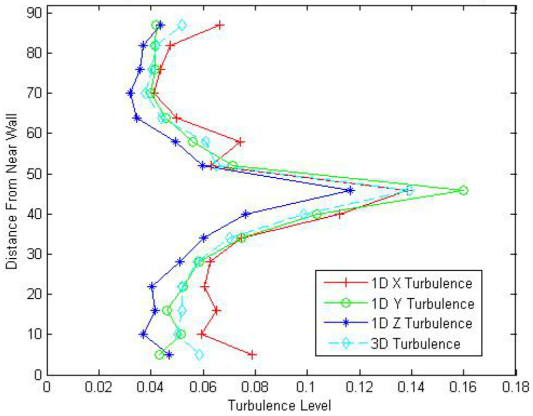

Figure 5.23: One dimensional turbulence for the standard case ($\lambda = 4$) at 2 D downstream

5.3.4 Velocity Vectors

As above, velocity vectors were plotted to display the V_Y and V_Z in various cross sections of the flow. Figure 5.24 shows the flow 2 D downstream of the device. The central circle represents the swept area of the rotor. It should be remembered that conservation is not required in this plot, as the V_X is not shown. The flow can be seen to be moving from the near wall towards the far wall, as occurs in Figures 5.2 and 5.8. Comparing with the unimpeded flume cross section (Figure 5.7) there is a more uniform spread on either side of the rotor area, where before there was a large swirl. The influence of the turbine is visible in that in the centre of the rotor area the rotation can be made out, the flow moving clockwise as it travels downstream. This is comparable to Figure 5.2 where minimal clear rotation is apparent in the equivalent area of the flume. By 4 D downstream (Figure 5.25) the central swirl has dropped in size, and by 10 D (Figure 5.26) it has all but disappeared, leaving no visible trace of the wake of the turbine using this method of visualisation.

Due to the blanking distance mentioned in Section 4.4.2, velocity measurements for the top section of the rotor area and flume were not taken. Thus there is no data at the top of the flume. Data from this area could have provided some indication of the impact of the free surface on the wake. It would also have provided further information on the V_Y aspect of the flow across the channel, and a fuller picture of the rotational effects of the rotor at 2 D downstream. However, the most significant results obtained are those at hub height (e.g. Figure 5.17), which show the deficit as it travels downstream, and on which the conclusions are based.

It should be emphasised that these plots present the average velocity vectors, as opposed to the instantaneous vectors, therefore time variant eddies will not be shown unless they are consistent enough to dominate the average.

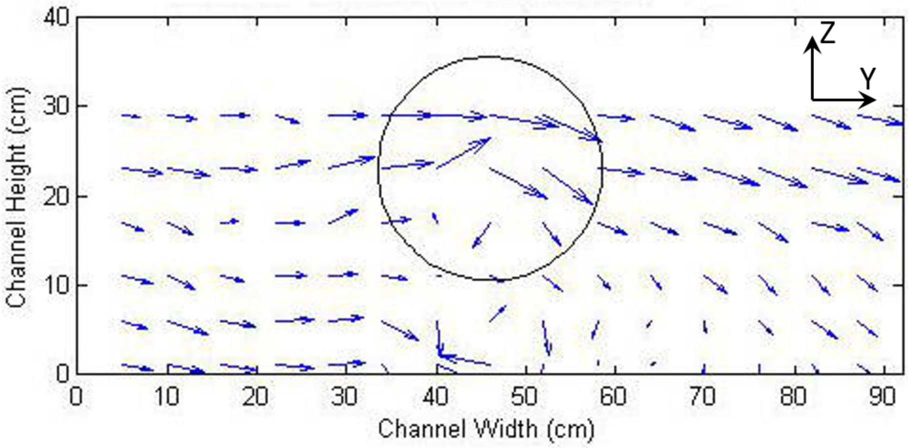

Figure 5.24: YZ velocity vectors for the standard case ($\lambda = 4$) at 2 D downstream

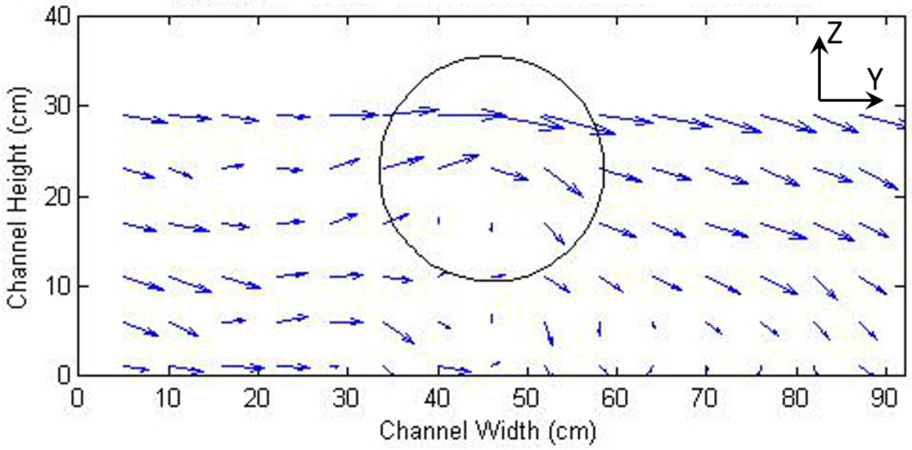

Figure 5.25: YZ velocity vectors for the standard case ($\lambda = 4$) at 4 D downstream

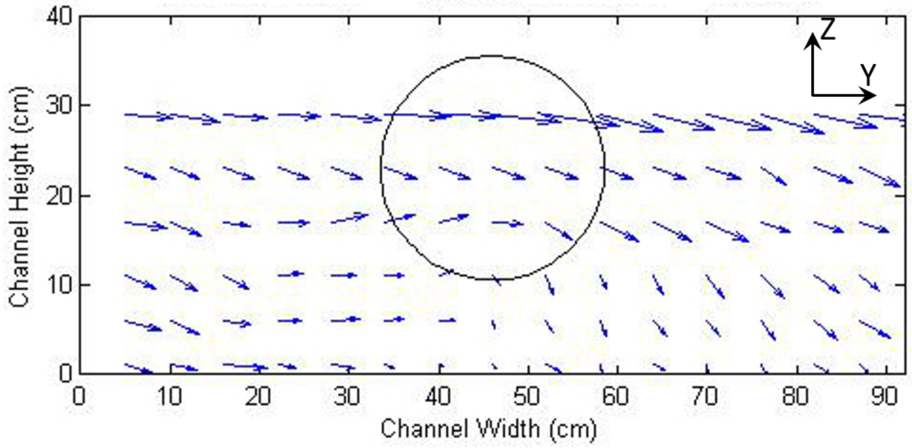

Figure 5.26: YZ velocity vectors for the standard case ($\lambda = 4$) at 10 D downstream

5.3.5 Upper Flow vs Lower Flow

In Figure 5.27, the horizontal profiles of the V_X deficit at 2 D downstream are plotted for different heights within the channel.

Along the centreline the larger deficits occur towards the base of the channel, the highest peaks being at 1 and 6 cm. The deficits towards the top of the channel are lower, even though they are directly behind the rotor. This is due to the presence of the structure and anchor, as discussed in Section 5.2, and the lower velocities at the bottom of the tank, as discussed in Section 5.1. When compared to Figure 5.7 it is clear that the velocity deficit at the channel base is lower for the standard case. As the comparison is being made over different measurement sessions, this may be due to the flume inconsistency. However, for every height above this the standard case velocity deficit is greater. Furthermore, there is increased evidence of flow acceleration around the device, seen in the negative deficit on either side of the rotor.

For 0.5 D either side of the centre of the flume it would be reasonable to expect the wake to be largest at hub height, where rotor tips ‘reach out’ furthest. This is the case above the gravity anchor, although the effect is not as pronounced as might be anticipated (Figure 5.28). Outside of the rotor area there are consistent negative deficits, meaning flow acceleration is taking place. This occurs equally on both sides of the rotor, with little difference due to depth.

Further downstream, the centreline velocity deficit has dropped considerably at the base of the channel, whilst dropping considerably less at the rotor heights (Figures 5.29 and 5.30). At 10 D downstream the largest deficits can be found across the rotor area at 23 cm height (hub height). Here the wake of the turbine dominates over the wake of the structure. A slight flow acceleration appears to remain outside of the rotor area at 4 and 10 D downstream, and is more pronounced on the near wall side.

Figures 5.27, 5.29 and 5.30 (the deficit depth profiles) can be compared to

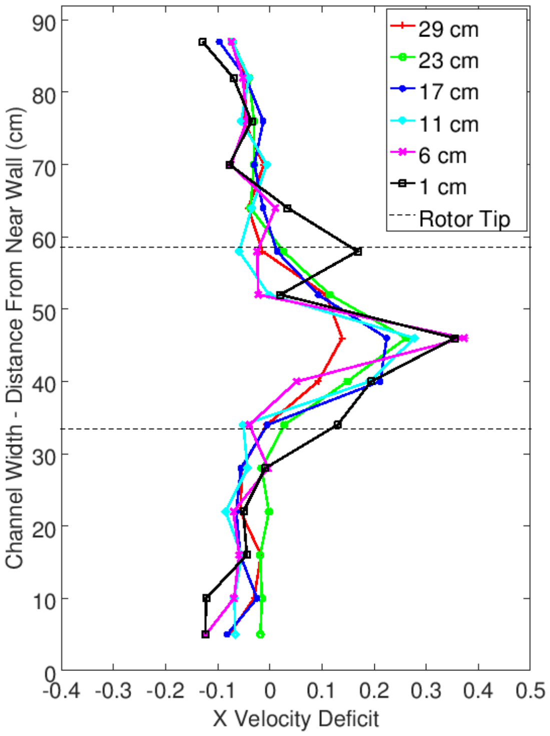

Figure 5.27: V_X deficit profiles for the standard case ($\lambda = 4$) at 2 D downstream

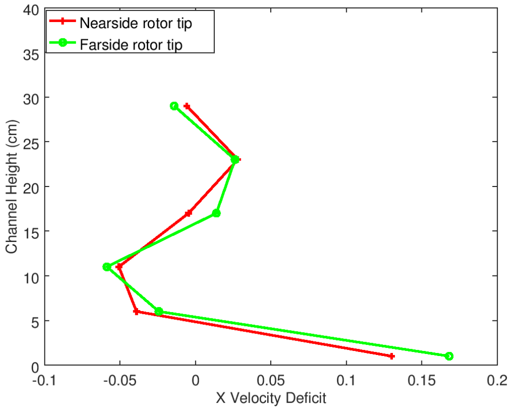

Figure 5.28: V_x deficits at the near and far side rotor tips 2 D downstream of the standard case

Figures 5.24, 5.25 and 5.26 (the velocity vectors), as they cover the same area (although the former are normalised whilst the latter are not).

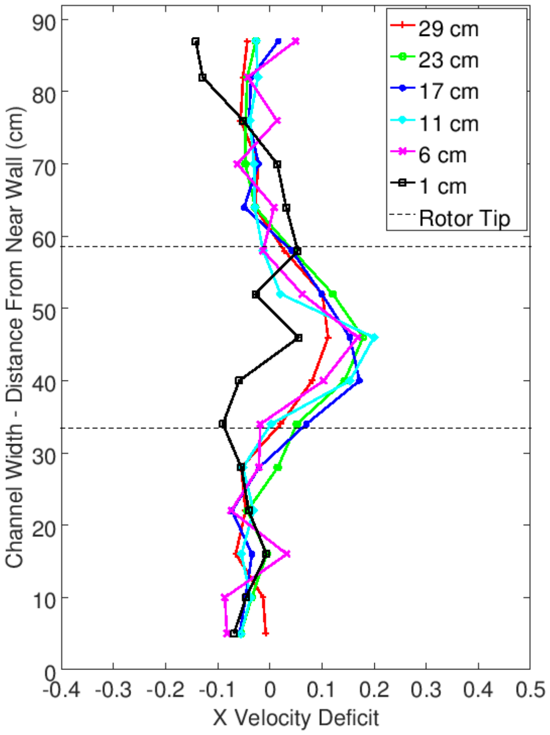

Figure 5.29: V_X deficit profiles for the standard case ($\lambda = 4$) at 4 D downstream

5.3.6 Blockage

In Figure 5.17 an acceleration was seen on the near and far side walls, and on the far side of the channel, continuing downstream. At the boundaries the relatively slow flow was re-energised, and remained so for most of the distance downstream. On the far side of the flume the flow increase was not particularly high, but was significant in that it did not recover quickly. The blockage ratio was 13 %, and no change in surface elevation was noted at any point.

The wake recovery may have been slightly slowed due to the shallowness of the flume. The water height was 1.6 D, and Myers, Bahaj and Germain (2008) suggests that any depth less than 4 D may reduce the rate of wake recovery by

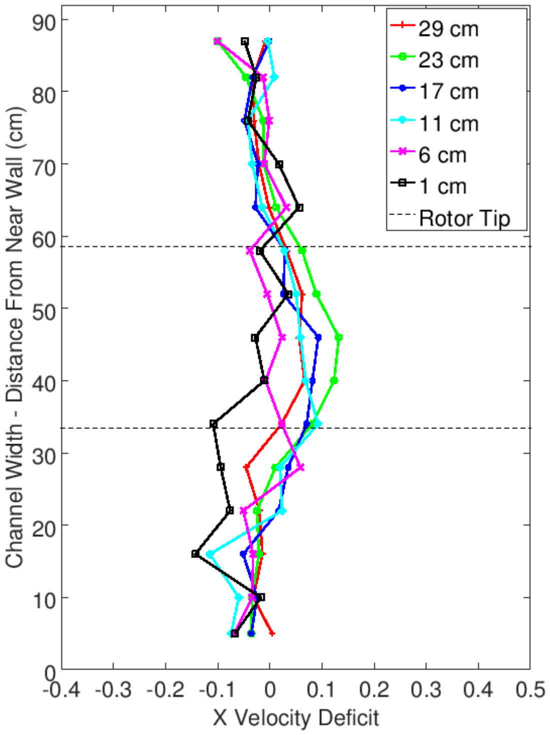

Figure 5.30: V_X deficit profiles for the standard case ($\lambda = 4$) at 10 D downstream

inhibiting mixing below the turbine due to the bottom boundary layer. Whilst this may have retarded recovery somewhat, and it is expected that full scale devices will be positioned in flows deeper than 1.6 D, it is highly plausible that they may positioned in flows shallower than 4 D. A 20 m diameter rotor (e.g. approximately 1 MW) might well be located in a water depth of less than 40 m, and certain specialised devices might be installed in far shallower waters, decreasing the wake recovery in a manner comparable to this experimental work.

5.3.7 Coefficient of Thrust

Using Equation 2.13, an approximation of the coefficient of thrust was calculated from the free stream and wake velocities. The C_T was found to be 0.45, which is similar to that used in Currie, Osbourne and Grouix (2016) and Chen *et al.* (2017). However, this is likely to be an underestimate, as measurements for V_w were not taken immediately downstream of the rotor, but were taken 2 D downstream, where some velocity recovery has already taken place. A more accurate value of C_T could have been obtained by gauging the device and measuring the bending applied to the turbine strut. Blockage has not been corrected for, but its effects are likely to be small.

5.3.8 Points of Note

- The highest velocity deficits occur in line with the centre of the rotor; in line with the blade tips the deficit is ≈ 0 immediately downstream of the rotor (Figure 5.17).
- Wake recovery is seen from 2 D to 25 D, recovery is faster close to the rotor and slower further downstream (Figure 5.17).
- However, there is significant uncertainty in the measurements (Section 5.3.1)
- Some flow acceleration is noted around the device (Figure 5.17).
- Wake mixing causes the deficit in line with the blade tip to increase until about 10 D downstream, where it begins to decrease (Figure 5.18).
- Deficit recover is in line with other experimental work found in literature (e.g. Stallard *et al.* (2013) and Chen *et al.* (2017)) (Section 5.3.1).
- There is still evidence of the wake at 25 D downstream (Figures 5.20 and 5.22).
- The rotation of the wake in the YZ contours is evident at 4 D but not at 10 D (Figures 5.25 and 5.26).
- The low depth to rotor diameter ratio may inhibit wake recovery (Section 5.3.6).

5.4 Alternative Rotational Configurations ($\lambda = 5$, $\lambda = 3$)

The device was then run in two further configurations. The rotational speed of the device was increased whilst keeping all other set-up constraints constant, so as to give a tip speed ratio of five, and the wake was measured in the usual fashion. The device was also run at a tip speed ratio of three. These wakes behind the device were analysed and presented as follows. At these speeds the thrust coefficients were calculated to be 0.48 and 0.40 for $\lambda = 3$ and $\lambda = 5$ respectively. As noted in Section 5.3.7 this method is likely to underestimate the C_T as velocity measurements were not taken immediately behind the rotor, but taken 2 D downstream, where some velocity recovery has already taken place.

5.4.1 V_X Profile

The normalised V_X deficit profiles for the $\lambda = 5$ configuration were plotted in Figure 5.31. These follow a similar shape to Figure 5.17. At 2 D downstream there is a large deficit in the centre of the channel, which falls to zero approaching either blade tip line. Outside of the rotor area the deficit is negative, thus flow acceleration is present. For all distances downstream a similar pattern is observed, though the deficit peak behind the device spreads over the rotor area with distance downstream. At 20 D there is still a deficit of 0.06 in the centreline.

Acceleration can be seen outside of the rotor area at distances near to the device, but it recovers with distance downstream. There is some evidence to suggest that the wake drifts towards the near wall as it travels downstream. At 13 D downstream the maximum velocity deficit is found to the nearside of the centreline, and at 20 D downstream the total deficit shape extends beyond the rotor area towards the nearside wall. The measurements taken at 13 and 20 D downstream were compared in absolute terms, shown in Figure 5.32. At these distances downstream there are still large differences between the velocity in the unimpeded channel and that behind the device, indicating the continued presence of the wake. The recovery between 13 and 20 D downstream is modest. Again, the expansion of the wake has occurred towards the near wall, but not towards the far wall.

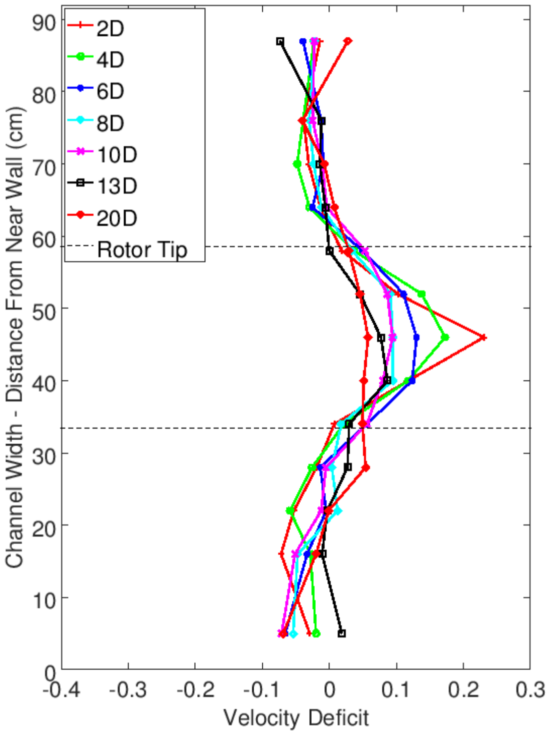

Figure 5.31: Hub Height V_X deficit ($\lambda = 5$)

Figure 5.33 shows the wake recorded behind the device running at $\lambda = 3$. Data was not taken at 2 D downstream of the device, but beyond this a similar picture is drawn to those previously described. A sharp peak in the centreline immediately downstream of the device gives way to a more dispersed wake further downstream. Flow acceleration is noted outside of the rotor area. Wake expansion on the far wall side is non-existent, and is very mild if present at all on the near wall side. At 13 and 20 D downstream the wake is evident (Figure 5.34), again displaying a drift towards the near wall. The recovery between 13 D and 20 D is more pronounced than for the $\lambda = 5$ configuration, but this is to be expected as

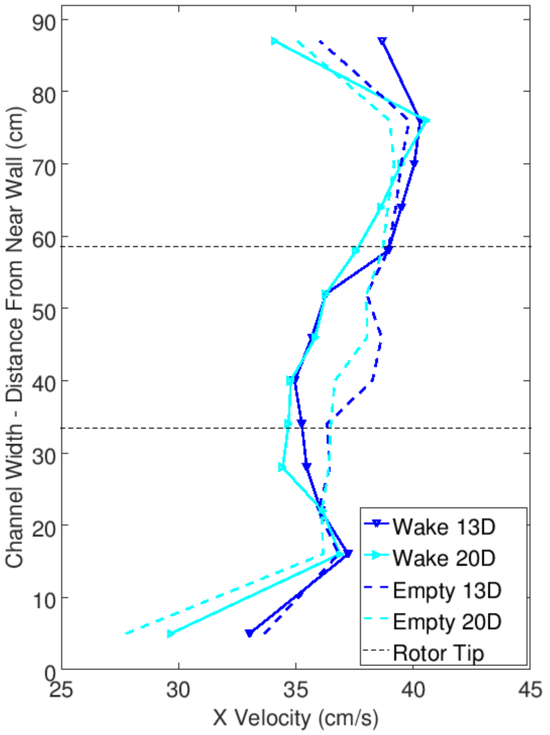

Figure 5.32: Hub Height V_X comparing wake with unimpeded flume ($\lambda = 5$)

the velocity deficit is larger for $\lambda = 3$ at these distances downstream.

One further aspect of the wakes of the three different configurations is compared directly, in Figure 5.35. This shows the V_X deficit in the centreline of the channel at hub height. Immediately of note is that the deficit of the lower speed configuration is larger than that of the higher speed configurations. This is contrary to expectations, as it would be reasonable to believe that a faster rotation would lead to a higher thrust, and thus a larger wake. A possible explanation for this lies in the unusual blade shape (an inverted propeller). A tip speed ratio of four was chosen as it was estimated that this would be somewhere close to the peak thrust coefficient value, and thus a decrease in tip speed ratio would lead to a decrease in thrust, decreasing the profile of the wake. However, if the datum tip speed ratio (4) corresponded to a point beyond the maximum thrust coefficient, any decrease in tip speed ratio would lead to an increased thrust, and therefore an increased wake deficit profile. This may be the case here, where the

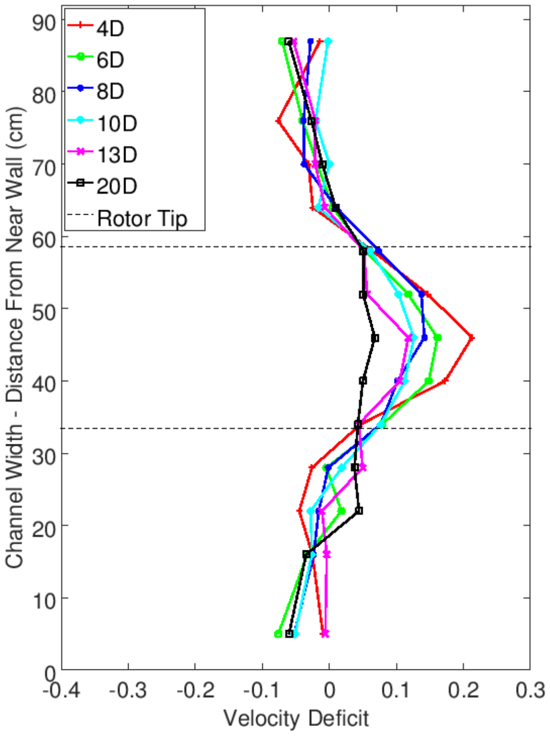

Figure 5.33: Hub Height V_X deficit ($\lambda = 3$)

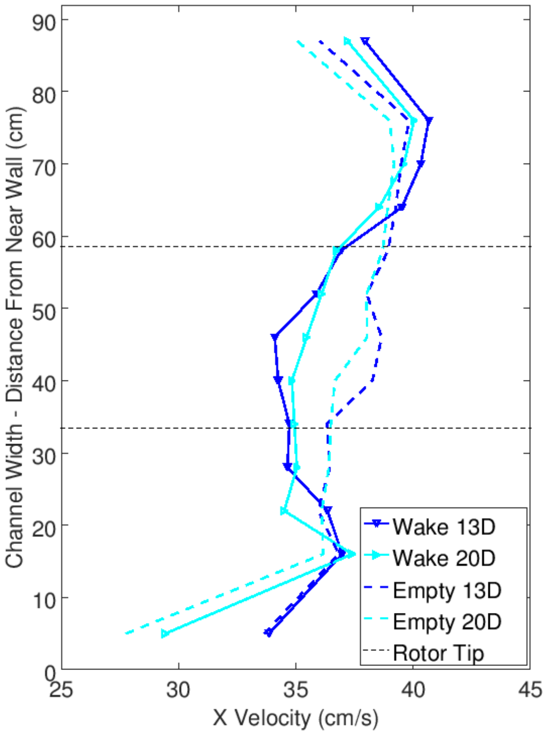

Figure 5.34: Hub Height V_X comparing wake with unimpeded flume ($\lambda = 5$)

deficit increases as the tip speed ratio is reduced. As with Section 5.3.1, there is significant uncertainty within the measurements, and differences between the points are well within the bounds of error.

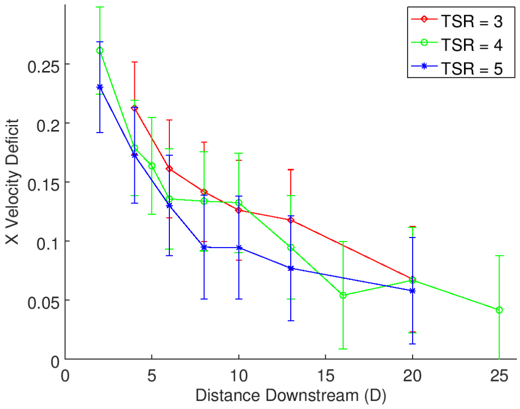

Figure 5.35: Hub Height V_X deficit in the centreline comparing different λ values

5.5 Conclusions

In this chapter an examination of the flow profile of the flume has been given, and the wake profile of a monopile turbine has been presented.

When profiling the flume it was clear that the flow within the channel was non uniform, with the flow being faster towards the far wall. This was thought to be a function of the flume inlet and pump behaviour, and was not rectifiable. Furthermore, there was a rotation within the centre of the lower half of the channel, confirming the swirl imparted by the pump. With respect to height, the flow obeyed approximately a 1/9th power law. A small head increase was found over a 12 m length of the flume, and a corresponding velocity decrease, due to the fluid viscosity. Results were found to be non identical over different measurement sessions. This was dealt with by taking unimpeded flume readings each session to serve as the datum against which the V_X wake measurements would be normalised.

Table 5.4: Deficits and turbulence intensity at selected distances downstream in the centreline and nearside blade tip line

Measurement Location		$\lambda = 3$		$\lambda = 4$		$\lambda = 5$	
		Vel Def	I	Vel Def	I	Vel Def	I
In Centreline	2D	(N/A)	(N/A)	0.26	0.14	0.23	0.11
	4D	0.21	0.10	0.18	0.09	0.17	0.07
	8D	0.14	0.08	0.13	0.07	0.09	0.06
	13D	0.12	0.06	0.09	0.06	0.08	0.06
	20D	0.07	0.05	0.07	0.05	0.06	0.05
At Blade Tip	2D	(N/A)	(N/A)	0.03	0.07	0.01	0.06
	4D	0.05	0.08	0.05	0.08	0.02	0.07
	8D	0.08	0.07	0.06	0.07	0.02	0.06
	13D	0.04	0.07	0.07	0.07	0.03	0.06
	20D	0.04	0.05	0.02	0.05	0.05	0.05

At 2 D downstream the wake of the structure was greatest at the base of the device, as a result of the anchor used. However, this area appeared to have completely recovered by 4 D downstream. The wake of the pile had more longevity, and was visible up to 6 D downstream. There was minimal wake detected behind the nacelle.

The velocity deficit in the wake of the device operating at $\lambda = 4$ reached 0.26 directly behind the device, compared to 0.065 velocity deficit behind the structure alone.

A table of the deficits and turbulence intensity in the wakes of the three configurations tested is shown in Table 5.4. Selected distances downstream are presented to show the near and far wakes. Results are shown for both the centreline and the nearside blade tip line (as per Figure 5.19). Note that no data was recorded at 2 D downstream for the $\lambda = 3$ configuration.

The deficit showed almost continuous recovery in the centreline from 2 – 25 D downstream, with faster recovery near the device, and slower recovery further downstream. This was a strong indication that the wake was still present, albeit greatly reduced, at distances far downstream. This was not visible in the turbulence intensity results, due to the sampling frequency of the measurement device.

It was visible in the velocity data, for all configurations tested, as far as tested (20 to 25 D). This is significant because, were it to be replicated at full scale, it could strongly influence the placement of turbines within arrays. It was observed that the wake due to the rotor recovered more slowly than the wake due to the structure. The largest deficits were found to be in the rotor centreline. Swirl of the rotor was seen in 2 dimensional vector plots at 4 D, but was not seen at 10 D downstream. Velocity deficit has recovered to < 0.1 by 13 D downstream, which is comparable with results found in literature (e.g. Stallard *et al.* (2013) and Chen *et al.* (2017)).

The results in Section 5.4 show the faster rotor speed resulted in a weaker wake. This was most likely due to the use of an inverted propeller as opposed to profiled aerofoil blades. In the following chapter the experimental device was fitted with shaped rotor blades of an S814 profile. However, the results for $\lambda = 5$ and $\lambda = 3$ served as confirmation of the approximate profile of wake recovery, with the wake remaining detectable far downstream.

The results presented contain a significant uncertainty due to the measurement of velocity with turbulent fluctuations and the variation of flume behaviour over different measurement sessions. Chapter 6 reports experiments where each configuration is measured within a single measurement session, reducing the error.

Chapter 6

Wire Hung Results

This chapter displays the results of the second experiment outlined in Chapter 4. Once again the unimpeded flume is presented, and the working section discussed. A base case configuration is then presented, followed by some variations in blade pitch angle and blade number. Finally a contra rotating configuration is presented, also with variations in blade pitch angle.

6.1 Flume Channel Results (No Device)

As the device was free spinning, without brakes or controls applied, the rotational speed was a dependant variable. Table 6.1 shows rotational speed with respect to blade pitch angle. It was expected that the blade rotation would follow a predictable pattern, with an increase in pitch resulting in a decrease in rotational speed.

For most configurations this was the case, but in two instances the rotational speed of the blades remains broadly the same despite an increase in pitch.

- 2 blade rotor from 4° to 6°
- 2 blade rotor on the contra rotating device from 0° to 2°

Table 6.1: Blade rotational speeds for different configurations and pitch angles

	0° Pitch	2° Pitch	4° Pitch	6° Pitch
2 Blade RPM	124	116	56	56
3 Blade RPM	116	72	58	28
Contra-Rotating 2 Blade RPM	100	104	38	56
Contra-Rotating 3 Blade RPM	103	90	84	60

And in one further instance the rotational speed of the blades increases despite an increase in pitch.

- 2 blade rotor on the contra rotating device from 4° to 6°

These all occur with the two blade rotor, two of which occur downstream of the contra rotating device, and two of which occur on the change from 4° to 6°. Reasons for this are unclear.

Whilst there may be small imperfections in the blades and the resistance of the hub may vary in different measurement sessions (as discussed in Section4.7.2), it is reasonable to assume that these changes will be small to negligible. Blades were manufactured to the same standard, and any with visual defects were discarded. Two hubs were used throughout, both manufactured to the same standard and kept in good condition.

Table 6.1 shows that the additional blade in the three blade configuration leads to a reduction in rotational speed, caused by the increased drag of the extra blade. However, this extra blade delivers additional thrust (as can be seen in Table 6.2). It can also be noted that the rotational speeds for the two and three blade rotors in the contra rotating configuration do not always match with the individual rotor speeds.

6.1.1 Flume Consistency Over Area

As has been previously mentioned, there is an asymmetry within the flume, with the near wall flow being roughly 12 % slower than the far wall flow. At 2 D downstream of the proposed rotor position there is a velocity drop of between 6–9 % across the rotor area, which will have some affect on the rotation of the device and the wake produced. With regards to the consistency of the velocity as it travels downstream, the average velocity of all points taken at 2 D downstream was compared with that at 25 D downstream. It was found this varied by less than 0.7 % for three out of four of the cases, with the fourth varying by 3.6% (Session D measurements).

6.1.2 Flume Profiles

Flume profiles are shown in Figures 6.1 to 6.4, over multiple measurement sessions. Differences in measurement sessions has been discussed in Section 4.7.3.

In Figure 6.1 the profiles show a higher velocity at the far wall compared to the near wall, as discussed in Section 5.1.

Y and Z direction velocities were also compared (Figures 6.2a to 6.3d). Across all distances downstream the V_Y was negative, thus there was a flow from the near wall to the far wall. This was to be expected as the V_X difference between the near and far walls would, by extension, be a pressure difference, facilitating cross stream flow. It should be noted that there is no evidence of the cross flow mitigating the V_X difference (i.e. the pressure balancing) with distance downstream. The magnitude of the V_Y was between –1 to –2.5 cm/s, and varied in a manner not proportional to the V_X.

The average V_Z was always small and could be roughly described as $-1.8 < V_Z < 0.6$ cm/s. A negative velocity signifies a flow downwards, towards the bottom of the channel. It can be seen that for all tests at all distances downstream there was consistent variation across the channel. Profiles are dominated by positive V_Z on the near wall side of the channel (roughly $20 - 50$ cm), and negative on the far wall side. This corresponds to the variation in V_X over the same distance.

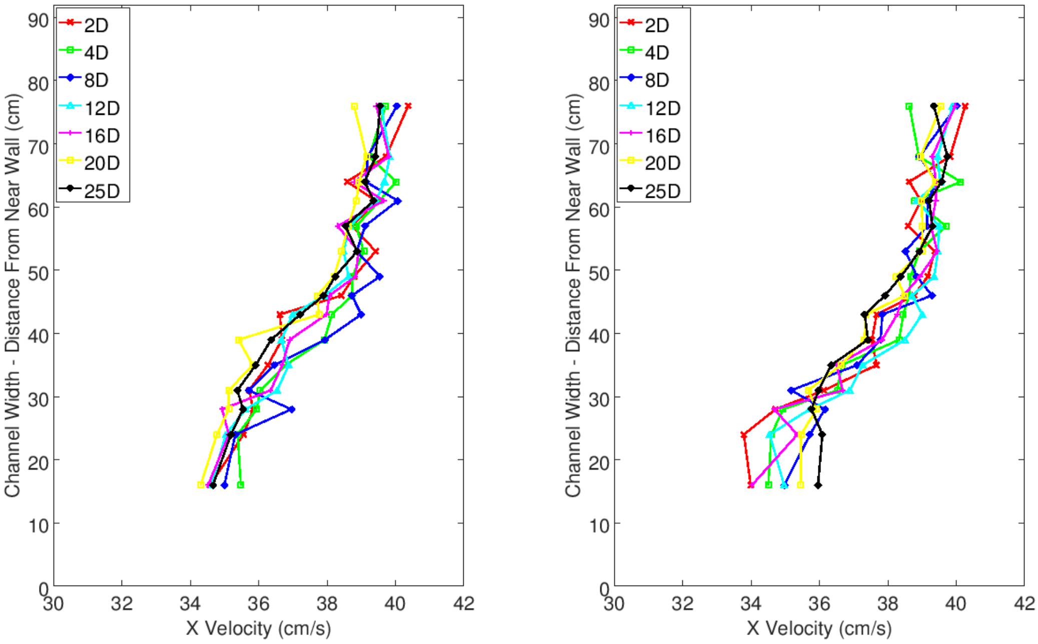

(a) V_X from Measurement Session A

(b) V_X from Measurement Session B

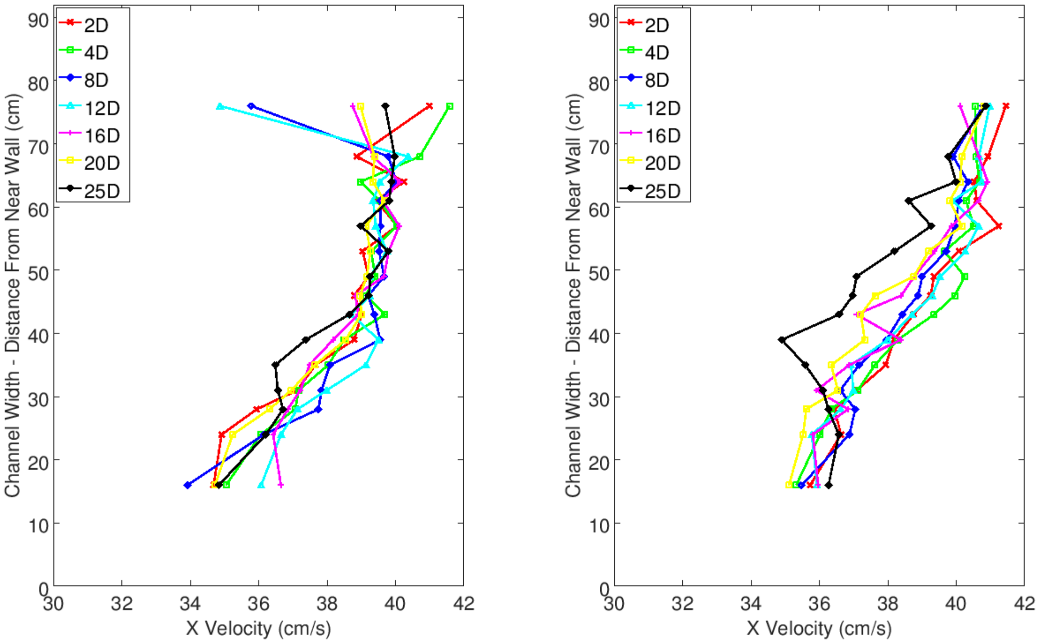

(c) V_X from Measurement Session C

(d) V_X from Measurement Session D

Figure 6.1: Unimpeded flume V_X over different measurement sessions

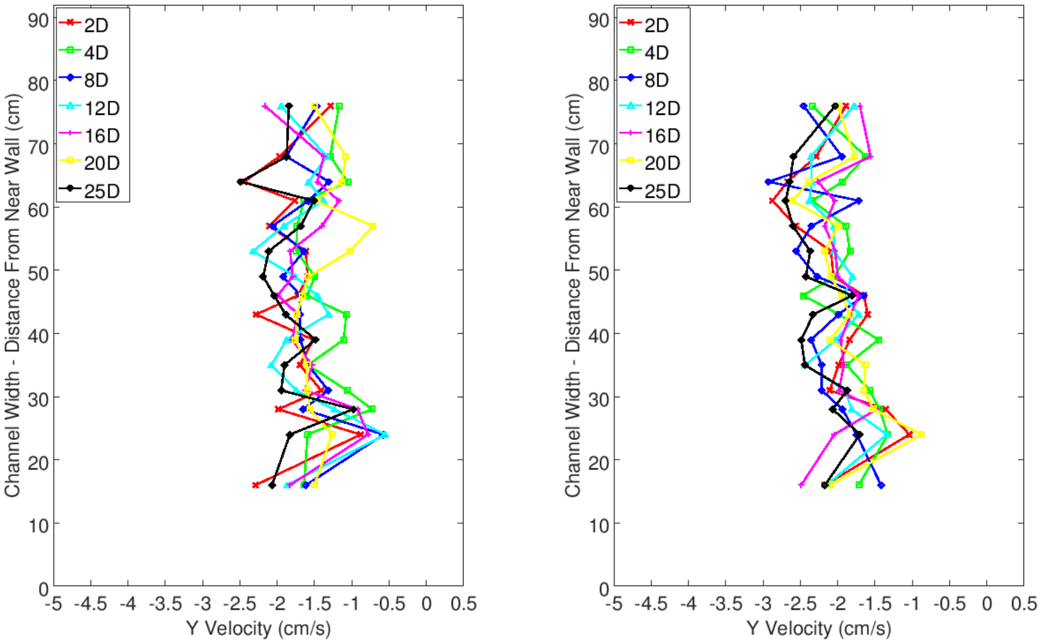

(a) V_Y from Measurement Session A

(b) V_Y from Measurement Session B

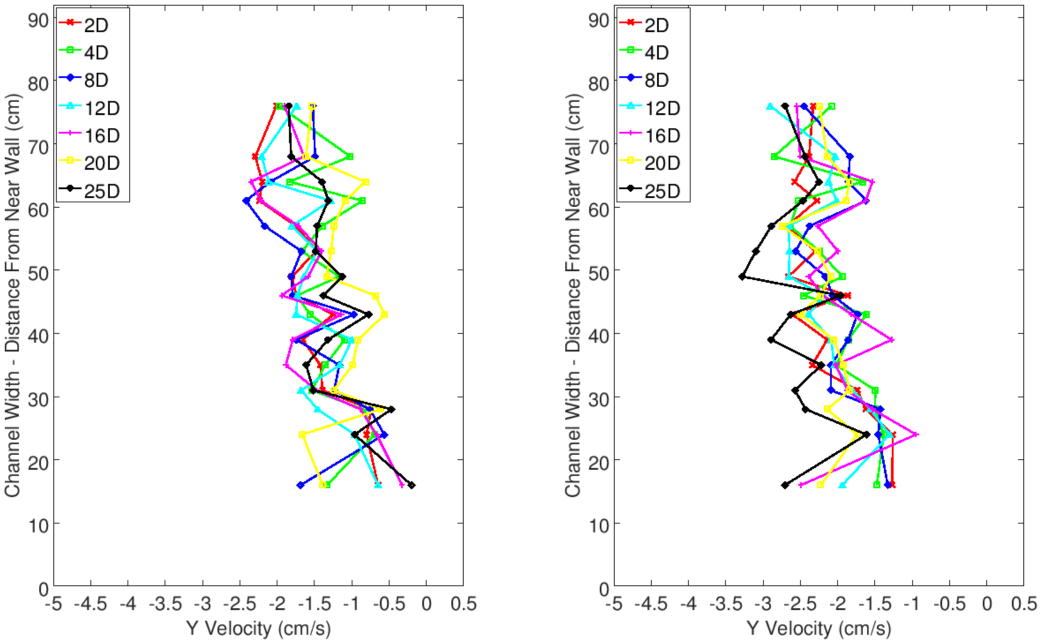

(c) V_Y from Measurement Session C

(d) V_Y from Measurement Session D

Figure 6.2: Unimpeded flume V_Y over different measurement sessions

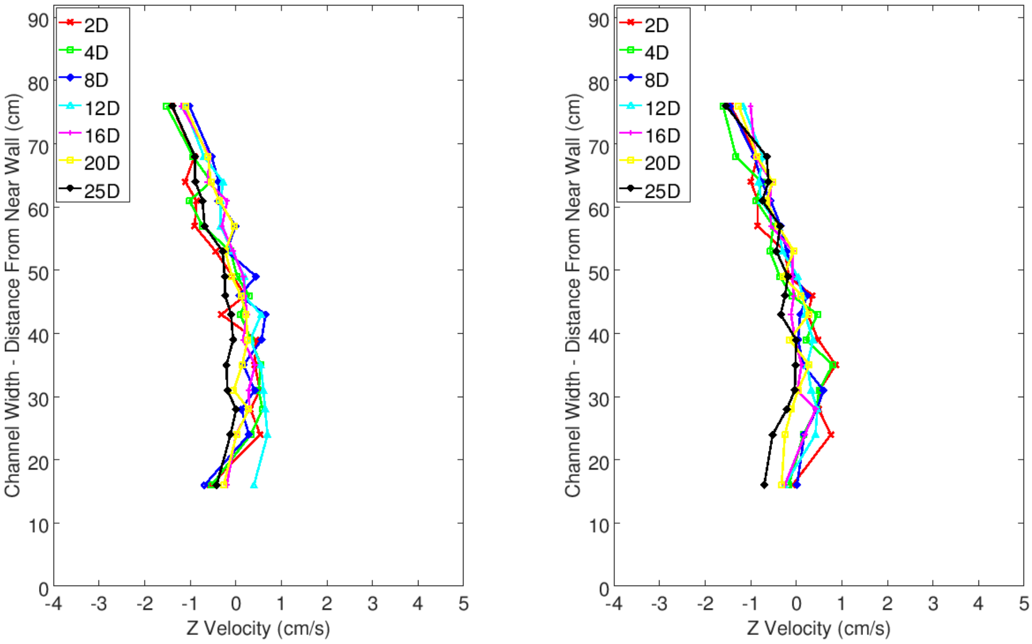

(a) V_Z from Measurement Session A

(b) V_Z from Measurement Session B

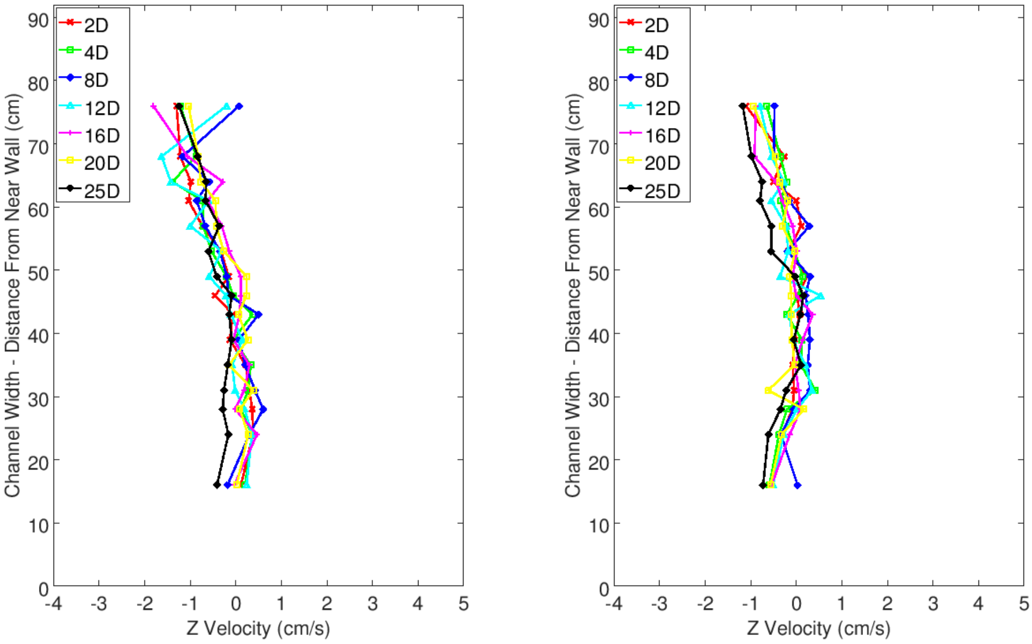

(c) V_Z from Measurement Session C

(d) V_Z from Measurement Session D

Figure 6.3: Unimpeded flume V_Z over different measurement sessions

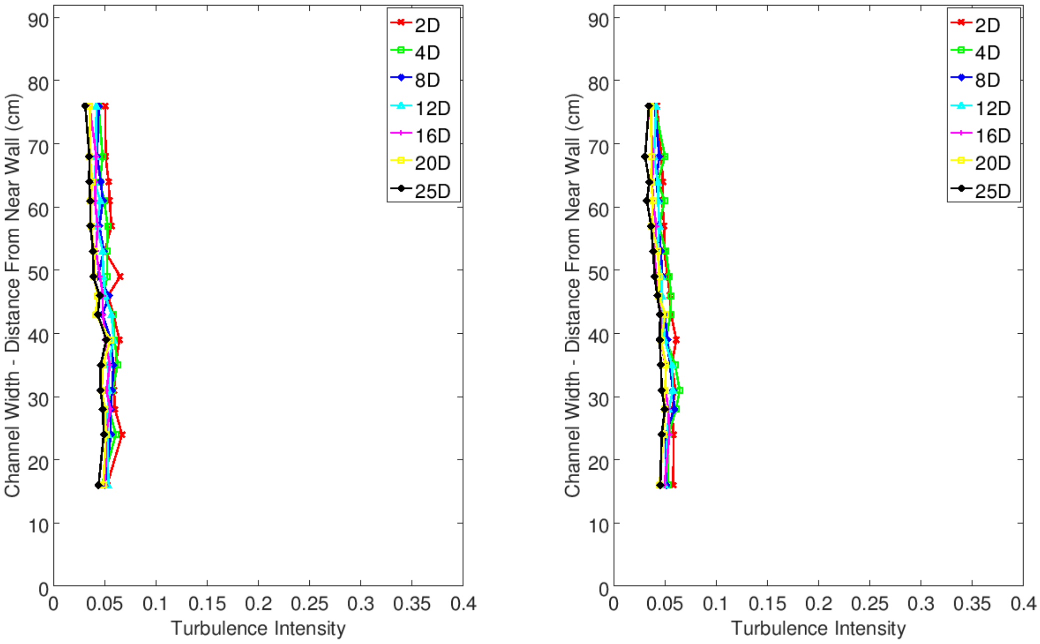

(a) I from Measurement Session A (b) I from Measurement Session B

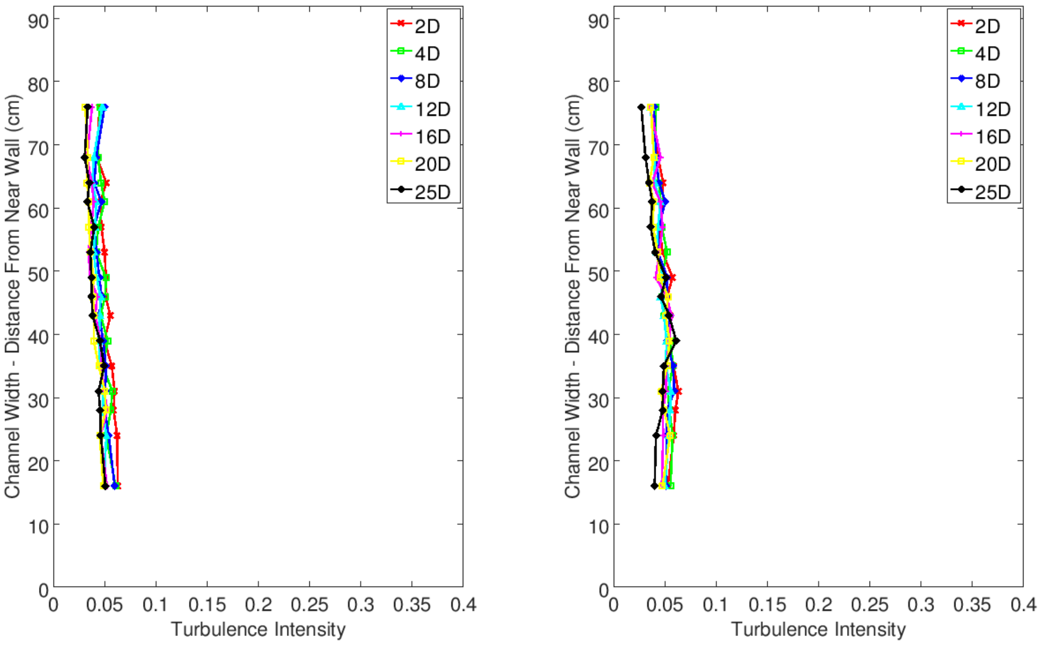

(c) I from Measurement Session C (d) I from Measurement Session D

Figure 6.4: Unimpeded flume I over different measurement sessions

The turbulence intensities are plotted in Figures 6.4a to 6.4d. Turbulence intensity is stated as a decimal, where 1 is equivalent to 100 %. A turbulence intensity of around 5 % can be observed. However, the averaged turbulence intensity across the channel can be seen to be decreasing with distance downstream. Within the working section, over the course of 20 D the turbulence intensity decreases by approximately 1 percentage point. This is likely due to the mesh filter applied far upstream of the working section, which will generate small scale turbulence. It should be noted that the whilst the turbulence drops with distance downstream, V_X does not.

6.1.2.1 Conclusion

The variation within the flume and over different measurement sessions was significant enough to merit close monitoring, and to require detailed unimpeded flume data for each measurement session to act as a datum. As discussed in Section 4.7 the primary method of comparison is made by using wake results normalised against the datum supplied from the relevant measurement session. Measurements not normalised against a datum (Y and Z velocities, and turbulence intensity) must also be compared with the unimpeded flume measurement from the corresponding measurement session. In particular the turbulence intensity must be treated with caution as in the unimpeded flume it decays over distance, due to the upstream mesh filter. Where results are compared across measurement sessions without normalising, this will be noted. There is an opportunity to verify (or otherwise) results produced here using a flume with consistency across its profile and across measurement sessions.

6.1.3 Thrust Coefficient

As mentioned in Chapter 3 the coefficient of thrust, C_T, is a performance defining characteristic which is often used for scaling purposes. C_T can be calculated in

Table 6.2: Coefficients of thrust for different configurations

Configuration	V_W (cm/s)	V_∞ (cm/s)	C_T	Thrust (N)
2 Blade 0°	22.24	38.76	0.67	3.6
2 Blade 2°	21.79	38.76	0.68	3.6
2 Blade 4°	29.44	39.01	0.43	2.3
2 Blade 6°	32.23	38.42	0.30	1.5
3 Bladee 0°	15.47	38.79	0.84	4.5
3 Blade 2°	19.65	38.79	0.74	4.0
3 Blade 4°	25.19	38.79	0.58	3.1
3 Blade 6°	27.23	36.98	0.46	2.2
2 and 3 Blade Contra 0°	10.47	39.25	0.93	5.1
2 and 3 Blade Contra 2°	7.27	38.92	0.97	5.2
2 and 3 Blade Contra 4°	13.60	38.92	0.88	4.7
2 and 3 Blade Contra 6°	27.31	37.73	0.48	2.4

multiple ways, depending on available data. C_T was approximated using the measured velocity data. Equations 2.13 and 2.10 were used to calculate C_T and the thrust loadings. The wake velocity was taken to be the velocity at 2 D downstream of the device in the axial line of the rotor; the upstream velocity was closely approximated by taking the velocity at the same point in the unimpeded flume. Thus the values were calculated and are shown in Table 6.2.

It should be noted that the thrust measurements presented here are likely to be an underestimation; as they are taken from velocity readings 2 D downstream of the device there is likely to be some wake recovery within that distance which is not accounted for here. However, thrust values here do provide an accurate reflection of the relative difference beween configurations, and thus provide a basis for comparison.

From here it can be seen that the thrust levels experienced by the device ranged from 1.5 N for two blades at 6° pitch, to 5.2 N for contra rotating at 2° pitch. The thrust was greater for higher than for lower numbers of blades (two blades $<$ three blades $<$ contra rotating blades). The thrust decreased as the pitch was increased, with two exceptions (two blade 0 to 2° pitch and contra rotating 0 to 2° pitch). The C_T ranged from 0.30 to 0.97. As previously mentioned, Ainslie (1988) ascertained that an increased C_T results in an increased wake deficit. However, given that in this case the velocity measurements were used to calculated the C_T, any application of this principle is tautological, and amounts to nothing more than stating that a larger velocity deficit immediately behind the device will lead to a larger velocity deficit further downstream, all other things being equal.

6.1.4 Power Generation

It is apparent here that an increase in blade number results in an increase in thrust loading, which would signify an increase in power capture. Operational devices are faced with the engineering trade off between extra energy generation and cost of blade manufacture. In this experimental work the thrust generated by the contra rotating blade configuration was greater than that of the three blade configuration, which in turn was greater than the two blade configuration. However, the thrust generated by the contra rotating configuration was considerably less than the sum of the two component configurations, as shown in Table 6.2, indicating that the two sets of rotors in the contra rotating configuration have some influence over each other.

6.1.5 Tip Speed Ratio

The tip speed ratios for each configuration are shown in Table 4.2 and are repeated here in Table 6.3.

6.1.6 Points of Note

- The rotational speed of the devices decreased as pitch increased (with some exceptions, see Table 6.1).
- The flume velocity variation upstream / downstream was acceptable (Sec-

Table 6.3: λ for different configurations

Configuration	Pitch Angle	λ
2 Blade	0°	5
2 Blade	2°	4.7
2 Blade	4°	2.3
2 Blade	6°	2.3
3 Blade	0°	4.7
3 Blade	2°	2.9
3 Blade	4°	2.3
3 Blade	6°	1.2
Contra 2 Blade	0°	4
Contra 2 Blade	2°	4.2
Contra 2 Blade	4°	1.5
Contra 2 Blade	6°	2.3
Contra 3 Blade	0°	4.1
Contra 3 Blade	2°	3.6
Contra 3 Blade	4°	3.4
Contra 3 Blade	6°	2.5

tion 6.1.1).

- The flume velocity variation across different measurement sessions was acceptable, with measurement sessions gaving close results. Velocity deficit normalisation would allow for comparison across all sessions (Section 6.1.2).

- The turbulence intensity decreased with distance downstream in the unimpeded flume (Figures 6.4a to 6.4d).

- The thrust generated by the contra rotating device was significantly less than the sum of the thrusts of the two single rotor configurations (Table 6.2).

6.2 Base Case Discussion (2 Blades)

6.2.1 V_X Profile

The first set of experiments to be discussed is the 2 blade configuration. Velocity deficit is stated as a decimal, where 1 is equivalent to 100 %. The velocity deficits at 0° pitch are shown in Figure 6.5a. A large and rapid recovery can be seen from 2 D to 8 D, where the deficit drops from 0.46 to 0.17. This is followed by a much slower recovery beyond 8 D. From Figure 6.5a it appears that the wake has returned to freestream velocity by 25 D downstream at 0° pitch, and perhaps upstream of here (however turbulence measurements suggest that this may not be the case). By 16 D downstream there is no point with a deficit exceeding 0.1, although the wake continues to recover beyond this distance. On either side of the device an acceleration in the flow is observed (shown as negative deficit), as some fluid is forced around the device. These accelerations peak at around a 0.1 increase in flow velocity, and decrease with distance downstream. However, this negative deficit remains for a significant portion of the downstream measurement area; well into the far wake at 12 D downstream. The change in deficit outwith the rotor area is small, though it is clear that the velocity is tending to freestream. Any wake expansion occurring does not appear to be significant enough to be registered within the measurement grid.

6.2.2 Peak Velocity Comparisons

For each configuration and at each distance downstream the highest velocity deficit was taken. These peaks mainly occurred in the centre of the rotor area, but not exclusively; due to wake movement the peak was sometimes found one measurement point away from the centre. These peaks (Figure 6.6) give a further picture of the wake recovery. As is shown, the 0° and 2° pitch configurations have very similar wake recoveries, within the error bounds for all distances downstream.

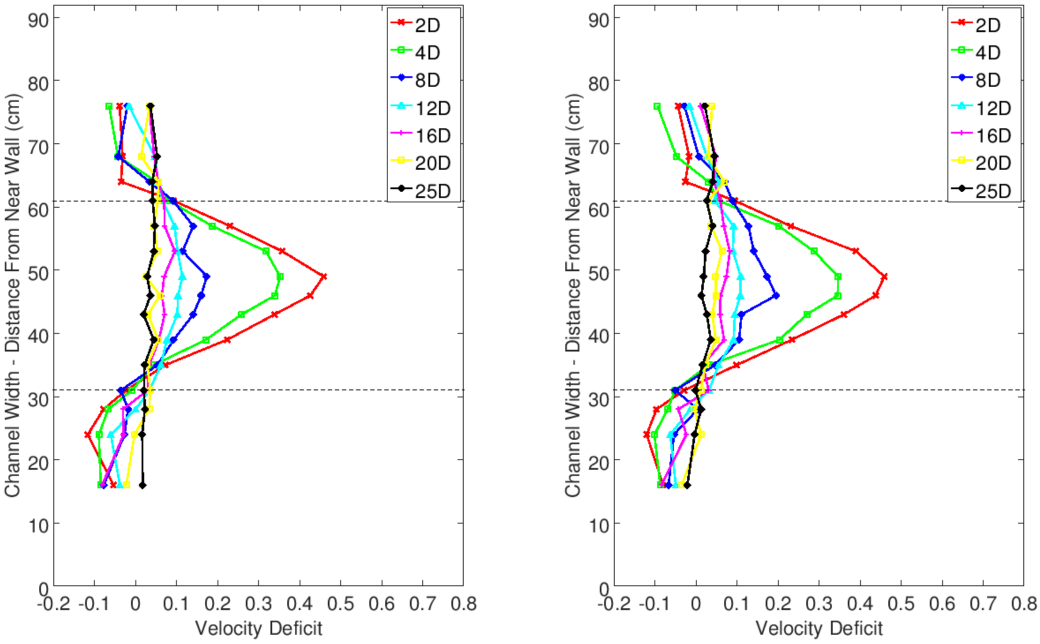

(a) V_X for the Base Case of 2 Blades at 0° pitch ($\lambda = 5$)

(b) V_X for the Case of 2 Blades at 2° pitch ($\lambda = 4.7$)

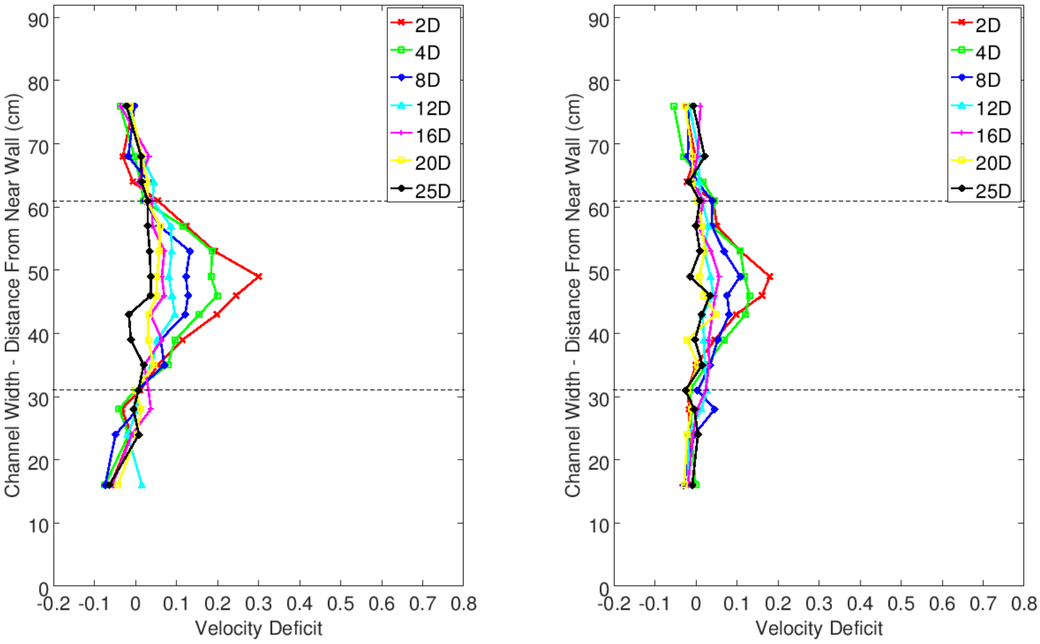

(c) V_X for the Case of 2 Blades at 4° pitch ($\lambda = 2.3$)

(d) V_X for the Case of 2 Blades at 6° pitch ($\lambda = 2.3$)

Figure 6.5: V_X for the Case of 2 Blades at different pitches

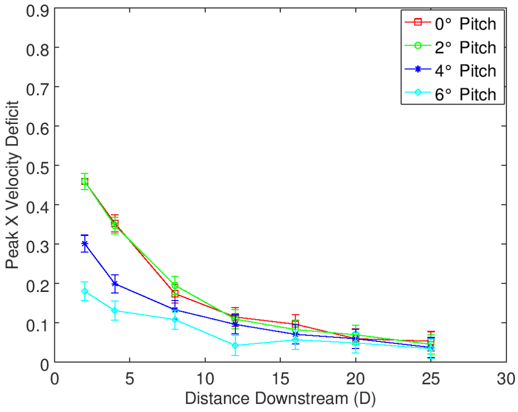

Figure 6.6: Peaks of V_X for all 2 Blade Cases

If recovery is arbitrarily defined as the wake deficit not exceeding 0.1 at any measurement point, then the wake reaches this condition somewhere between 12 to 16 D for 0° and 2° pitch, and between 8 to 12 D for 4° and 6° pitch. Recovery does continue beyond this, but the gradient at which it occurs is shallow. The velocity will never fully return to free stream as energy has been extracted from the flow. Uncertainty bars are calculated for each point individually and show the effect of the turbulent velocity fluctuations. Uncertainty is less for the wire hung measurements than for the pile mounted measurements as for the former each configuration is measured within a single measurement session.

Figures 6.5b, 6.5c and 6.5d show the velocity deficit for 2°, 4° and 6° pitch. Unsurprisingly, an increase in pitch (leading to a decrease in λ) generally results in a smaller wake impact. However, it can be seen that the peak deficit for the 2° pitch configuration marginally exceeds that of the 0° pitch configuration, and at all distances downstream the wake recovery is similar for 0° and 2° pitch. This indicates that at 0° pitch the rotor is slightly over-speeding, and the maximum coefficient of performance (C_P) will be found somewhere between 0° and 2° pitch. For the lower values of λ the peak velocity deficit behind the rotor is reduced, and less downstream distance is required for the deficit to fall beneath 0.1. Furthermore, the velocity increase on either side of the rotor is also reduced, and is not detected at all at 6° pitch.

6.2.3 Turbulence Profile

Turbulence intensity is a measure of the fluctuations about the mean of a flow, and is often used as a measure of turbulent activity. Figure 6.7a plots the turbulence profiles for the two blade configurations (results are taken over different measurement sessions). Unlike the velocity deficit, these data are not normalised, so flume characteristics are still present. At 2 D downstream of the device at 0° pitch the turbulence peaks at 13.8 % before seemingly dropping to ambient levels of ≈ 4–5 % further downstream. Here the wake recovers faster towards the near wall, which could be an indication of wake drift towards the far wall.

Comparing Figures 6.5a and 6.7a, it would appear that the turbulence has returned to ambient conditions before the velocity deficit has. However it may be that some remnant can be observed, as the average of the turbulence across the flume was taken at 25 D downstream, and was found to be higher than the corresponding value for the unimpeded flume. This difference was repeatedly found for other configurations at this distance downstream. However, the difference was small (4.6 % versus 4.1 %), and within the margin for error due to sampling. Further experimental work, using a higher sample size, could confirm or refute this effect.

The turbulence intensity should be used cautiously as an indicator of wake recovery in this experimental process. As mentioned previously, turbulence decays when large low frequency eddies pass energy into smaller, higher frequency eddies, which in turn pass on energy to eddies smaller still. The ability to detect these eddies is dependent on the sampling frequency of the data capture device. In this case, the Nortek Acoustic Doppler Velocimeter sampled at 25 Hz, giving a Nyquist frequency of 12.5 Hz (Luke, 1999). Any energy contained in eddies broken down into frequencies higher than this was not detected, making it likely that certain

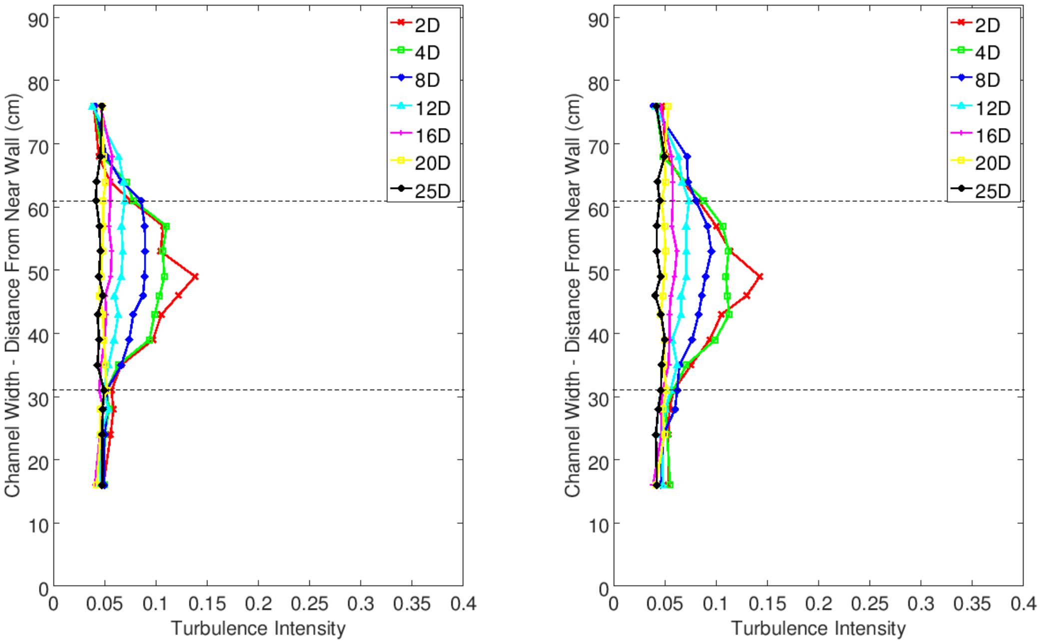

(a) I for the Base Case of 2 Blades at 0° pitch ($\lambda = 5$)

(b) I for the Case of 2 Blades at 2° pitch ($\lambda = 4.7$)

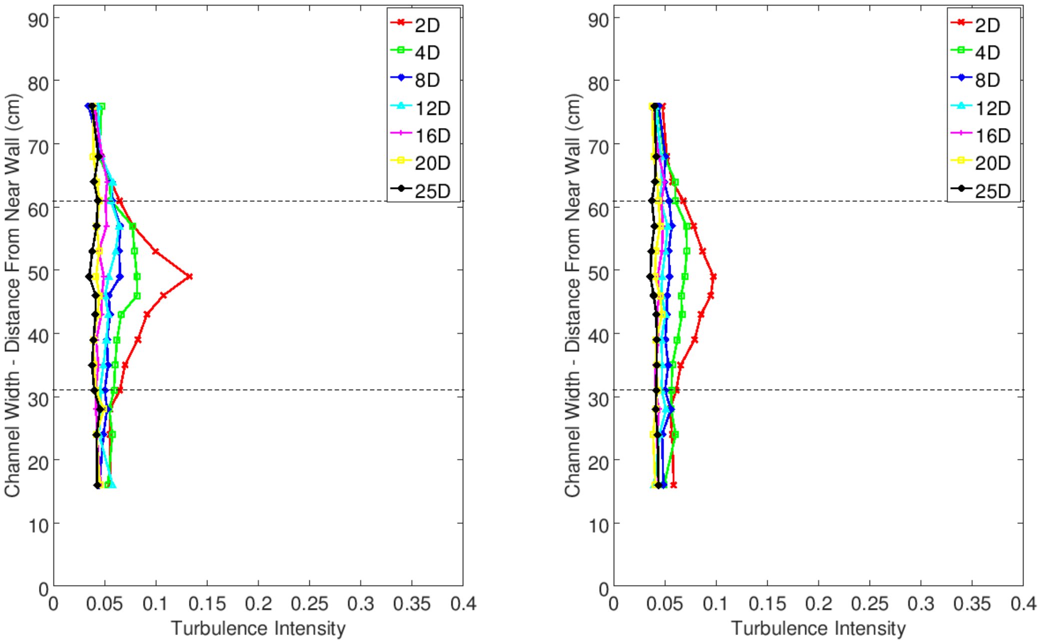

(c) I for the Case of 2 Blades at 4° pitch ($\lambda = 2.3$)

(d) I for the Case of 2 Blades at 6° pitch ($\lambda = 2.3$)

Figure 6.7: I for the Case of 2 Blades at different pitches

aspects of the turbulence within the wake are not shown. A further point to note is that the areas on either side of the device show no sign of increased or decreased turbulence, despite the velocity increase noted above. From Equation 5.2, for a flow where the mean velocity is increased, and the turbulence intensity remains constant, the RMS velocity fluctuations must also increase proportionally.

Like the velocity deficit, the 2° pitch configuration has a peak turbulence value marginally greater than that of 0° pitch, whilst the 4° and 6° pitch configuration peaks decrease (Figures 6.7b to 6.7d, results taken over different measurement sessions). As with the base case, ambient turbulence of $\approx$ 4–5 % appears to be reached at 16 D downstream for the 2° and 4° pitch configurations, and 8 D for the 6° pitch configuration. However, for the 2° pitch configuration the average turbulence across the flume at 25 D downstream exceeds the same average in the unimpeded flume. This may demonstrate the persistance of the wake effect, however, it is within the margin of error due to sample size. As mentioned in Section 4.4.5 the turbulence measured is dependent on the measurement equipment sampling frequency.

6.2.4 V_Y and V_Z Profile

Profiles were also plotted for Y and Z direction velocities, in Figures 6.8 and 6.10 respectively (results are taken over different measurement sessions). These profiles are less informative than the X directional profiles, but are useful nonetheless. There is little distinguishable coherent shape in the V_Y profiles (Figure 6.8a) at any distance downstream. Measurements were taken along the channel horizontally at hub height, where the blades rotatation resulted in very little horizontal flow displacement. Figure 6.9a shows a slight imprint of the wake at 2 D downstream, where the V_Y magnitude has increased over the rotor area, this is also visible at 4 D downstream. In both the unimpeded flume case and the base case, V_Y is always negative, and remains consistent across the channel.

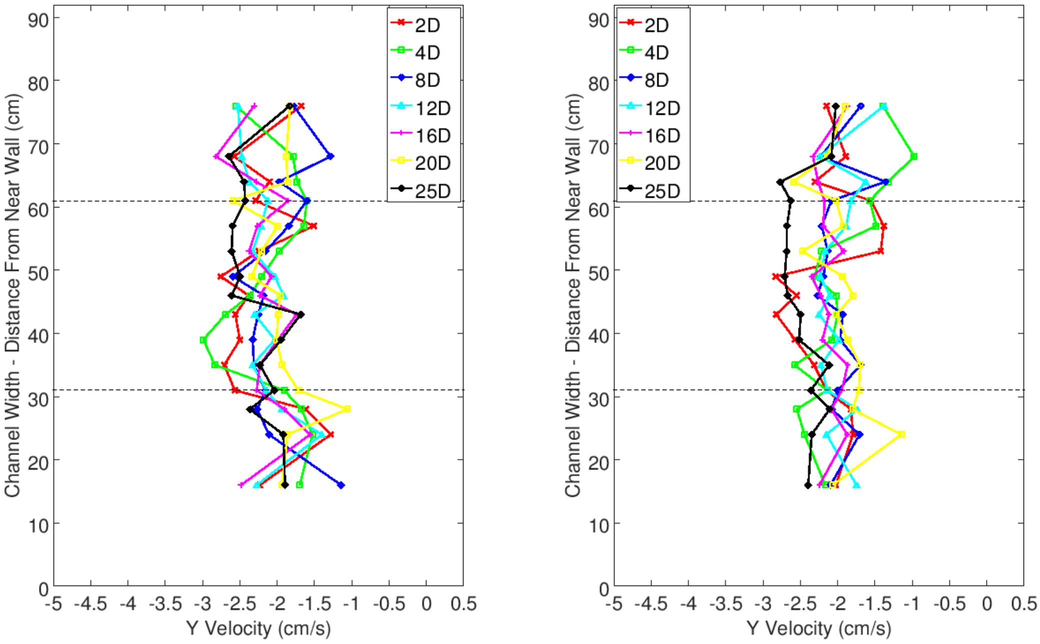

(a) V_Y for the Base Case of 2 Blades at 0° pitch ($\lambda = 5$)

(b) V_Y for the Case of 2 Blades at 2° pitch ($\lambda = 4.7$)

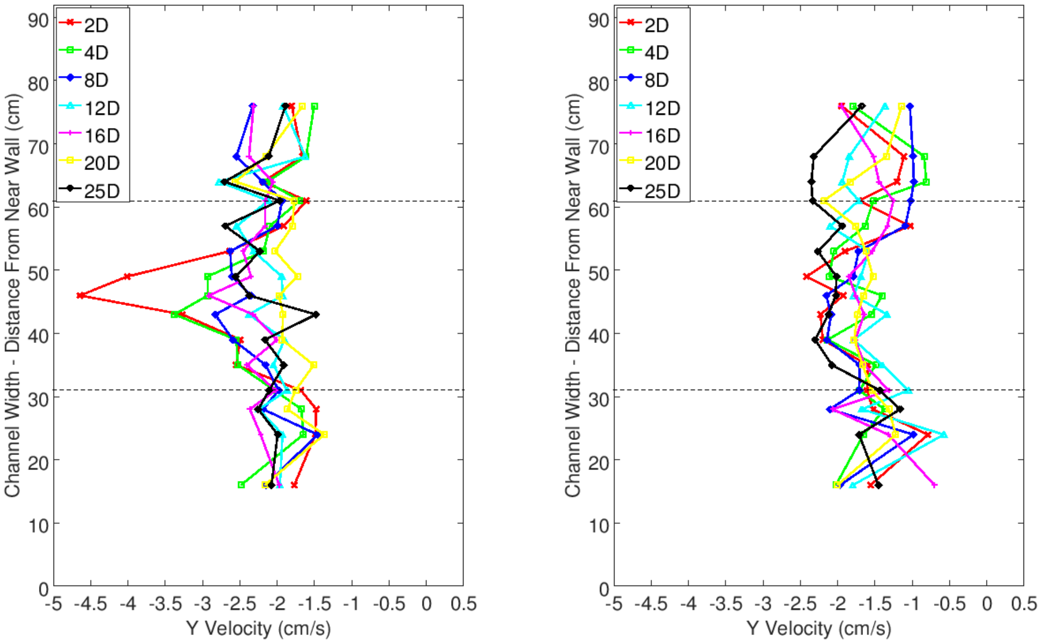

(c) V_Y for the Case of 2 Blades at 4° pitch ($\lambda = 2.3$)

(d) V_Y for the Case of 2 Blades at 6° pitch ($\lambda = 2.3$)

Figure 6.8: V_Y for the Case of 2 Blades

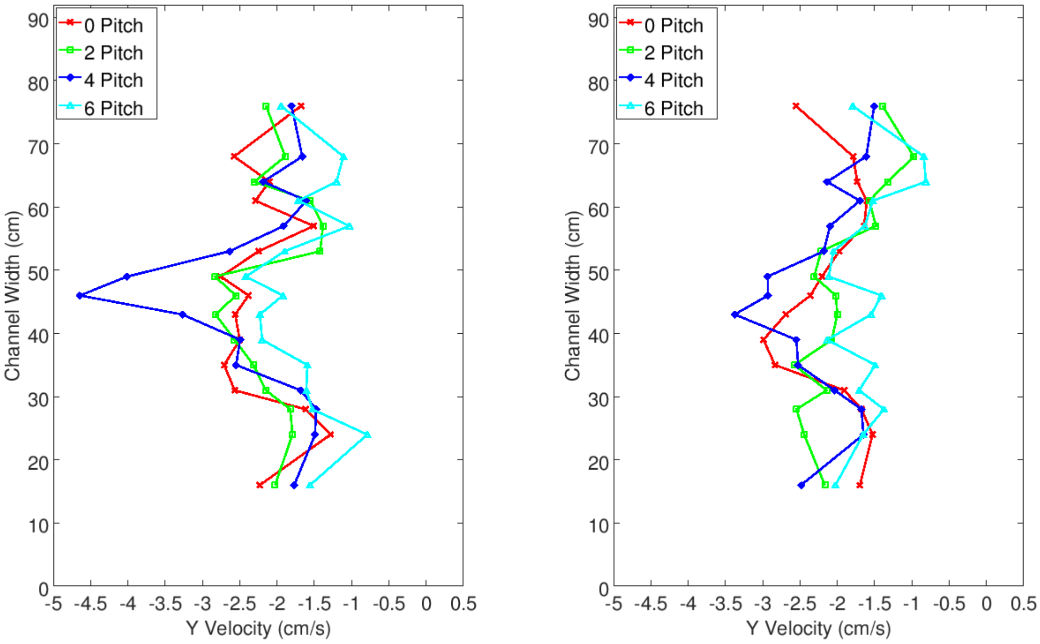

(a) V_Y for all 2 blade configurations at 2 D downstream

(b) V_Y for all 2 blade configurations at 4 D downstream

Figure 6.9: V_Y for 2 blade cases in the near wake

At distances further downstream, coherent patterns within the V_Y profiles remain elusive, but an imprint of the wake can be seen in the near wake when compared with the empty flume (Figures 6.8b to 6.8d compared with 6.3) (results are taken over different measurement sessions). This is shown more clearly in Figure 6.9. The velocity range also remains consistent throughout the different configurations. It will be noticed that a velocity spike is apparent at 2 D downstream of the device in the 4° pitch configuration. As this spike incorporates three separate measurement points it is unlikely to be caused by instrument error, and likely to be a physical flow feature. Given that it is not replicated in any other pitch setting (or blade configuration) it will be treated as an anomaly. It may have been caused by some form of detritus in the flume attaching itself to the turbine, however this is speculative and the origin of the anomaly is unknown.

The profiles in the Z direction (Figure 6.10a), however, provide evidence of rotation within the near wake. An inverted 'S' shape can be seen in the profiles closest to the device. This demonstrates the direction of rotation, as the helical structure of the near wake is formed. The flow acts on the blades, which impart an equal and opposite force on the flow, causing it to rotate. As the measurements were taken horizontally across the centre of the rotor the flow is forced upwards on one side and downwards on the other, as displayed. The velocities displayed are average values, whilst the helix of the near wake is dependent on the rotation of the blades.

If a single point immediately behind a rotor is considered, it will 'see' the wake of this rotor as each blade passes by (if pressure effects are ignored). The V_Z at that point will not be continuously affected by the wake, but will return to something like freestream conditions after the blade has passed by. A time average of this will give a low result for the V_Z, as it is tempered by the time where the blade is not passing. If this point is then moved further downstream there will be a time offset between the blade passing the point and the wake reaching the point, but the measurement will still see the wake of the blade at the same angle of rotation (in this case horizontal). As this is only visible at 2, 4 and faintly at 8 D downstream, it is reasonable to assume it is a feature of the near wake, and beyond this the wake structure is broken down and becomes non directional. An actuator disc does not impart rotation to the wake, and these results go some way to justifying the use of an actuator disc as a substitute for a rotational device when considering the far wake, assuming the near wake breakdown does not significantly alter the far wake. However, these results suggest that the rotational part of the wake (i.e. the near wake) may extend for further than is often suggested, as there is still evidence of rotation at 8 D downstream.

The size of this 'S' shaped signal could be increased if the measurement frequency was synchronised with the blade rotation (as in Ebert and Wood (1997), Ebert and Wood (1999) and Ebert and Wood (2001)), eliminating the freestream periods from the average results. This might also have the effect of increasing

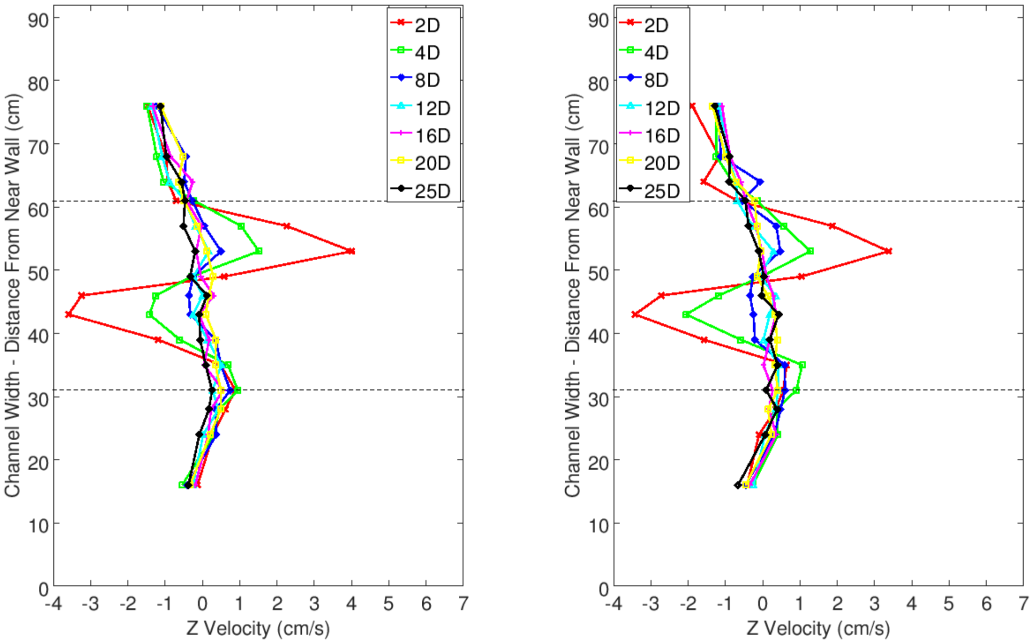

(a) V_Z for the Base Case of 2 Blades at 0° pitch ($\lambda = 5$)

(b) V_Z for the Case of 2 Blades at 2° pitch ($\lambda = 4.7$)

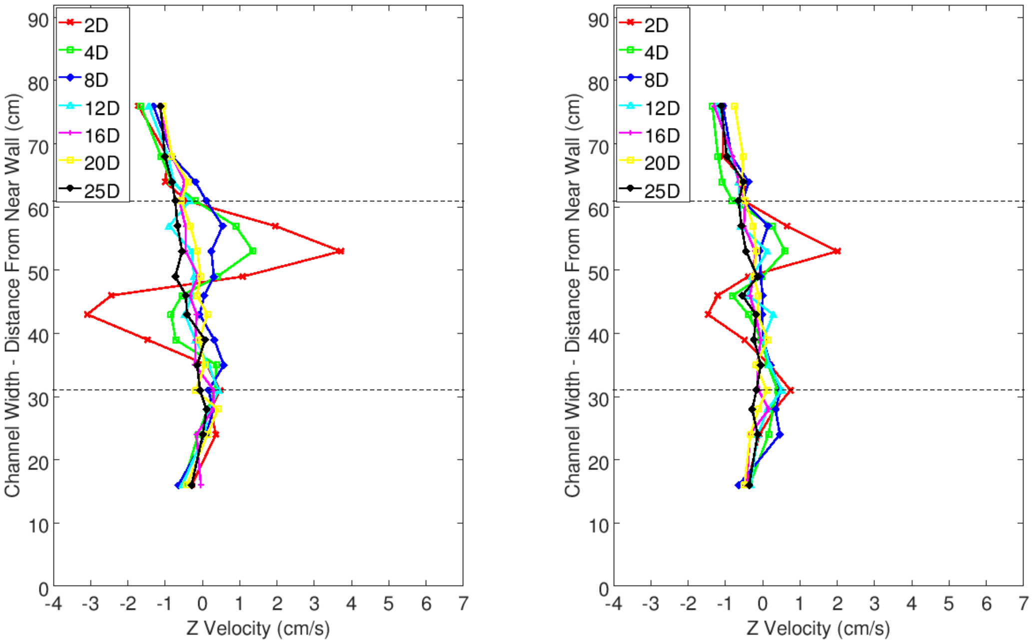

(c) V_Z for the Case of 2 Blades at 4° pitch ($\lambda = 2.3$)

(d) V_Z for the Case of 2 Blades at 6° pitch ($\lambda = 2.3$)

Figure 6.10: V_Z for the Case of 2 Blades

the distance downstream at which the rotational effect can be seen, and further increase the length of the observed near wake.

The 'S' shaped impact of the rotor in the near wake seen in Figure 6.10a is also seen in Figures 6.10b to 6.10d. As would be expected, the larger λ configurations show a more significant effect. In Figure 6.10b there is some slight remnant of this signal at 8 D downstream, but it has mostly faded by this point. Downstream of this the V_Z profiles are near indistinguishable from the unimpeded flume profiles. This highlights the fact that the main velocity component of the wake is a deficit in the X direction. However, given that these measurements are time averaged, it may be that instantaneous measurements time synchronised with the blade rotation would reveal V_Z structure further downstream.

An increase in the region of swirl expected (i.e. the near wake) has the potential to increase environmental concerns, as it may increase seabed scouring, bathymetry changes or other ecological changes at a given location.

6.2.5 Points of Note

- The base case maximum velocity deficit measured was 0.46, occuring 2 D downstream of the device (Figure 6.5a).
- The wake recovers to less than 0.1 deficit by 16 D downstream (Figure 6.5a).
- Maximum C_P will likely be found somewhere between 0° and 2° pitch, that is $\lambda = 5$ and $\lambda = 4.7$ (Section 6.2.2).
- The lower tip speed ratios (i.e. $\lambda = 2.3$) have wakes that are smaller immediately behind the rotor, and recover to 0.1 more quickly. There is also less wake acceleration around the rotor (Figure 6.5).
- For 0° and 2° pitch the wake deficit reaches 0.1 between 12-16 D (Figures 6.5a and 6.5b).

- For 4° and 6° pitch the wake deficit reaches 0.1 between 8-12 D (Figures 6.5c and 6.5d).

- There is further recovery beyond this, but it is gradual.

- Averaged turbulence measurements may give some indication of a continued wake at 25 D downstream, however this is small and not confirmed by turbulence profiles (Section 6.2.3).

- Ambient turbulence appears to be reached by 16 D downstream for the 2° pitch, but further examination shows it has not returned to freestream conditions Figure 6.7b).

- The average turbulence across the flume at 25 D is greater behind the rotor than in the unimpeded flume – thus there is evidence of the wake at 25 D downstream (Section 6.2.3).

- Fluid is accelerated by up to 10 %, around the device (Section 6.2.1).

- No wake expansion is observed (Section 6.2.1).

- A small imprint of the wake is noted in the V_Y profile near wake (Figure 6.8).

- An ‘S’ shape is visible in the V_Z profile graphs, which demonstrates the rotation of the near wake (Figure 6.10).

- This ‘S’ shape would be much bigger and might extend further downstream if measurements were time sychronised with the blade passing (Section 6.2.4).

- That the ‘S’ shape is not visible beyond 8 D indicates that actuator discs are an acceptable approximation for the far wake (Section 6.2.4).

- However, the near wake may extend up to 8 D downstream, further than suggested in some literature (Section 6.2.4).

- The ‘S’ shapes are also related to λ – a higher λ gives a more significant ‘S’ shape (Figure 6.10).

- The main impact of the rotor on the velocity of the flow is a deficit in V_X, which is more significant than any impact in V_Y or V_Z (Section 6.2.4).

6.3 Extra Blade Comparison – 3 Blades

The addition of an extra blade does not necessarily facilitate direct comparison with the previous configuration. The additional blade will increase both lift and drag of the rotor, altering the thrust coefficient. The altered rotational speeds can be seen in Table 6.3, and the altered thrust coefficients in Table 6.2. Nevertheless the comparison of the wake of a two and three blade device is of interest. Furthermore it will allow discussion on the assumption of superimposition of wakes when examining the contra rotating configuration.

6.3.1 V_X Profiles

The velocity deficit profiles of the 3 blade configuration are shown in Figures 6.11a to 6.11d. They broadly conform to a similar pattern of recovery as those looked at previously: a large recovery between 2–8 D followed by a more gentle recovery, flow acceleration on either side of the device, and no sign of wake expansion. However, some clear differences can be highlighted. The magnitude of the deficit is greater in the three blade configuration for all pitches, peaking at 0.6 for 0° pitch. The wake deficit still exceeds 0.1 at 20 D downstream for 0° pitch, and is discernible for 2° pitch as well. The deficit of the 0° pitch is greater than that of the 2° pitch. Finally, certain low deficit outliers are obvious at points closest to both the near and far walls, and are particularly evident close to the near wall during the 4° pitch configuration. The two points closest to the far wall at 0°, 2° and 4° pitch for 8 and 12 D downstream are also irregular, and should be compared to the corresponding unimpeded flume graph (Figure 6.1), which shows similar outliers in the datum tests, indicating the far wall V_X deficit outliers are a result of the data against which they were normalised.

6.3.2 Peak Velocity Comparisons

Again the peak velocity deficits at each distance downstream were plotted against each other (Figure 6.12). As mentioned, the three blade configurations have a larger wake velocity deficit than the two blade configurations for all pitches. From 16 – 25 D downstream there is very little change in the peak velocity deficits of the 0° pitch configuration; it remains around 0.1. This may indicate that the flow behind the rotor is fully mixed, and the deficit will decrease by only negligible amounts from here on. However, this would suggest that the device had removed approximately 19 % of the kinetic energy in the flume, through energy capture and turbulence generation.

Whilst the device may have caused an energy reduction of this magnitude, a further possibility is that the flume was not fully mixed, and the 0.1 deficit was specific to the rotor area. This is borne out in Figure 6.11a, where even at 25 D downstream a peak exists in the rotor area. At this point mixing was occurring very slowly, with a reduction in peaks of 0.005 between 20 – 25 D downstream. It is reasonable to assume that beyond this the mixing of the full flume cross section would continue to occur very slowly, resulting in evidence of the wake far beyond 25 D downstream.

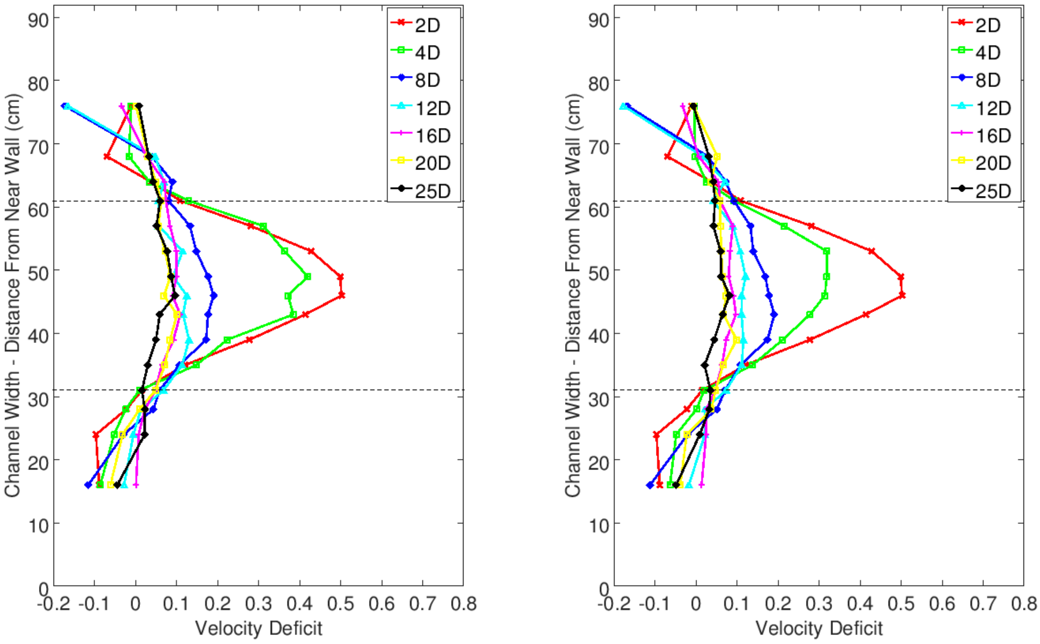

(a) V_X for the Case of 3 Blades at 0° pitch ($\lambda = 4.7$)

(b) V_X for the Case of 3 Blades at 2° pitch ($\lambda = 2.9$)

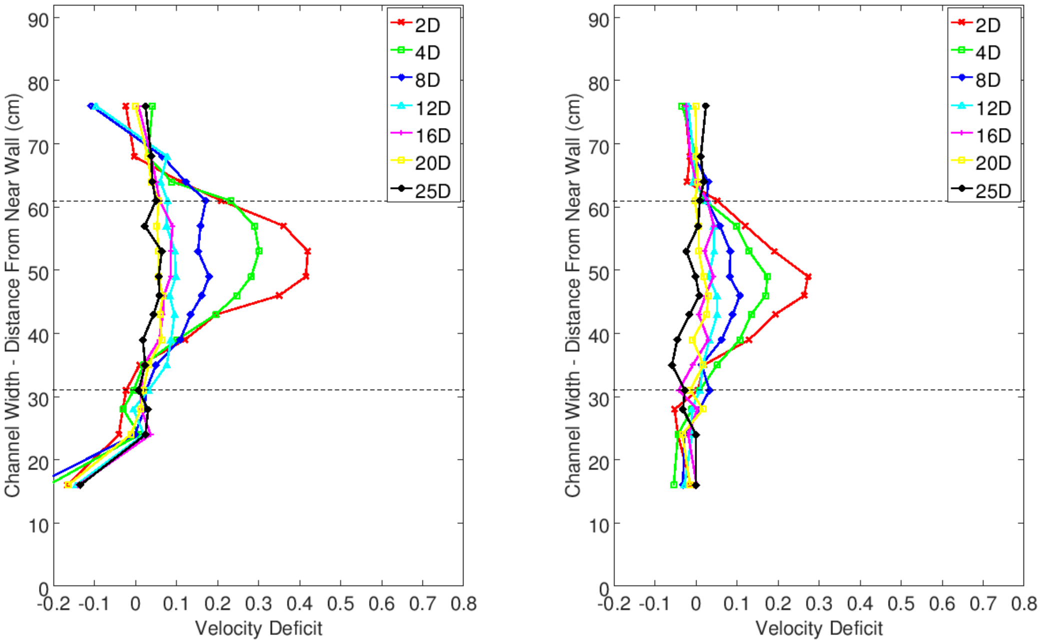

(c) V_X for the Case of 3 Blades at 4° pitch ($\lambda = 2.3$)

(d) V_X for the Case of 3 Blades at 6° pitch ($\lambda = 1.2$)

Figure 6.11: V_X for the Case of 3 Blades at different pitches

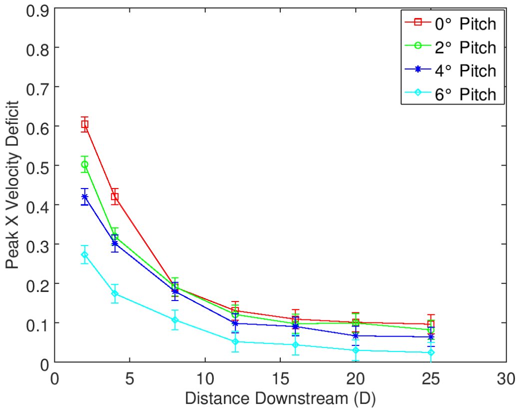

Figure 6.12: Peaks of V_X for all 3 Blade Cases

6.3.3 Turbulence Profile

In the three blade configuration the turbulence in the wake was found to be greater than for the two blade configuration (Figures 6.13a to 6.13d, results taken over different measurement sessions), peaking at 23 % for 0° pitch. At 2° and 4° pitch the peak turbulence was greater for three blades (5 % and 3 % greater respectively). However, at 6° pitch the peak turbulence is only half a percentage point greater for three blades than two.

By 16 D the 0° pitch turbulence has dissipated enough to avoid detection at 25 Hz sampling, and between 16 – 20 D the standard deviation across the channel was very similar to that of the unimpeded flume. However, the average turbulence across the flume at 25 D was higher for the three blade configuration than the unimpeded flume or the two blade configuration. The average turbulence at 25 D downstream was also higher than the unimpeded flume for 2° pitch, and surprisingly, for 4° pitch. This suggests that even at 25 D downstream, for a 4° pitch configuration, an imprint of the wake is still present in the flume, changing the characteristics of the flow. The average turbulence at 25 D downstream was higher for 0° pitch than for 2° pitch, and for 2° pitch than for 4° pitch.

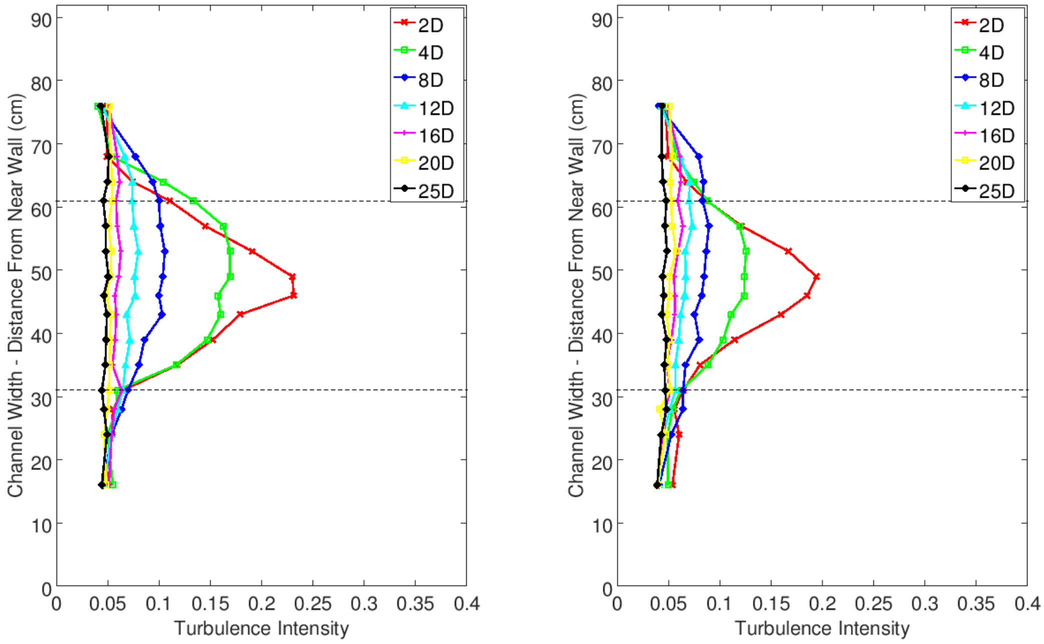

(a) I for the Case of 3 Blades at 0° pitch ($\lambda = 4.7$)

(b) I for the Case of 3 Blades at 2° pitch ($\lambda = 2.9$)

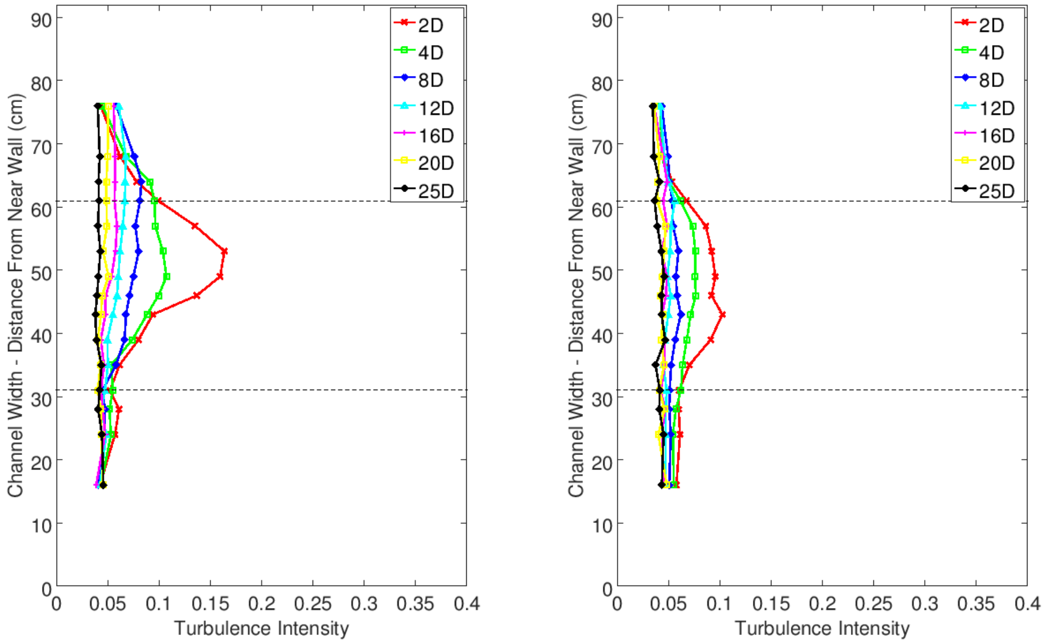

(c) I for the Case of 3 Blades at 4° pitch ($\lambda = 2.3$)

(d) I for the Case of 3 Blades at 6° pitch ($\lambda = 1.2$)

Figure 6.13: I for the Case of 3 Blades at different pitches

6.3.4 V_Y and V_Z Profiles

As with the two bladed configurations, no pattern is discernible in the V_Y profiles (shown in Figures 6.14a to 6.14d, results taken over different measurement sessions). A range of 2 – 3 cm/s is in the same order as the previous configurations, but the velocities are approximately 0.5 cm/s higher (i.e. closer to 0 cm/s), which is within the bounds of variation within the flume setup. This is comparable to the corresponding unimpeded flume tests which show the same range around the same velocity, although the unimpeded flume profiles show an increase in V_Y magnitude close to the far wall, which has been negated by the presence of the device. At 2 D downstream for 0°, 2° and 4° pitch, V_Y increases at the rotor area, a change not seen in the two blade configurations.

In the Z direction the profiles in Figures 6.15a to 6.15d show the impact of the blades on the near wake. These 'S' shapes are in the reverse direction to those of the two blade configurations, as the blades rotated in the opposite direction. At 0° and 2° pitch the strong Z directional spikes seen at 2 D downstream are small by 4 D downstream and not visible at 8 D downstream.

6.3.5 Points of Note

- The wake profiles of the three blade device are similar to the two blade device, but the wake magnitude is greater for three blade (Section 6.3.1).
- The peak deficit is 0.6, immediately downstream of the 0° pitch device (Figure 6.11a).
- There is little recovery between 16–25 D downstream of the 0° pitch configuration; it remains around 0.1 (Figure 6.11a).
- The wake is not fully mixed at 25 D downstream, as there is still a peak deficit for the wake (Section 6.3.3).

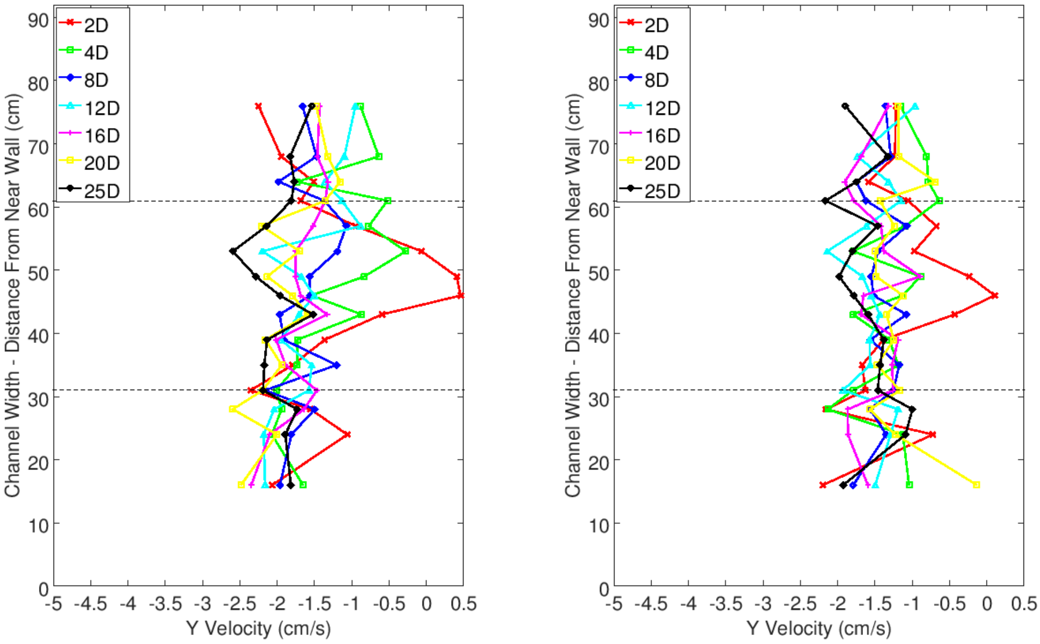

(a) V_Y for the Case of 3 Blades at 0° pitch ($\lambda = 4.7$)

(b) V_Y for the Case of 3 Blades at 2° pitch ($\lambda = 2.9$)

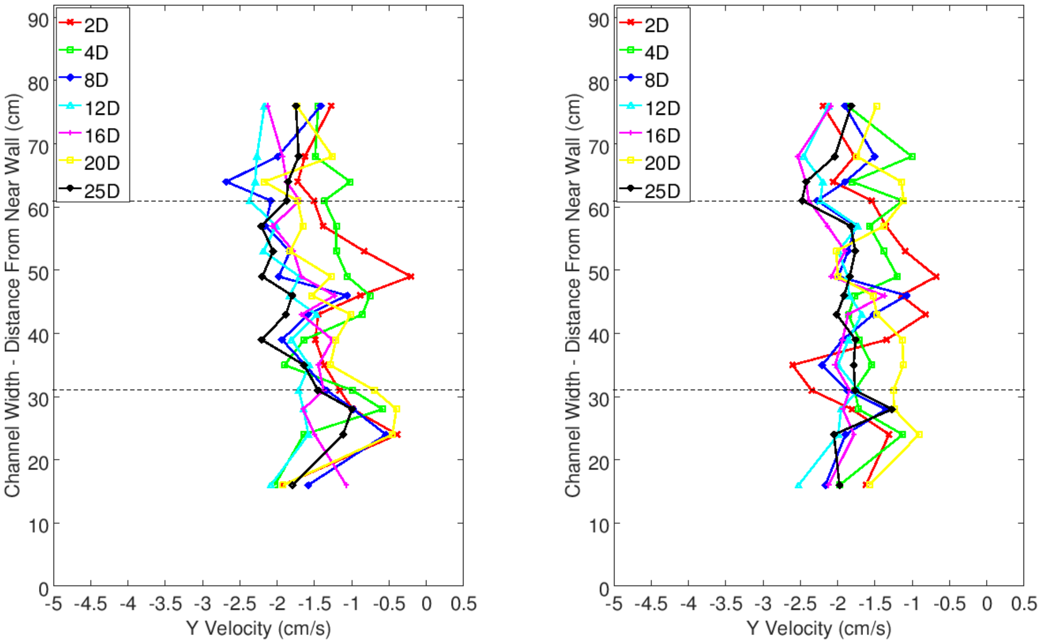

(c) V_Y for the Case of 3 Blades at 4° pitch ($\lambda = 2.3$)

(d) V_Y for the Case of 3 Blades at 6° pitch ($\lambda = 1.2$)

Figure 6.14: V_Y for the Case of 3 Blades at different pitches

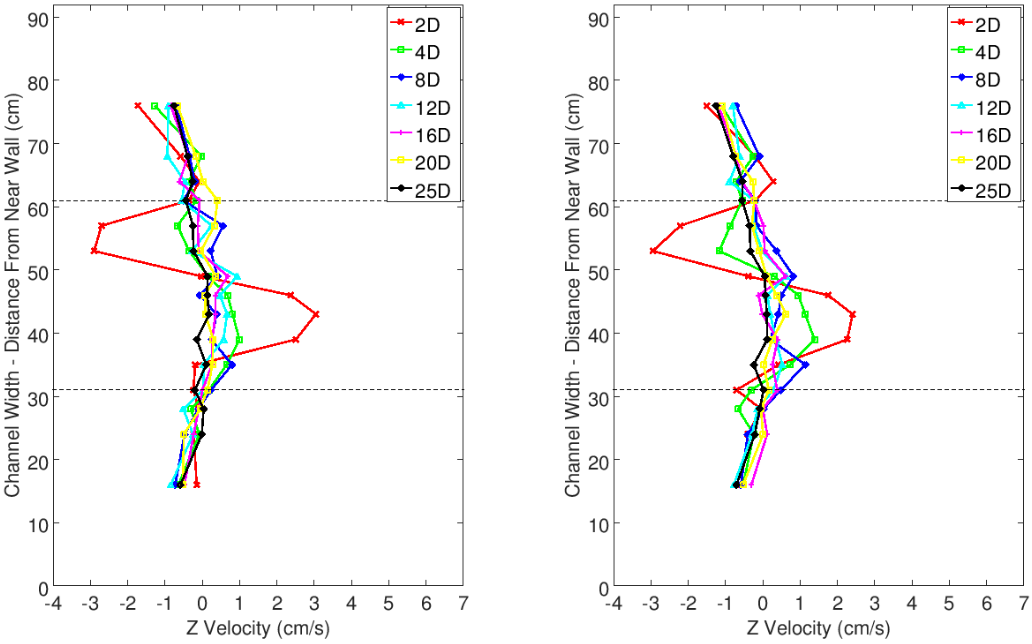

(a) V_Z for the Case of 3 Blades at 0° pitch ($\lambda = 4.7$)

(b) V_Z for the Case of 3 Blades at 2° pitch ($\lambda = 2.9$)

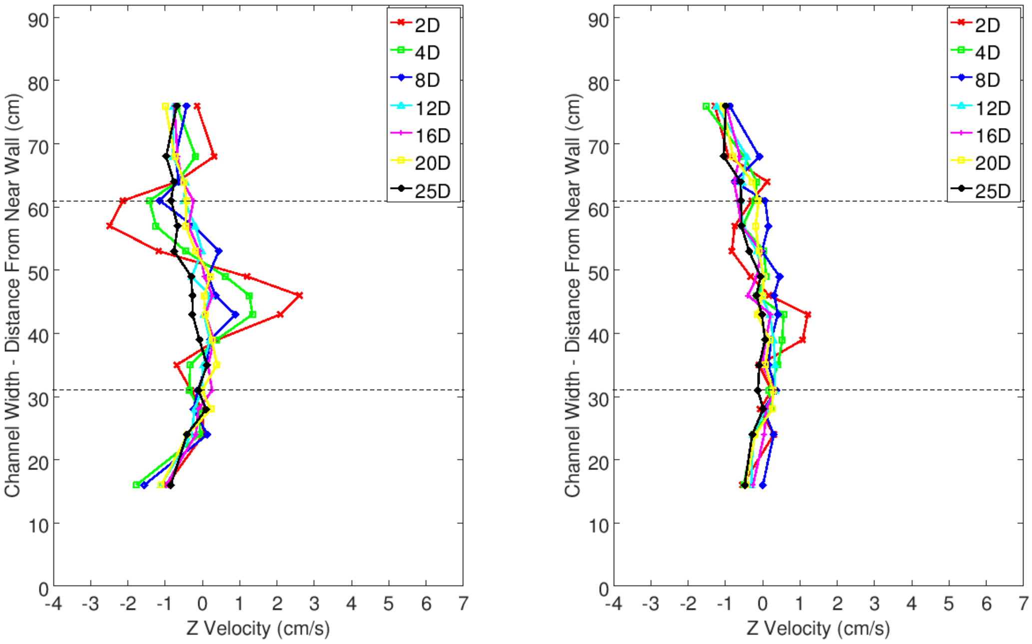

(c) V_Z for the Case of 3 Blades at 4° pitch ($\lambda = 2.3$)

(d) V_Z for the Case of 3 Blades at 6° pitch ($\lambda = 1.2$)

Figure 6.15: V_Z for the Case of 3 Blades at different pitches

- It can be assumed that mixing will be slow further downstream, and there will still be evidence of the wake beyond 25 D (Section 6.3.2).
- Turbulence for the three blade device was greater than for the two blade (Figures 6.13a and 6.7a).
- Although there is no visible wake in the turbulence profile, the average turbulence across the channel at 25 D is greater for 0° pitch than 2° pitch, and 2° pitch than 4° pitch, and 4° pitch than the unimpeded flume. Thus there is still device generated turbulence at 25 D downstream (Section 6.3.3).
- An increase in V_Y is noted immediately downstream of the device, a change not seen in the 2 blade configuration (Section 6.3.4).
- Rotation in the wake is noted at 8 D downstream for the 4° pitch case (though not for the 0° pitch or 2° pitch cases, see Section 6.3.4).

6.4 Contra Rotating Comparison

An ideal contra rotating device will produce a wake with no rotational component in the velocity (Hansen, 2008). Furthermore, the energy generated will be more than that of a single rotor device, there will be no requirement for a rigid support structure due to torque balance, and the design may not require a gear box. However, it is unclear whether the wake of a contra rotating tidal device will extend further downstream than the wake of a single rotor device, and to what extent the deficit is increased.

6.4.1 V_X Profiles

Velocity deficits for the contra rotating configurations are shown in Figures 6.16a to 6.16d. The wake deficit magnitude is higher than that of the other two configurations, with a peak deficit of 0.75 at 0° pitch. However, in all pitch settings the wake appears to have dissipated or be very small by 25 D. This is in contrast to the 3 blade configuration results. As with the two blade configuration, the 2° pitch configuration has a higher deficit than the 0° configuration.

6.4.2 Peak Velocity Comparisons

Peak deficits are shown in Figure 6.17. Of all tests conducted the contra rotating configurations produce the largest velocity deficits, reaching 0.81. At 8 D downstream there is very little difference between the three lower pitch settings, which remain close further downstream. Though initially very high the deficits reduce quickly and by 25 D are small. At 0° and 2° pitch the deficit recovers to 0.1 between 16 – 20 D downstream, whilst for 4° pitch this occurs between 20 – 25 D. Unlike the three blade configurations, meaningful deficit reduction occurs below a deficit of 0.1 for all pitch settings. This high rate of recovery far downstream suggests that there is more mixing within the flume, and it is significant that this may have been facilitated by the contra rotation of the rotors. The increased mixing may be due to the lack of coherent structure in the near wake, the helical vortex sheets which form behind each blade are forced to interact in a contra rotating device, whereas they are left to break down naturally behind a single rotor. This is corroborated in Figures 6.16a to 6.16d, where no peak is noticeable in the rotor area for the profiles far downstream, but rather each profile shows a reasonably straight line across the flume, indicating the deficit is roughly uniform.

In Figure 6.18 the peak V_X is shown for the contra rotating, 2 blade and 3 blade configurations at 2° pitch. Although the initial wake deficit is significantly higher for the contra rotating device than the three blade device, by 25 D downstream the contra rotating wake deficit is lower than that of the 3 blade configuration, though higher than that of the 2 blade configuration. The higher coefficient of thrust and initial velocity deficit do not result in a higher velocity deficit downstream.

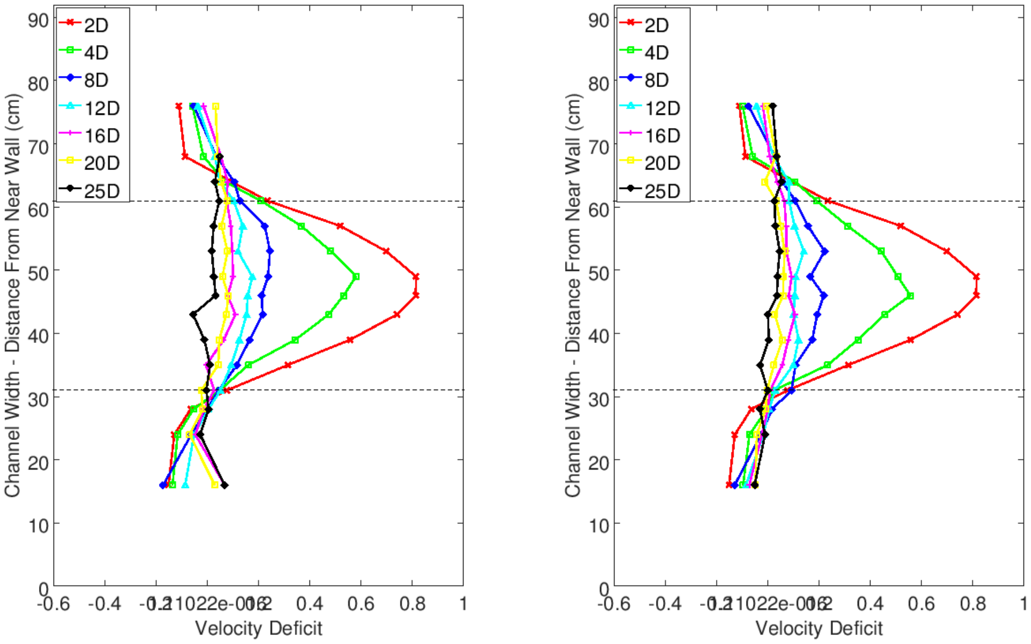

(a) V_X for the Contra Rotating Case at 0° pitch

(b) V_X for the Contra Rotating Case at 2° pitch

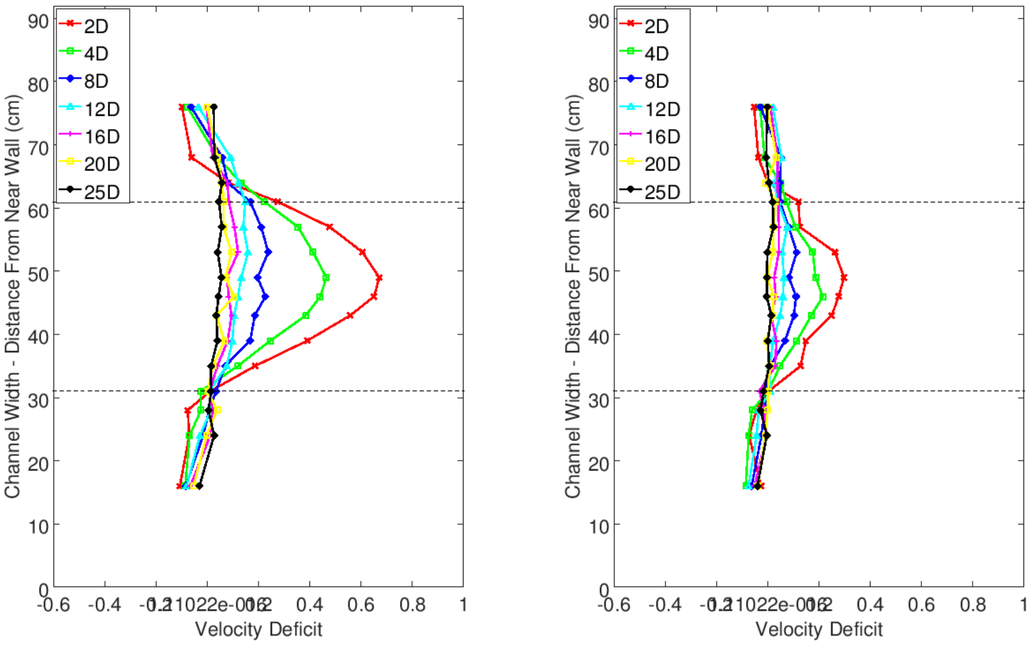

(c) V_X for the Contra Rotating Case at 4° pitch

(d) V_X for the Contra Rotating Case at 6° pitch

Figure 6.16: V_X for the Contra Rotating Case at different pitches

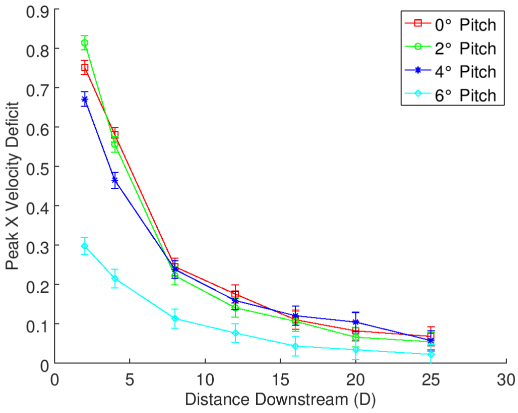

Figure 6.17: Peaks of V_X deficit for all Contra Rotating Cases

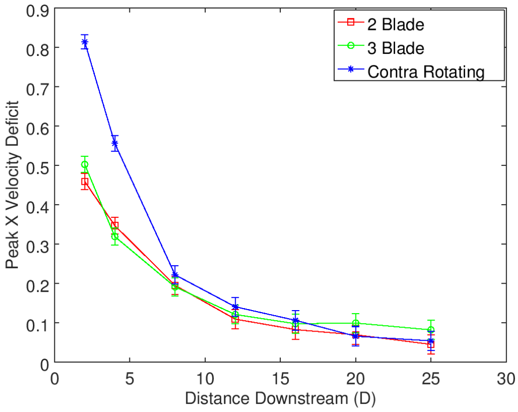

Figure 6.18: Peaks of V_X deficit for all Configurations at 2° pitch

6.4.3 Turbulence Profile

The turbulence from the contra rotating configuration shows a peak deficit of 34 % for 2° pitch at 2 D downstream (Figures 6.19a to 6.19d, results taken over different measurement sessions). Whilst this is greater than that of 0° pitch, interestingly the turbulence at 4 D downstream is only very slightly larger for 2° pitch, and by 8 D downstream the peak turbulence for 0° pitch is greater. For all configurations the wake appears to be small by 16 D downstream, and the turbulence is well mixed across the channel width. As with the previous configurations, the average turbulence taken across the flume at 25 D downstream is greater than the corresponding average from the unimpeded flume, which indicates the persisting effects of a wake.

When the peak turbulence intensities for the contra rotating, three blade and two blade configurations are plotted with respect to distance downstream, it becomes clear that the contra rotating configuration produces a more turbulent wake that the others (Figure 6.20). This increased turbulence is seen up to 25 D downstream. In the near wake the difference between the contra rotating device and the other configurations is large, but the recovery is also large and by 8 D downstream the turbulence intensities are similar for all configurations. This vastly increased turbulence found immediately downstream of the contra rotating device results in only a small increase in turbulence beyond the near wake.

6.4.4 V_Y and V_Z Profiles

As with previous configurations, the V_Y profiles display incoherence, within a consistent range (Figures 6.21a to 6.21d).

Perhaps the most significant result from the contra rotating configuration can be seen in Figures 6.22a to 6.22d, where the V_Z profiles are shown (results are compared across measurement sessions). Here the 'S' shaped spikes caused by the blade rotation (as seen in the two and three blade configurations) are not so

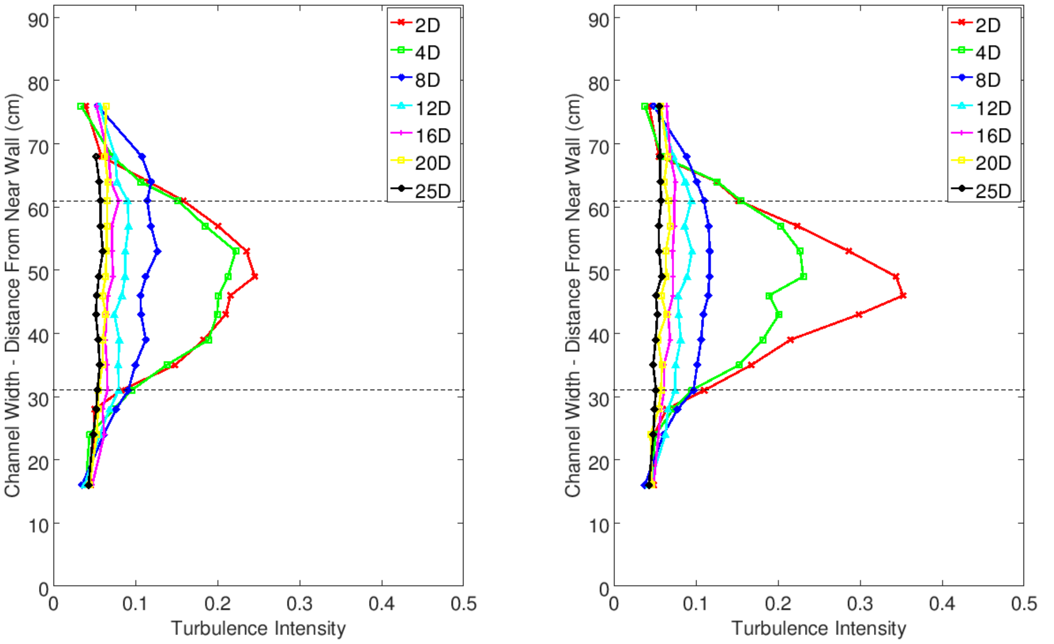

(a) I for the Contra Rotating Case at 0° pitch (b) I for the Contra Rotating Case at 2° pitch

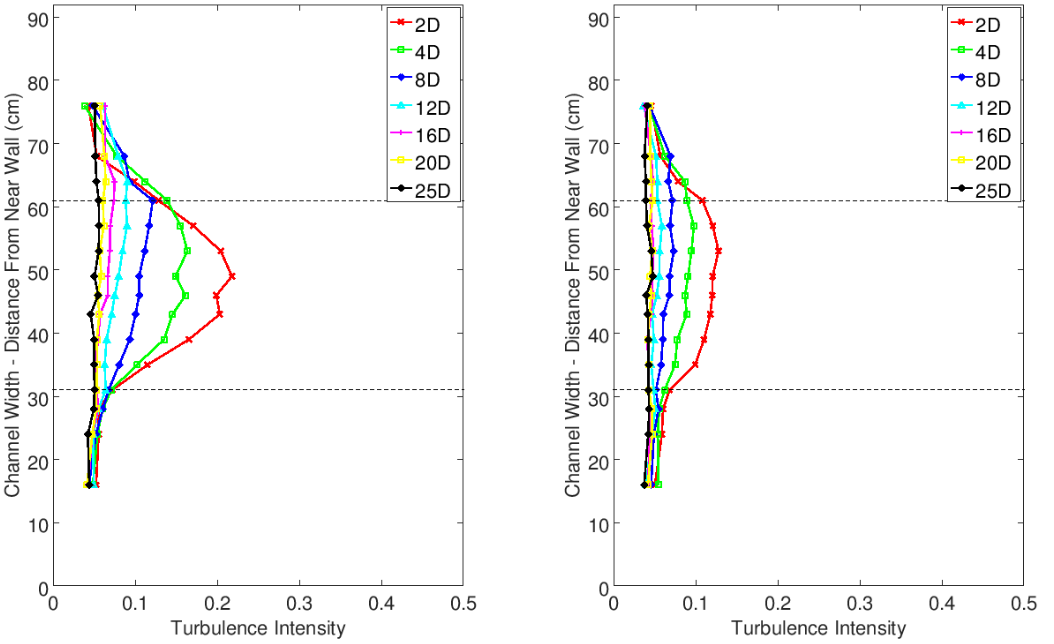

(c) I for the Contra Rotating Case at 4° pitch (d) I for the Contra Rotating Case at 6° pitch

Figure 6.19: I for the Contra Rotating Case at different pitches

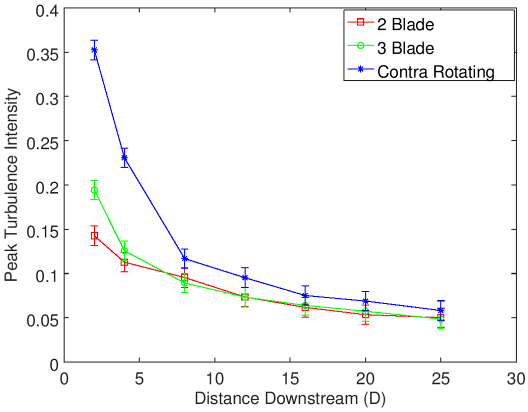

Figure 6.20: Peak I for all cases at 2° pitch

clearly present. Instead the profiles bear striking resemblance to the unimpeded flume profiles (Figures 6.3a to 6.3d), as they are gently curved across the flume. These graphs indicate that contra rotation results in minimal coherent rotational elements left in the wake. It should be remembered that these measurements are averages, and the near wake flow is expected to contain considerable fluctuations in V_Y and V_Z (as seen in the increased turbulence). However, the lack of coherence will result in faster wake breakdown. Absolute torque balance cannot be guarenteed by the set up, but an approximate torque balance appears likely.

6.4.5 Points of Note

- The immediate velocity deficit is larger for contra rotating than for any other configuration (Section 6.4.1).
- The wake of a contra rotating device is not the sum of the individual wakes of the constituent rotors, i.e. superimposition (Section 6.4.2).
- Beyond 16 D downstream the peak contra rotating V_X deficit is lower than the equivalent three blade deficit (Figure 6.18).
- Unlike the three blade configuration, meaningful recovery occurs beyond 0.1 deficit – this may be because of increased mixing caused by the contra

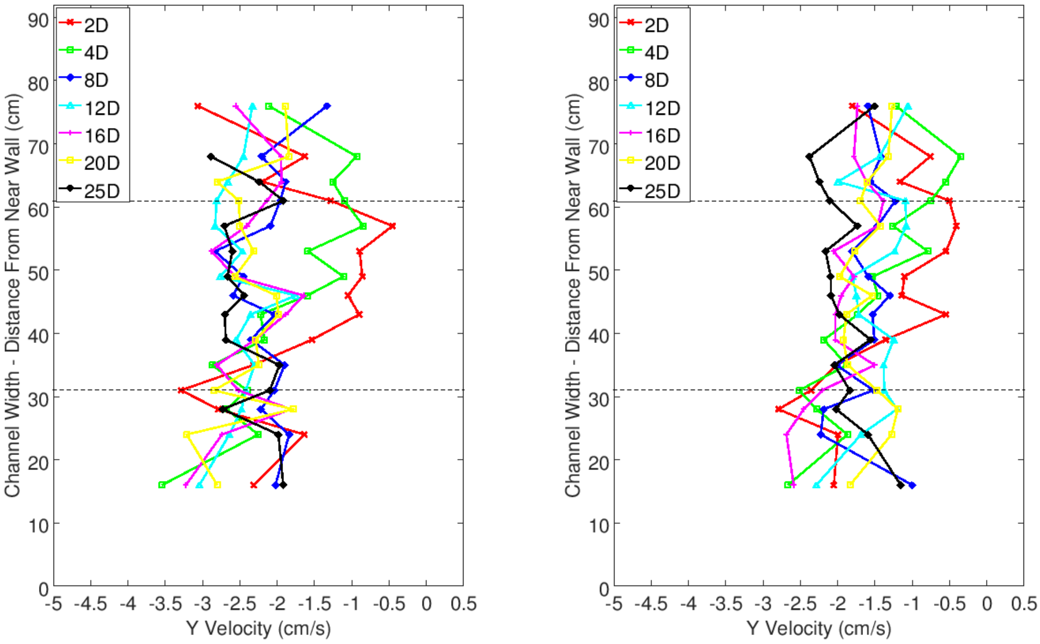

(a) V_Y for the Contra Rotating Case at 0° pitch

(b) V_Y for the Contra Rotating Case at 2° pitch

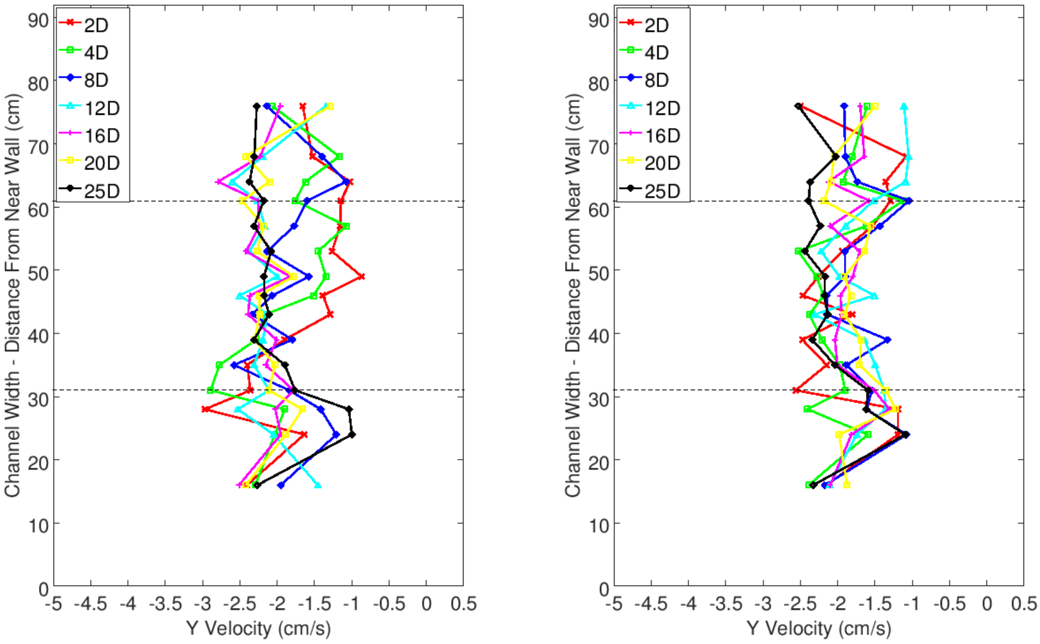

(c) V_Y for the Contra Rotating Case at 4° pitch

(d) V_Y for the Contra Rotating Case at 6° pitch

Figure 6.21: V_Y for the Contra Rotating Case at different pitches

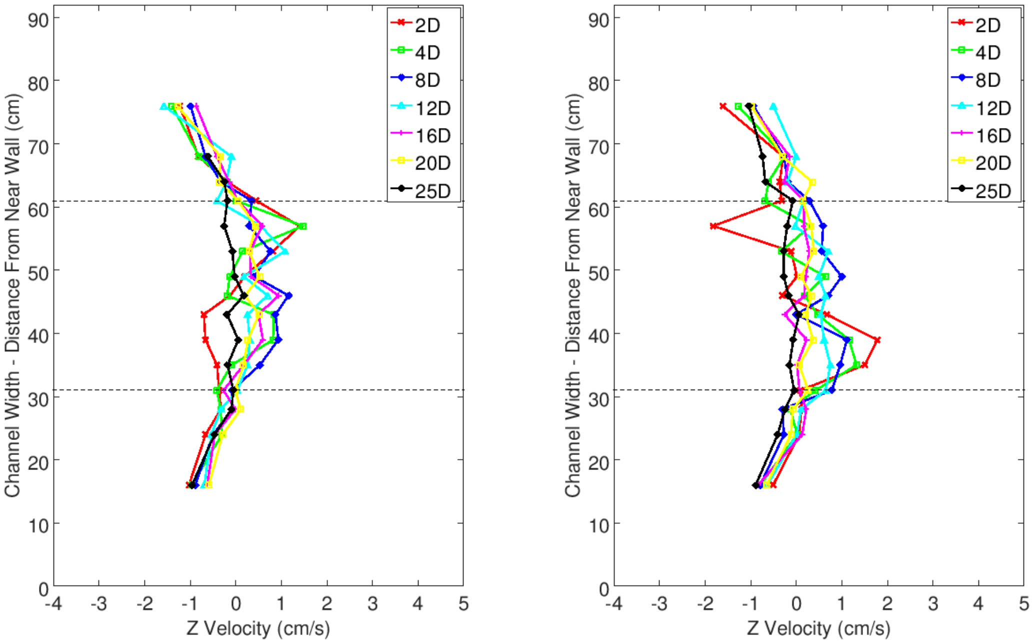

(a) V_Z for the Contra Rotating Case at 0° pitch

(b) V_Z for the Contra Rotating Case at 2° pitch

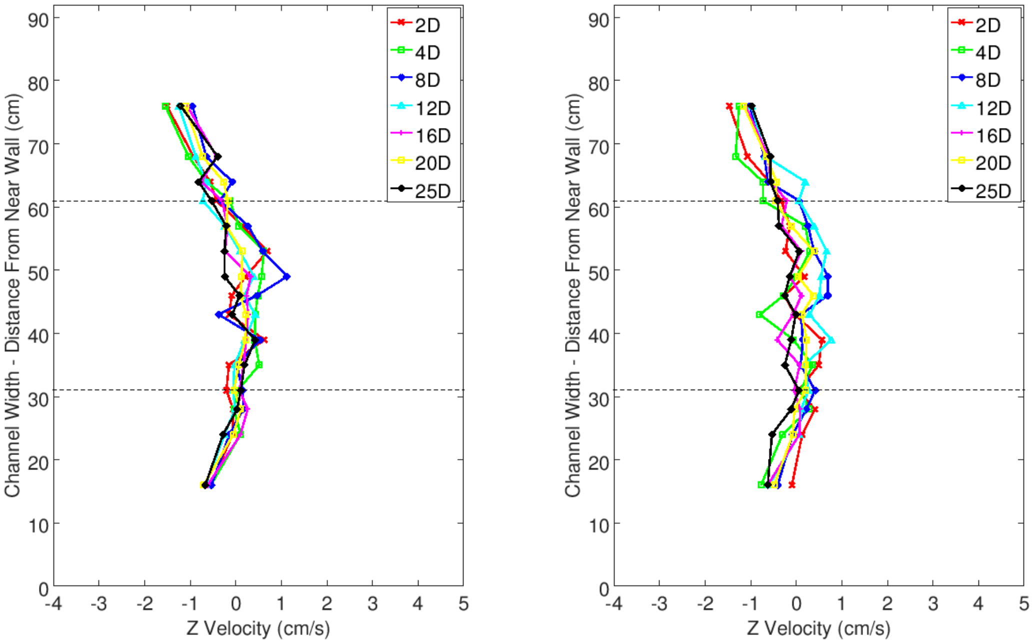

(c) V_Z for the Contra Rotating Case at 4° pitch

(d) V_Z for the Contra Rotating Case at 6° pitch

Figure 6.22: V_Z for the Contra Rotating Case at different pitches

rotating blades (Section 6.4.2).

- The higher thrust coefficient and initial velocity deficit of the contra rotating configuration does not result in a larger deficit far downstream (Section 6.4.2).
- Thus the wake of the contra rotating configuration recovers more quickly than those of the other configurations (Figure 6.18).
- As with previous configurations, the average turbulence across the flume at 25 D downstream is higher than the unimpeded flume equivalent. The magnitude of change is comparable to that of the other configurations (Section 6.4.3).
- The peak turbulence is much higher than the other configurations immediately downstream of the device, but only slightly higher beyond 8 D. This again shows that the contra rotating wake recovers more quickly than those of the other configurations (Figure 6.20).
- In the V_Z profiles the 'S' shaped profile is not visible, indicating that there is minimal coherent rotation within the wake (Figure 6.22).
- This lack of coherence results in faster wake breakdown (Section 6.4.4).
- The lack of 'S' shape suggests that an approximate torque balance is likely (Section 6.4.4).

6.5 Further Analysis of Contra Rotating Data

6.5.1 Statistical Plots

Given that the wake of a contra rotating device is formed differently to that of a single rotor device, further comparison of the flow behind the two configurations

Table 6.4: Statistical properties for data series' downstream of 2 blade and contra rotating device configurations

Parameter	Configuration	V_X (cm/s)	V_Y (cm/s)	V_Z (cm/s)
Mean	2 Blade	25.01	–2.64	–3.58
	Contra Rotating	13.10	–1.14	–0.55
Range	2 Blade	19.18	21.97	16.61
	Contra Rotating	20.75	20.51	15.68
Standard Deviation	2 Blade	2.70	2.87	2.73
	Contra Rotating	3.17	3.15	2.45
Skew	2 Blade	0.36	–0.15	0.21
	Contra Rotating	0.65	–0.03	0.21
Kurtosis	2 Blade	0.65	0.35	–0.09
	Contra Rotating	1.04	–0.23	0.35

is of interest. The statistical properties of the flows are examined and compared in this section. A series of six statistical plots are presented in Figure 6.23. These plots analyse data taken from a single data series, 2 D downstream of the contra rotating base case scenario (0° pitch). The data series measurement point is taken at hub height, in the centre line (the 7th data point from the near wall in Figure 6.16a). For comparison, the corresponding point for the 2 blade configuration is shown in Figure 6.24.

The first plot (Figure 6.23**a** and Figure 6.24**a**) gives the data V_X time series. Here the data is in its lowest form; nothing more is shown than the measurements taken from the ADV, and the average across those measurements. If an obvious trend of increasing or decreasing velocity is present (i.e. the velocity is not constant over the measurement period), it will be seen in this plot. As already discovered, the contra rotating data series (Figure 6.23 **a**) has a lower mean velocity than the 2 blade data series (Figure 6.24 **a**). This is due to the higher thrust coefficient of the contra rotating configuration, and more energy being extracted from the flow. The respective ranges of fluctuations are statistically similar, and the standard deviation is slightly larger for the contra rotating configuration (Table 6.4).

In Figures 6.23 **b** and 6.24 **b** a scatter plot is shown, with each point corre-

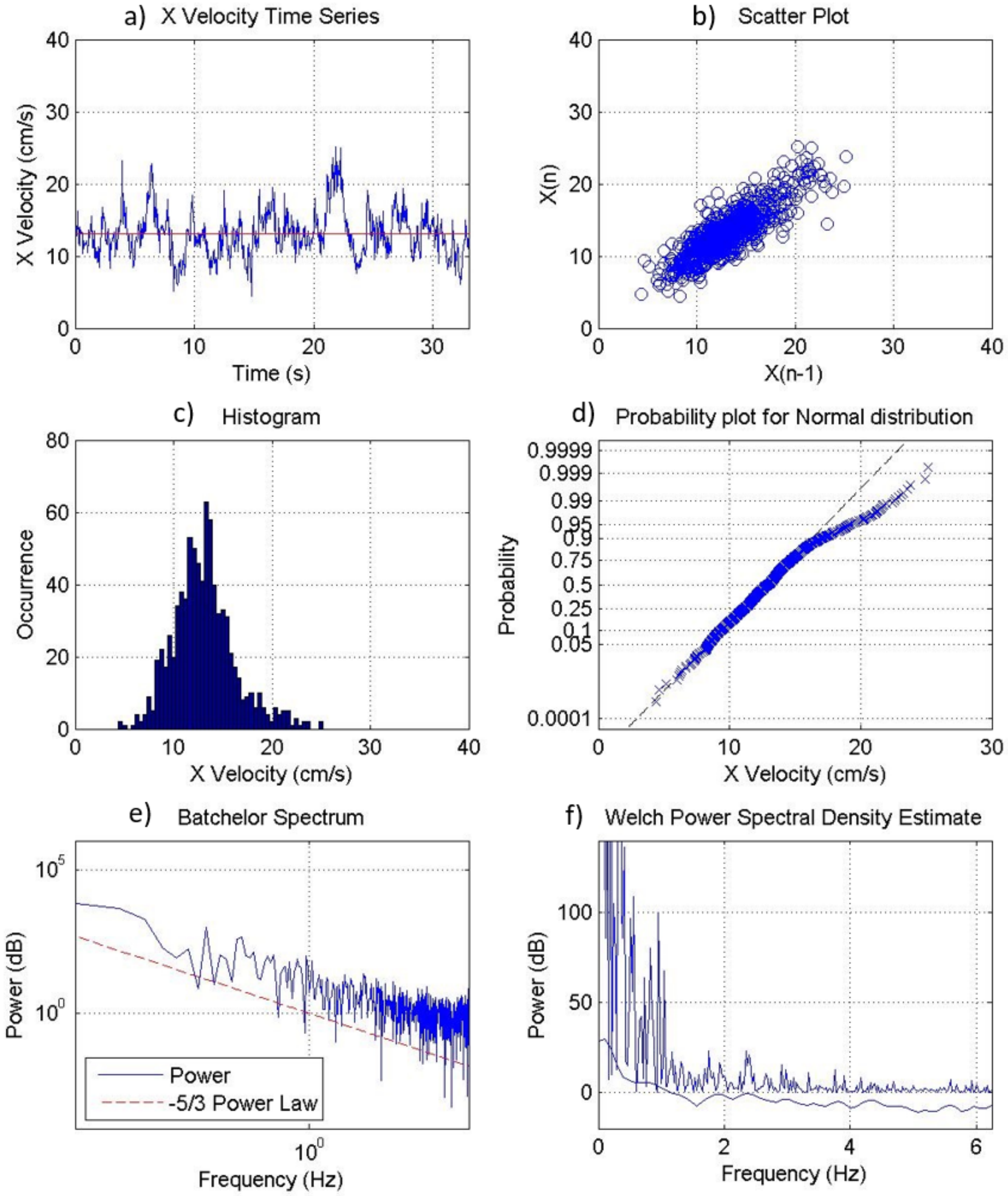

Figure 6.23: Statistical plots for V_X wake data spot reading 2 D downstream of the Contra Rotating configuration

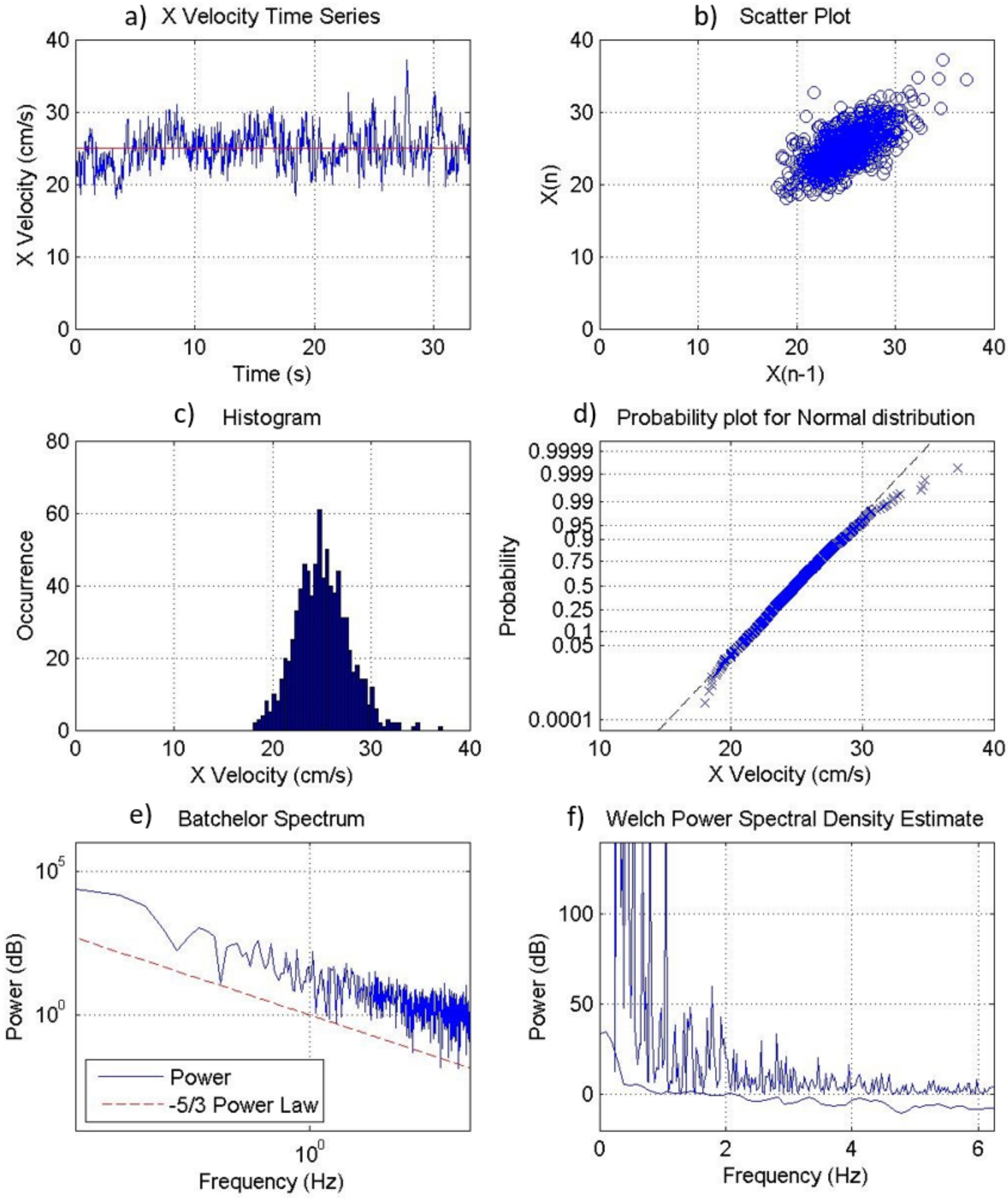

Figure 6.24: Statistical plots for V_X wake data spot reading 2 D downstream of the 2 Blade configuration

sponding to two measurements, measurement n and n–1. Plotting one against the other gives a comparison of the change in V_X over a single time step. In an ideal case, the time step will be small enough to adequately capture all velocity fluctuations. Therefore, points will deviate very little from the line $Y = X$ because $X(n) \approx X(n-1)$. If the data generally conform to this relationship any outliers will be easy to spot, and may well be an indication of instrument or processing error as opposed to a genuine physical change. In the event of the data being random or sampled in such a way as to miss the underlying trends, a shotgun scatter would be expected. It should be noted that a single point outlier would cause two outliers in the scatter plot. Both data sets can be seen to conform to $X(n) \approx X(n-1)$, indicating limited scope for single measurement instrumentation error and a suitable sampling frequency. The range and spread of the data can also be seen.

Figures **c** and **d** give an indication of the distribution of the data series. Figures 6.23 **c** and 6.24 **c** present a histogram. A normally distributed series will provide a bell curve with varying levels of skew and kurtosis. Skewness is the measure of asymmetry, or tail, in the distribution; a positive skewness statistic indicates a tail extending in the positive direction. As shown in Table 6.4 both series' are positively skewed, but the contra rotating series is more so. Kurtosis is the measure of peakedness in the distribution, with a positive kurtosis meaning a sharper peak. Both series' have positive kurtosis, again the contra rotating series more so.

The next plot, Figures 6.23 **d** and 6.24 **d** gives a probability plot for a normal distribution. The velocity data are plotted against the probability of their occurrence, and shown with a guide line to indicate the theoretical normal distribution. The closer the match to the guide line, the closer the sample is to a normal distribution. As with the histogram, this confirms the long tail of the contra rotating data.

Whilst neither data series is perfectly normal, the series taken in the wake of the contra rotating configuration has a more pronounced deviation from normality. Turbulence (or rather the velocity fluctuations that define turbulence) is often approximated as a normal distribution (George, 2013). The abnormality in the contra rotating data series may be due to the rotors providing distinct data signals to the measurement equipment, i.e. the superimposition of two non equal normal distributions, one from each of the rotors. If this is the case it is likely that these signals will quickly become mixed.

Figures **e** and **f** show the data in the frequency domain, having undergone a Fast Fourier Transform (FFT). In Figures 6.23 **e** and 6.24 **e** the theoretical Kolmogorov's law is illustrated alongside the transformed data, on a log-log scale. Kolmogorov's law, or the -5/3 power law, is the line along which the energy decays from large low frequency to small high frequency eddies (as discussed in Section 2.1). This is applicable to turbulent flows, but not necessarily to non-homogenous flow structures. The plot also gives an indication of the magnitude of the energy cascade. The magnitude of the power varies depending on the flow characteristics, but the turbulent breakdown will mean that the energy decay takes on the same gradient at all times (the -5/3 power).

Finally, Figures 6.23 **f** and 6.24 **f** gives the data in the form of an FFT, showing the energy corresponding to each frequency. This plot is used to identify the frequencies at which a peak in energy is experienced. These peaks may be due to tank vibration, vortex shedding, blade shadowing or other reasons, with each cause having a specific frequency. In the two blade configuration FFT a spike may be seen at approximately 2 Hz, corresponding to half the rotational frequency of a blade passing. This spike is also present in the Y and Z domains (see Appendix A). Additional spikes can be seen at 0.9 Hz, 2.1 Hz, 2.9 Hz and 3.75 Hz. These do not correspond to the blade frequencies of the turbine. The power of the spikes in the contra rotating configuration is smaller than that of the two blade configuration, likely because the mixing caused by the contra rotation has already broken down significant coherence in the wake. This appears to conform to the idea of a lack of coherent structure within a contra rotating wake.

The same plots for the V_Y and V_Z components are shown in Appendix A in Figures A.1 to A.4.

6.5.2 Points of Note

- The range and spread of the contra rotating and single rotor data sets are similar.
- The contra rotating data is less normal than the single rotor data; it has a long tail (positive skew) and sharper peak (positive kurtosis).
- Whilst the single rotor data set shows regular, obvious peaks in the frequency domain, including a peak corresponding to blade passage, the contra rotating data set shows smaller peaks which do not obviously correspond to the blade passage frequency, as the peaks are reduced by the mixing occurring at the rotor.

6.6 Blockage and Scaling

6.6.1 Blockage

The blockage ratio was 18.7 %, and no change in surface elevation was noted at any point in any configuration. As with the pile mounted experiments, the blockage caused flow acceleration around the device. This acceleration was greater in magnitude than previous experiments, but showed a more obvious recovery. Generally, the larger the deficit immediately behind the device (and thus the larger the C_T), the larger the flow acceleration around the device, with the greatest acceleration occurring in the contra rotating configuration. On either side of the rotor the acceleration was similar. Again the flow was shallower than the 4 D required to remove boundary effects fully from the wake recovery (specified in Myers, Bahaj and Germain (2008)). However, as mentioned previously it is likely that full scale devices may also be positioned in water depths shallower than 4 D.

6.6.2 Scaling

Although devices used here are not designed to model any specific full scale device, a comparison still proves interesting. Were these results to be replicated for a 20 m device, its wake would return to 90 % of the free stream velocity at approximately 320 m downstream of the device (16 D), with little further recovery by 500 m downstream (25 D). For the single rotor devices, there could still be evidence of the near wake at least 160 m downstream (8 D), and possibly beyond.

6.7 Conclusion

This chapter has presented velocity and turbulence wake data for a range of turbine configurations.

The working section was chosen as an approximately constant velocity and turbulence region. As before, V_X data were normalised against unimpeded flume data to mitigate against any cross sectional and measurement session inconsistencies.

In the chosen base case configuration the peak velocity deficit was 0.46. All measurement points had recovered to 90 % of the freestream velocity by 16 D downstream. This did not necessarily indicate a fully recovered wake. Acceleration to 110 % of the freestream velocity was noted outside the rotor area, and although this reduced with distance downstream, it remained present into the far wake. The turbulence peaked at over 13 %, compared to ambient levels of 4 – 5 %. A strong ‘S’ shaped profile behind the rotor was seen in the V_Z results, as the blades forced flow up or down, depending on the direction of rotation. As expected this ‘S’ shape was not detectable far downstream. This result gave credence to the use of actuator discs as an approximation of rotors when examining the far wake (as an actuator disc assumes rotation does not need to be accounted for in the far wake). This is borne out by the minimal rotation found in the far wake of the rotor. However, the length to which the rotation persists indicates the near wake can extend further than is commonly assumed. In these experiments there was evidence of rotation at 8 D downstream. This evidence was from averaged velocity data and it is quite possible that if measurements were synchronised to blade frequency evidence of wake rotation would be found even further downstream.

For the two blade, three blade and contra rotating cases the wake had not fully recovered by 25 D downstream. This is a considerable distance, and could impact choices made when considering array spacing, as most arrays will require a trade off between packing density and wake recovery.

It was noted that an increase in blade numbers resulted in an increase in C_T, as the thrust generated by the rotor (and so the wake deficit) increased. However, the thrust generated by two sets of contra rotating rotors was considerably less than the sum of the two rotors operating independently.

As was expected, an increase in blade pitch angle usually resulted in a decrease in rotational speed, which in turn resulted in a smaller wake. However, this was not the case for 2° pitch, which had a lower rotational speed but a larger wake profile than that of 0° pitch. This was due to the rotor at 0° pitch over-speeding, and the optimum pitch angle being somewhere between 0 and 2° pitch. The lower deficits of the high pitch configurations corresponded to the wake recovering in a shorter distance, though not at a faster rate of recovery.

The addition of an extra blade to the rotor allowed more rigorous analysis of the contra rotating device, but also provided an opportunity for comparison in its own right. Whilst the results were broadly similar to that of the two blade configurations, the deficits were larger, peaking at 0.6. As with the two blade results there was a large recovery between 2 – 8 D, and a more gentle recovery after this. Between 16 – 25 D downstream the maximum deficits did not recover greatly, remaining around 0.1. As these maxima were in the form of clear peaks this indicated that the flume was not fully mixed, and mixing was occurring very slowly.

For the contra rotating configurations the wake was larger than for any other configurations, with a peak deficit of 0.75 at 0° pitch. However, it appeared that the contra rotation facilitated more effective flume mixing, as in the far wake the recovery continued beyond that of the three blade configuration. The contra rotating configuration had the largest C_T of all the configurations, but resulted in a faster recovery than the three blade configuration. This was due to the second rotor removing structure and coherence from the wake. As the contra rotating device's higher thrust does not result in a larger deficit downstream, this could have significance for the layout of arrays when packing density is considered. Contra rotating devices could be used to reduce wake lengths, making an array more efficient.

The 'S' shaped profiles visible in the V_Z direction for the two and three blade configurations were much less clear for the contra rotating configurations. Thus, as predicted by Hansen (2008), a large amount of the rotational element within the flow was removed by the second rotor. This may be what drove the improved mixing within the wake, which led to a faster wake recovery. This enhanced wake recovery may be employed benificially in array layout, allowing a greater packing density without adverse effects.

Results in the wakes of the contra rotating and 2 blade configurations were further compared using statistical measures. For the data points analysed the wakes were found to have a similar velocity range and standard deviation, but the measurement in the wake of the contra rotating turbine conformed less to the normal distribution, and suggested better mixing.

Chapter 7

Results Comparison With Similar Experiments

This chapter makes some comparisons between the results from Chapters 5 and 6, and then with Chapter 6 and selected similar work from literature.

7.1 Comparisons Between Pile Mounted and Wire Hung

Table 7.1 repeats the configurations tested for both regimes.

Figure 7.1 compares the peak velocity deficits of the two standard cases (as seen in Figures 5.17 and 6.5a, repeated in Figure 7.2 for clarity). It can be seen that the immediate deficit of the wire hung tests far exceeds that of the pile mounted, for the same number of blades. The significant differences in the two experiments are the rotor diameters and the blade types. The higher rotor diameter of the wire hung device gives a larger rotor area, capturing more of the energy within the channel. The aerofoil profile blades of the wire hung device are far more efficient, and also result in higher energy capture. A larger energy capture must by definition result in a larger immediate wake.

Table 7.1: λ and C_T for all configurations tested

Regime	**Configuration**	**Lambda**	**CT**
Pile Mounted	Sensitivity	3	0.48
	Base Case	4	0.45
	Sensitivity	5	0.4
Wire Hung 2 Blade	0 deg Pitch	5	0.67
	2 deg Pitch	4.7	0.68
	4 deg Pitch	2.3	0.43
	6 deg Pitch	2.3	0.3
Wire Hung 3 Blade	0 deg Pitch	4.7	0.84
	2 deg Pitch	2.9	0.74
	4 deg Pitch	2.3	0.58
	6 deg Pitch	1.2	0.46
Wire Hung Contra Rotating	0 deg Pitch	4 / 4.1	0.93
	2 deg Pitch	4.2 / 3.6	0.97
	4 deg Pitch	1.5 / 3.4	0.88
	6 deg Pitch	2.3 / 2.5	0.48

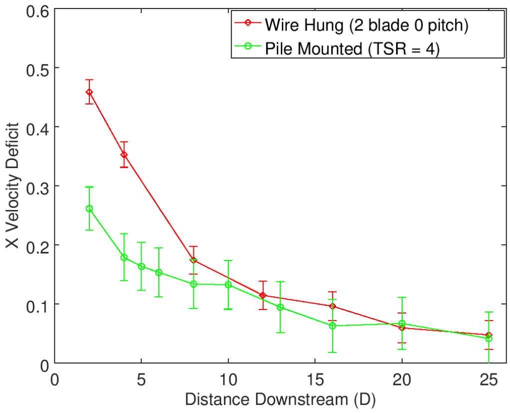

Figure 7.1: Comparison of peak deficits in the Pile Mounted and Wire Hung base cases

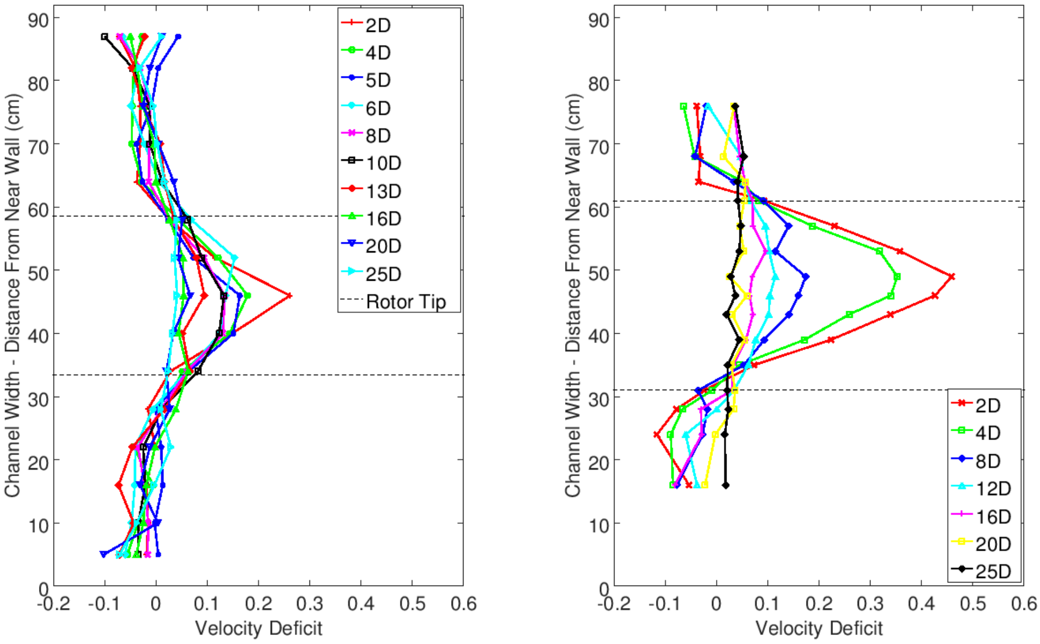

(a) V_X for the Pile Mounted Base Case of $\lambda = 4$ (as seen in Figure 5.17)

(b) V_X for the Wire Hung Base Case of 2 Blades at 0° pitch (as seen in Figure 6.5a)

Figure 7.2: Comparison of Pile Mounted and Wire Hung base cases

Far downstream of the device both standard cases have recovered to < 0.1. However, the wake of the pile mounted device appears to be more prominent than that of the wire hung device. This difference is unexpected, as ambient turbulence levels are similar (recalling Figure 4.9). Results are compared at 20 and 25 D downstream for the wakes of both configurations (Figure 7.3), which shows that the deficit in the rotor area is comparable, and the difference in wake prominence is caused by the negative deficits recorded at the edges of the channel. It can also be seen that there is evidence of recovery noted between 20 and 25 D downstream for both the pile mounted and the wire hung configurations. Uncertainties are larger for the pile mounted results than for the wire hung results, due to the effect of flume inconsistency. This is because results for wire hung configurations were taken from a single measurement session.

Tip speed ratios are comparable between the pile mounted device at $\lambda = 5$ and the 2 bladed wire hung device at 0° and 2° pitch, however thrust coefficients are

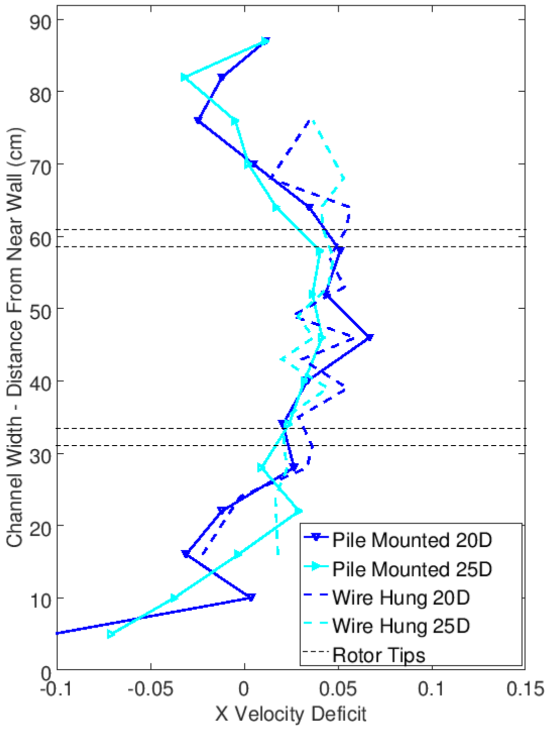

Figure 7.3: Velocity deficit in the far wake for the Pile Mounted and Wire Hung base cases. Pile Mounted rotor extent is shown by the inner dashed lines, and Wire Hung by the outer.

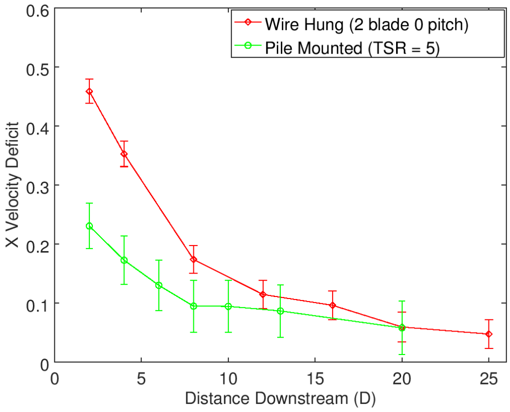

Figure 7.4: Comparison of Wire Hung base case and Pile Mounted $\lambda = 5$ for λ similarity

greater for the wire hung tests. This can be seen in Figure 7.4 which compares results from Figures 5.31 and 6.5a (repeated in Figure 7.5 for clarity). Initial deficit for the same value of λ is much greater for the wire hung device, due to the more efficient profiled blades. The wake area can also be seen to be wider, due to the larger diameter rotor used.

As C_T has been calculated from the velocity deficit, configurations of similar C_T will have a similar initial velocity deficit. The pile mounted base case and the wire hung 2 blade device at 4° have similar C_T, and are compared in Figure 7.6. It can be seen here that the rate of wake recover is extremely similar, particularly in the far wake. Bahaj *et al.* (2007) states that the recovery in the far wake is primarily dependent on the ambient turbulence, which is reflected in Figure 7.6.

7.2 Comparisons Between Wire Hung Tests and Literature

The wake of the wire hung device is more representative of full scale devices and devices used in literature, due to the profiled wake blades. Furthermore there is a lower uncertainty within the wire hung data. The following section compares

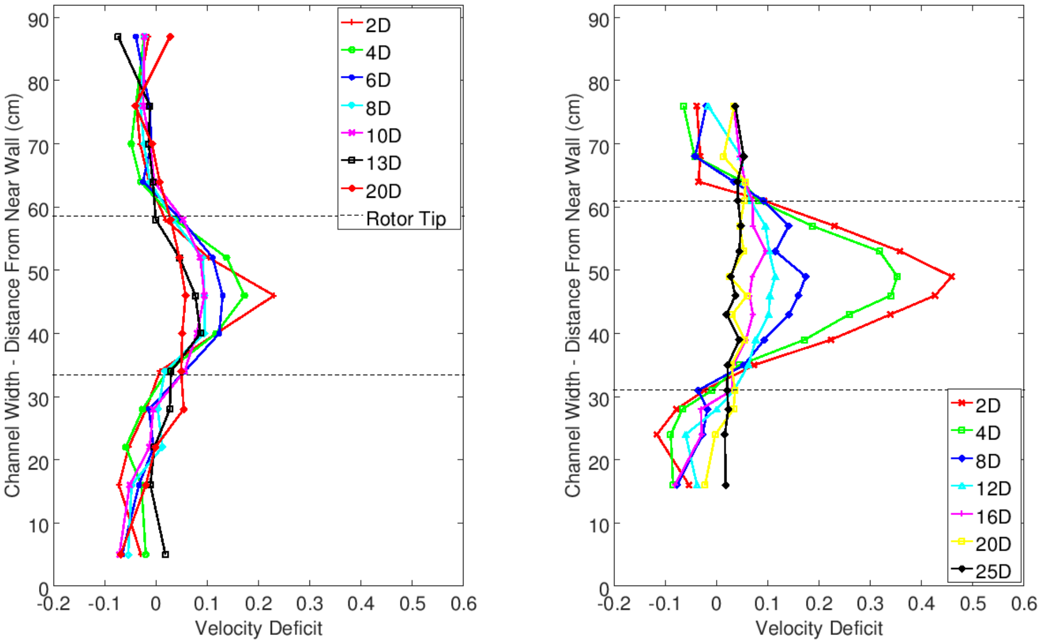

(a) V_X for the Pile Mounted Base Case of $\lambda = 5$ (as seen in Figure 5.31

(b) V_X for the Wire Hung Base Case of 2 Blades at 0° pitch (as seen in Figure 6.5a

Figure 7.5: Comparison of Pile Mounted $\lambda = 5$ and Wire Hung base case

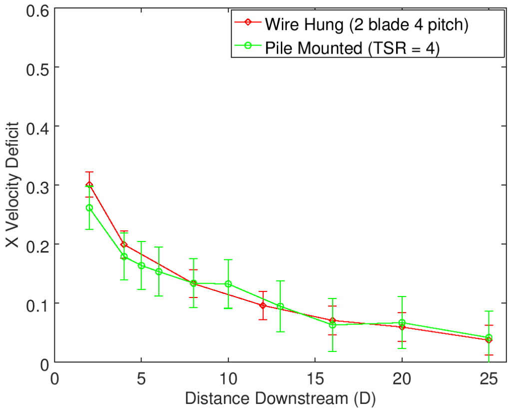

Figure 7.6: Comparison of Wire Hung 2 blade 4 pitch and Pile Mounted $\lambda = 4$ for C_T similarity

the wire hung device with selected results from literature, discussed in Chapter 3.

7.2.1 Single Rotor Devices

In Myers (2005) downstream velocity deficit measurements are given for three flume velocities from 3 – 7 D downstream of an actuator disc, and a correction factor is given. Recovery is noted to be less than predicted by other work, and this is explained by the low ambient turbulence (although no turbulence measurements were taken). When compared with the work presented in this document the Myers deficits are larger at 3 D downstream, but are similar in the rate of recovery. As the Myers results do not extend beyond 7 D, a full comparison is not possible.

In Myers and Bahaj (2009b) velocity deficit is given up to 10 D downstream of a rotor. The results support the claim made in Section 5.2 that the wake of the structure has little effect in the far wake. Previous studies are said to suggest a distance of 15 – 20 D for a wake recovery of 85 – 92 %; the experimental work in Chapter 5 and Chapter 6 broadly conform to this. Downstream deficit is shown as ranging from about 0.55 at 3 D to 0.22 at 10 D for a thrust coefficient of 0.77. The recovery rate conforms to those presented in Chapter 6, over the given distance, but the absolute deficit is greater for Myers and Bahaj (2009b).

Myers and Bahaj (2009a) provides an interesting comparison with the results presented here, as the data set extends to 20 D downstream. As shown in Figure 7.7 the deficit recovery gives a good match to the 3 blade, 0° pitch device presented in Section 6.3 over the length of the measurements, indicating a similar wake recovery rate. However, there the deficit magnitude is offset by approximately 1 D, suggesting a spatial lag in the decay. The idea of spatial lag is briefly discussed in Roc, Conley and Greaves (2010), where it is proposed that the lag is because of non rotation (from the actuator disc), and is a near wake issue. It can be seen in Figure 7.7 that from approximately 16 D downstream the deficits

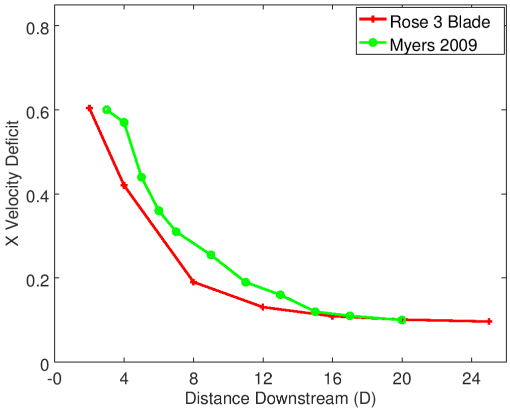

Figure 7.7: Velocity deficit comparison between Rose 3 blade device and that found in Myers and Bahaj (2009a)

would match excellently without any lag, and both sets of results suggest minimal recovery beyond a deficit of 0.1. This failure to recover meaningfully beyond 0.1 is significant as it results in a potential power reduction of 27 % for any device positioned downstream. However, it should be remembered that even at this distance downstream there is a difference in velocity deficit between the centreline and the rest of the channel (Figure 6.11a), meaning that further mixing, and thus further recovery, is still to occur.

In Polagye (2009) the deficit of simulated turbines has returned to less than 0.1 within 20 D, which is similar recovery to that of simulations reported in Harrison *et al.* (2009), but much slower than wind turbines, which are reported to recover to 0.07 within 10 D. Polagye also finds that even at 60 D downstream there is a velocity deficit present, indicating that complete recovery requires a very long time or length scale, considerably longer than is available in most flume tanks and longer than is reasonable for array spacing.

Maganga *et al.* (2010b) gives velocity deficit data for a 700 mm, three blade turbine for the first 10 D of the wake. Wake recovery is reasonably consistent along the distance, reaching 0.16 at 10 D downstream. The turbulence intensity of 8 % is slightly higher than that used in this study, where the recovery is similar, as can be seen in Figure 7.8.

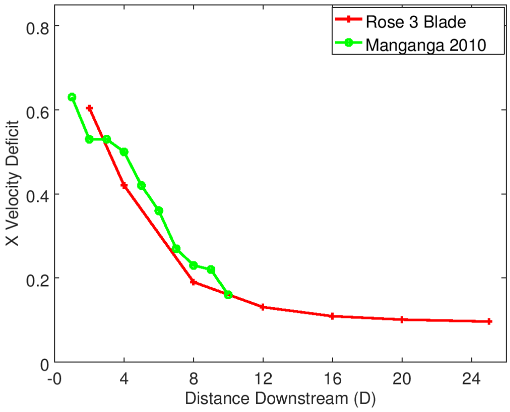

Figure 7.8: Velocity deficit comparison between Rose 3 blade device and that found in Maganga *et al.* (2010b)

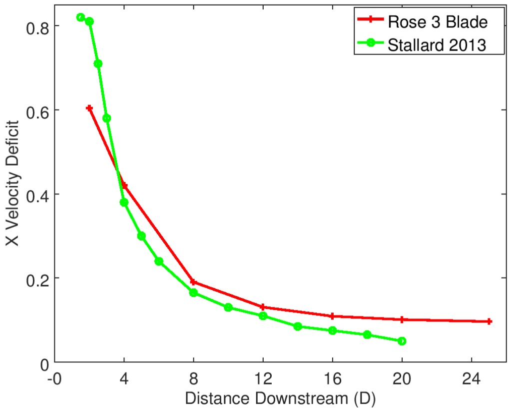

Figure 7.9: Velocity deficit comparison between Rose 3 blade device and that found in Stallard *et al.* (2013)

In Stallard *et al.* (2013) the wake behind a similar sized, 3 blade rotor is given up to 20 D downstream. The velocity deficit is given in Figure 7.9, where it can be seen that it is higher immediately behind the rotor, and lower from 4 D downstream. The initial high deficit may be due to the higher C_T employed by Stallard (0.87). The greater rate of recovery may be due to the higher ambient turbulence intensity (8 - 10 %) causing a more rapid wake breakdown, which may also be seen by the wake continuing to recover significantly beyond the point where it reaches 0.1.

Figure 7.10 also compares with results from Chen *et al.* (2017), which uses

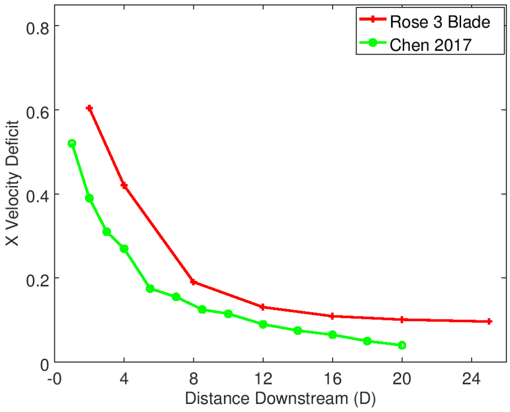

Figure 7.10: Velocity deficit comparison between Rose 3 blade device and that found in Chen *et al.* (2017)

a 3 blade, 30 cm diameter rotor. The velocity deficit is is lower at all distances downstream the for the work presented here. This may be due to the lower C_T of Chen (0.39); Chen also mentions that blockage effects increase mixing in the near wake.

In various literature relating to wind turbines, the near wake / far wake transition is given as being between 2 – 5 D (e.g. Vermeer, Soerensen and Crespo (2003)), beyond which the coherent structure has broken down. This is also the case for some tidal turbine literature (e.g. Bahaj and Myers (2013)). In Figures 6.10b and 6.15b, evidence of a rotational structure is seen at 4 D and is also visible at 8 D, indicating that the transition zone may reach as far as 8 D downstream, or even beyond.

7.2.2 Contra Rotating Devices

Unfortunately, but not unexpectedly, the author was unable to obtain any velocity data from published literature in the wake of a contra rotating turbine. However, as previously noted, Hansen (2008) states that an ideal contra rotating turbine will leave no rotational velocity within its wake. Figure 6.22a goes some way to demonstrating this, as it shows a significant reduction in structured V_Z

compared with Figure 6.10a or Figure 6.15a, as discussed in Section 6.4. The effectiveness of the second rotor in removing swirl from the wake may be dependent on factors such as torque balance or relative rotational speed – factors which were not considered in detail within the scope of this research. Thus from these experiments the effect cannot be said to be absolute or recurring in all circumstances, but it can be said that the effect occurs.

As mentioned in Section 3.5.2 O'Doherty *et al.* (2009) models a contra rotating device using CFD, and compares this with a single rotor. It finds that the overall wake recovery is similar for both (despite the contra rotating device having a higher C_T), but the wake of the contra rotating device makes a greater initial recovery. The increased initial recovery is consistent with results presented here, and in both the contra rotating device's higher coefficient of thrust and initial velocity deficit does not result in a higher velocity deficit downstream. However, in this work the improved recovery continues into the far wake.

The increased rate of wake recovery may result in a significant benefit when considering array spacing. The faster wake breakdown can be used either to decrease the distance between devices, increasing packing density; or it can be used to obtain more recovery over the same distance. It would be for an array developer to decide which of these options is preferable.

7.3 Conclusions

In this chapter comparisons have been made between the Pile Mounted results described in Chapter 5 and the Wire Hung results described in 6. The Wire Hung configurations result in a higher velocity deficit and C_T for a given λ, due to the profiling of the blades. Wake recovery is noted for both configurations at distances far downstream, and the rate of recovery in the far wake is similar, as it is dictated by ambient turbulence.

Comparisons have also been made between the Wire Hung results discussed in this report and results found in literature. Due to the lack of published data, limited comparisons have been made with the contra rotating device. It can be seen from Figures 7.7 to 7.10 that despite comparing different devices, in different channels, operating in different conditions, with different measurement equipment and methodology, the wake deficits are remarkably similar. One particular point of agreement between Myers and Bahaj (2009a) and the three blade configuration discussed in Chapter 6 is the very slow to negligible wake recovery from about 16 D downstream, usually at around 90 % of the freestream velocity. The lack of meaningful recovery beyond this point should certainly inform turbine array spacing. Differences in deficit do exist within the near wake, (e.g. initial deficit and initial recovery rate) but these can likely be attributed to the variation in devices tested. In this study evidence of the near wake was found for various configurations at 8D downstream. This exceeded the near wake length suggested by Bahaj and Myers (2013) or Myers and Bahaj (2009b), or the rotation found in Chen *et al.* (2017). It should be noted that the experiments of Myers and Bahaj (2009a) and Maganga *et al.* (2010b) use ambient turbulence levels similar to that used in Chapters 5 and 6, whilst Stallard *et al.* (2013) uses higher turbulence and Chen *et al.* (2017) lower.

Chapter 8

Conclusions

8.1 Summary of Work

8.1.1 Pile Mounted Experiments

In Chapter 4 a description was given of the testing of a pile mounted tidal turbine device. The wake was profiled by measuring the three dimensional instantaneous velocity at certain points downstream of the device, using an Acoustic Doppler Velocimeter. The results were presented and discussed in Chapter 5. The wake of the hub and its supporting pile was found to have a small impact on the near wake, and the wake of the structure corresponded to that given in literature for a cylinder. The wake of the gravity base was initially more considerable, but had little influence beyond 6 D downstream, and then only at the base of the channel. Thus any wake detected far downstream could be assumed to be due to the rotor as opposed to the structure (Section 5.2).

The wake behind the device operating at $\lambda = 4$ peaked at a turbulence intensity of 26 %, then showed continuous recovery from 2 – 25 D downstream, implying that a greatly reduced wake was still present far downstream (Figures 5.17 and 5.18). That the wake remained present when C_T was only 0.45 indicated considerable longevity within the wake structure. As would be expected, the largest deficits were predominantly to be found in the rotor axial centreline (Section 5.3).

Increased and decreased values of λ gave small changes to the thrust and wake, though the recovery remained broadly similar (Figure 5.35). The changes in λ provided corroboration for the previous tests, as the wake continued until far downstream (in this case 20 D) (Figure 5.34). The limited velocity recovery far downstream showed that the breakdown of the wake structure occurred more slowly than might have been anticipated (Section 5.4).

8.1.2 Wire Hung Experiments

Chapter 4 also contained a description of the testing of a wire hung turbine, which had a small nacelle and minimal support structure. This device was capable of variations in blade number and blade pitch angle, and was able to hold two contra rotating rotors. The wake profiles of multiple configurations were measured in the same flume as the previous experiments. The results were presented and discussed in Chapter 6.

The base case (2 blade) peak deficit of 0.46 greatly exceeded that of the previous experiment, because the greater rotor diameter and more effective blade profile led to higher thrust generation. This wake deficit had reduced to less than 0.1 by 16 D, but evidence of wake presence persisted to the limit of downstream measurement (25 D) (Section 6.2.1). In the Z direction a clear picture of the rotation imparted to the flow was given, the dissipation of this (between 8 and 12 D downstream) signalled the start of the far wake (Section 6.2.4).

An increase in blade pitch angle generally resulted in a slower rotation, a smaller thrust, and thus a smaller wake Figure 6.5). At 0 to 2° pitch this was not the case, due to over-speeding in the 0° pitch case. The addition of an extra blade resulted in higher thrusts and therefore larger wakes (Section 6.3). As a peak velocity deficit was seen at all distances downstream (for the faster, lower blade pitch angles) it was clear that the wake was not fully mixed with the surrounding flow, even far downstream (Section 6.3.3). This was further confirmation of the phenomena observed in the pile mounted experiments.

The contra rotational configuration provided evidence that wakes from contra rotating devices do not behave in the same way as wakes from single rotor devices. Although the wakes from contra rotating configurations generated the most thrust, they recovered faster than in the three blade configuration (Section 6.4.2). Further, the rotational element of the wake so clearly visible in the V_Z profile for the single rotor cases was greatly obscured in the contra rotating cases (Figure 6.22). This illustrated a potential benefit of contra rotation when considering wake effects on packing density.

The contra rotating wake data is found to conform less to a normal distribution than the single rotor device immediately downstream of the device (Section 6.5.1). It is also more difficult to see blade rotation frequencies in the frequency domain, as these signals have been obscured by mixing at the rotor.

In Vermeer, Soerensen and Crespo (2003) the near wake is said to end 2 – 5 D downstream, and in Myers and Bahaj (2009b) the swirl is said to be dissipated by 4 – 5 D. In Figure 6.10a and Figure 6.10a the swirl within the flow can clearly be seen at 4 D, and less clearly at 8 D. This indicates that in this experimental work the transition from near to far wake is at least at the limits of the 5 D suggested elsewhere, and may even extend beyond it.

A number of studies find a wake recovery to 90 % freestream by 20 D downstream, and often before that. Of those mentioned in Section 3.4, only Stallard *et al.* (2011) reports any differently (88 %). This is broadly the case for configurations mentioned within this work. However, there is still a peak across the channel in the rotor area (indicating that the wake has not fully mixed) and the recovery beyond this appears to be very slow.

8.2 Potential Application to the Development of Tidal Energy Capture

8.2.1 New Data Sets

Through the experimental testing detailed in Chapters 4 to 6, a number of new data sets are presented for the wakes of tidal turbines. These data sets give small scale testing results, primarily in the form of velocity and turbulence profiles, for a variety of turbine configurations. These data sets offer measurements up to 25 D downstream of the device, longer than most of that which is currently available. They provide a basis for comparison for any past or future experiments or computational simulations.

8.2.2 Length of Wake

For all configurations where measurements were taken at 25 D the wake is observable. This is equivalent to a distance of 500 m downstream for a device of 20 m diameter. For the wire hung results, the wake at 25 D shows a deficit of approximately 0.1, but is still detectable. A deficit of 0.1 has sometimes been used as an arbitrary designation for wake recovery, and whilst this may be appropriate in some circumstances, even at a deficit of 0.1 the wake has not fully recovered. A 10 % reduction in velocity to the inlet of a turbine is very significant, and could threaten the economic viability of a device, or even an array. The recovery beyond 25 D downstream is expected to occur slowly, and the wake may extend far downstream of this. The downstream distance required before the velocity deficit becomes acceptable depends on the input requirements of the device downstream.

Furthermore, individual array layout depends heavily on the device and the location, but it is likely there will be many locations where packing needs to be tighter than 25 D downstream. Developers designing for such locations should examine the wake effects specific to their devices.

There may also be an increase in small scale turbulence at 25 D downstream, relative to ambient. Although only a very small increase in turbulence was observed at this distance, it has been noted previously that frequencies below 12.5 Hz could not be measured with the equipment used. This turbulence is likely to be small enough in scale that it has no undesirable impact on a downstream device.

8.2.3 Near Wake/Far Wake Transition

In certain experiments reported here the near wake appears to extend further than the distance usually ascribed to the transition zone. The near wake is defined as the part of the wake with coherent structure, and the far wake is where that coherent structure has been broken down. In certain results (e.g. Figure 6.10a) the rotational aspect of the flow is detectable at 8 D downstream. This is an interesting observation which indicates that in this case the rotational wake structure breaks down less easily than predicted.

This work suggests that the near wake extends beyond the commonly mentioned 5 D, and care needs to be taken when interpreting results from actuator discs in this region. Actuator discs are commonly used to model wakes, under the proviso that they are not used to represent near wakes as they offer no rotational aspect. Thus if the transition zone extends to approximately 8 D, the actuator disc results will be less useful upstream of this point.

An increase in the region of swirl expected (i.e. the near wake) has the potential to increase environmental concerns, as it may increase seabed scouring, bathymetry changes or other ecological changes at a given location.

8.2.4 Contra Rotation

The contra rotating device is a novel concept which has numerous advantages over the traditional monopile device. The results shown in Section 6.4 suggest that one of those advantages is an increased wake recovery. Despite having a higher C_T than the two and three blade devices, the wake of the contra rotating configuration recovers to a similar level by 16 D (Figure 6.18). This improved rate of wake recovery is likely due to the lack of coherent structure within the wake, allowing for faster mixing.

Another effect of the contra rotation is a reduction in swirl in the near wake. This reduction is unlikely to have any direct effect on the downstream device unless it is positioned very close, but could impact local bathymetry, as well as the habitat of plants and animals. Considering a point on the seabed in the near wake of a turbine, it is unclear whether the periodic velocity fluctuation caused by a single turbine device creating high swirl would be preferable to the more constant wake of a contra rotating device. It may be that the single rotor device wake scours the seabed by pushing debris out the sides of the wake, whilst the contra rotating device wake scours the seabed by keeping debris in the wake, pushing it downstream. Whilst many devices will be sufficiently raised up from the seabed so as to have minimal impact over the near wake area, some devices are gravity based and can expect to have some impact on the seabed downstream of the device.

8.2.5 Impact on Array Spacing

Any array development will be faced with many competing considerations, involving materials, installation methods, distance from shore, robustness and maintenance, power capture, and many other considerations. Within this mix there must be due consideration of the wake effects of one device upon another. Due to the spacial limitations of most sites it is inevitable that some devices will be placed in the wakes of others. The change in velocity and turbulence profiles experienced by these devices will alter performance and survivability. It is for the developer to decide what levels of change from ambient are appropriate, and this will be dependent on the specifics of the device, the required operational performance, and the allowed maintenance schedule.

Throughout this work no array testing has taken place, and any conclusions are as a result of an extrapolation of the results. Nevertheless there are some pertinent points affecting array spacing. This work suggests there is still evidence of the wake present at 25 D downstream, and array developers must take this into account. The wire hung three blade configuration maintained a peak of 0.1 velocity deficit at 25 D downstream. A 10 % reduction in flow velocity results in a 27 % reduction in power available, a very considerable amount. If the (in this case incorrect) assumption was made that wakes could be neglected for devices spaced 25 D apart, the generated power output would be significantly less than the predicted power output, potentially threatening the economic viability of the array. However, increasing the distance between devices within an array beyond 25 D may provide limited benefits. The velocity recovery in the far wake was observed to occur very slowly, and it would be reasonable to expect a continuation of this. A further 5 or 10 D may provide little recovery, and thus little extra available power. A downstream device might also experience an increase in small scale turbulence with respect to ambient levels, but this is likely to be of too small a scale to be detrimental.

It is clear that different devices, operating in different conditions, will generate different wake profiles. The wake is dependent on the thrust, and a higher thrust might yield a longer wake, whilst a lower thrust may result in a shorter wake. Within these experiments the contra rotating device produced the highest thrust coefficient, but due to the unique fluid dynamics caused by the dual rotors the discernible wake length was shorter than some other configurations. If a single rotor device were compared with a contra rotating device of equivalent power generation, the contra rotating device would likely have a shorter wake. Thus it appears that contra rotating devices may be used to reduce the length of the wake relative to single rotor equivalent power producing devices.

Laterally staggering the devices, as discussed in Myers *et al.* (2010), would likely facilitate a reduction in the downstream spacing required. However, caution must be taken as wake expansion could result in upstream devices casting a shadow larger than the upstream rotor area, and any potential benefits must be carefully assessed.

8.3 Further Work

8.3.1 Increased Spacial Coverage

A comprehensive CFD analysis of the turbines discussed here would provide a great deal of useful information. It would give greater resolution to the measurement points, allowing a more detailed analysis of boundaries (in particular the rotor edge). It would provide results for areas where physical measurements were limited by physical constraints, such as close to the free surface, or closer than 2 D behind the device. It would also allow an assessment of the turbulence decay, independent of sampling frequency. This would provide information on the magnitude of turbulence due to the wake still present far downstream. However, such a model would be time consuming to build and computationally expensive to run. Furthermore, any computational model would be subject to turbulence assumptions, and meshing restrictions, as mentioned in Section 1.5.

Experimental or computational work which extends beyond 25 D downstream would further clarify the rate of recovery at a distance far downstream.

8.3.2 Alternative Test Environment

Further experimental work could be conducted in a different test environment, which might decouple some of the facility effects from those of the devices. The asymmetry of the flume and its inconsistency over multiple measurement sessions may have shielded some effects from view, and may have distorted others. Further testing in a flume with a more consistent flow profile would augment the results presented here. A variety of ambient turbulence would also have added greatly to the experimental work. However, the limitations of towing (due to downstream coverage) and in sea testing (due to inconsistent, non steady state flow and limited repeatability) make flume tank testing the preferred option for experimental work within the far wake.

8.3.3 More Representative Device or Bigger Scale

Most desirable of all future work would be the wake measurements of a full scale device. This would provide an opportunity to assess the scale dependence of the experiments presented here. Furthermore, a more representative device, for example one with a power take-off system, would be expected in a full scale device, but is not reasonably possible when working at small scales. The in-sea testing of full scale turbines will form an essential part of the development of any device. It is likely these tests will focus on the performance of the device, and the expense associated with full scale testing makes it unlikely that any tests will be conducted with wake data collection as the first priority. Nevertheless wake data could also be captured, and would prove useful for planning array layout.

8.3.4 Near / Far Wake Transition Zone

An unexpected result of this work was the extension of the near wake to 8 D in some cases. A more detailed examination of the transition zone could ascertain where the rotational aspect of the structure is broken down and the far wake begins. Work could also be done to assess what difference the extension of the near wake may make to actuator disc experiments. As was suggested in Section 6.2.4, if velocity measurements were synchronised with blade frequency, the rotation in the wake might be seen even further downstream.

It is possible that the length of the near wake, and position of the transition zone, was influenced by the characteristics of the test facility. Any study similar to this set of experiments could confirm or clarify if the transition zone found in this work was independent of the test facility.

8.3.5 Environmental Impact

The environmental impact of a device will be an important factor in gaining permission to install single devices or arrays. This will be dependent on the environment in which the device is located, however general applications of the results presented here could be used to estimate seabed scouring, impact on bathymetry and impact on ecology of a given location. Further work could be done to assess whether the wake of a contra rotating device would have a different impact to that of a single rotor device, due to the lack of swirl in the near wake.

8.3.6 Array Spacing

Research has been published examining potential efficient layouts of turbines in an array. This depends on certain constraints such as device type; device operation; depth, width and length of channel. Further experimental research is required to fully understand the impact of placing a device in the wake of an upstream turbine. Particular attention should be paid to a device placed in the far downstream wake, beyond 16 D downstream, as this magnitude of distance is likely to be used in arrays where lateral offsetting of turbines is not possible.

The benefits of laterally offsetting any downstream device so as to reduce the impact of the upstream device wake should also be examined.

8.3.7 Contra Rotating Devices

A robust and high resolution computational model of the rotor and near wake of the contra rotating device would prove enlightening. A detailed analysis of the mixing between rotors would give an indication of the wake structure, which in turn would inform wake breakdown. It would also shed light on the deviation from a normal distribution of data sets directly behind the device.

Bibliography

Ainslie, J. (1988). 'Calculating the flowfield in the wake of wind turbines.' *Journal of Wind Engineering and Industrial Aerodynamics*, **27**: pp. 213–224.

Akwesivie, F. (2004). *In the Wake of a Marine Current Turbine.* Master's thesis, University of Strathclyde.

Atlantis-Resources (2018a). 'Ar1500 turbine.' `https://www.atlantisresourcesltd.com/wp/wp-content/uploads/2016/08/AR1500-Brochure-Final-1.pdf`. Accessed: 13-03-2018.

Atlantis-Resources (2018b). 'Meygen project.' `https://www.atlantisresourcesltd.com/projects/meygen/`. Accessed: 24-02-2018.

Bahaj, A. and Myers, L. (2013). 'Shaping array design of marine current energy converters through scaled experimental analysis.' *Energy*, **59**: pp. 83–94.

Bahaj, A.S., Myers, L.E., Thomson, M.D. and Jorge, N. (2007). 'Characterising the wake of horizontal axis marine current turbines.' In 'Proceedings of the 7th European Wave and Tidal Energy Conference (EWTEC2007),' Porto, Portugal.

Bahaj, A., Batten, W. and McCann, G. (2007). 'Experimental verifications of numerical predictions for the hydrodynamic performance of horizontal axis marine current turbines.' *Renewable Energy*, **32**(15): pp. 2479 – 2490. ISSN 0960-1481.

Bai, L., Spence, R.R.G. and Dudziak, G. (2009). 'Investigation of the influence of array arrangement and spacing on tidal energy converter (TEC) performance using a 3-dimensional CFD model.' In 'Proceedings of the 8th European Wave and Tidal Energy Conference (EWTEC2009),' Uppsala, Sweden.

Baidya Roy, S., Pacala, S.W. and Walko, R.L. (2004). 'Can large wind farms affect local meteorology?' *Journal of Geophysical Research*, **109**.

Barthelmie, R.J., Folkerts, L., Ormel, F.T., Sanderhoff, P., Eecen, P.J., Stobbe, O. and Nielsen, M. (2003). 'Offshore wind turbine wakes measured by SODAR.' *Journal of Atmospheric and Oceanic Technology*, **20**: pp. 466–477.

Barthelmie, R.J., Frandsen, S.T., Nielsen, M.N., Pryor, S.C., Rethore, P.E. and Jrgensen, H.E. (2007). 'Modelling and measurements of power losses and turbulence intensity in wind turbine wakes at Middelgrunden offshore wind farm.' *Wind Energy*, **10**: pp. 517–528.

BEIS (2013). 'Wave and tidal energy: part of the uk's energy mix.' Tech. rep., Department for Business, Energy and Industrial Strategy.

Blunden, L. and Bahaj, A. (2007). 'Tidal energy resource assessment for tidal stream generators.' *Proceedings of the Institution of Mechanical Engineers, Part A: Journal of Power and Energy*, **221**(2): pp. 137–146.

Blunden, L.S., Batten, W.M.J., Harrison, M.E. and Bahaj, A.S. (2009). 'Comparison of boundary-layer and field models for simulation of flow through multiple-row tidal fences.' In 'Proceedings of the 8th European Wave and Tidal Energy Conference,' .

Cea, L., Puertas, J. and Pena, L. (2007). 'Velocity measurements on highly turbulent free surface flow using adv.' *Experiments in Fluids*, **42**: pp. 333–348. ISSN 0723-4864. 10.1007/s00348-006-0237-3.

Chanson, H. (2008). 'Acoustic doppler velocimetry (adv) in the field and in laboratory: Practical experiences.' *International Meeting on Measure ments and Hydraulics of Sewers.*

Chen, T. and Liou, L. (2011). 'Blockage corrections in wind tunnel tests of small horizontal-axis wind turbines.' *Experimental Thermal and Fluid Science*, **35**: pp. 565–569.

Chen, Y., Lin, A., Lin, J. and Wang, S. (2017). 'Experimental study of wake structure behind a horizontal axis tidal stream turbine.' *Applied Energy*, **196**: pp. 82 – 96.

Clarke, J., Connor, G., Grant, A. and Johnstone, C. (2007). 'Design and testing of a contra-rotating tidal current turbine.' *Proceedings of the Institution of Mechanical Engineers, Part A: Journal of Power and Energy*, **221**(2): pp. 171–179.

Crespo, A., Hernandez, J. and Frandsen, S. (1999). 'Survey of modelling methods for wind turbine wakes and wind farms.' *Wind Energy*, **2**: pp. 1–24.

Crown Estate, T. (2012). 'Uk wave and tidal key resource areas project summary report.' Tech. rep., ANSYS.

Currie, G., Osbourne, N. and Grouix, D. (2016). 'Numerical modelling of a three-bladed nrel s814 tidal turbine.' In 'Proceedings of the third Asian Wave and Tidal Energy Conference,' .

Daly, T., Myers, L. and Bahaj, A. (2010). 'Experimental analysis of the local flow effects around single row tidal turbine arrays.' In 'Third International Conference and Exhibition on Ocean Energy, Bilbao,,' .

Doman, D., Murray, R., Pegg, M., Gracie, K., Johnstone, C. and Nevalainen, T. (2015). 'Tow-tank testing of a 1/20th scale horizontal axis tidal turbine with uncertainty analysis.' *International Journal of Marine Energy*, **11**(1): pp. 105–119.

Ebdon, T., O'Doherty, D.M., O'Doherty, T. and Mason-Jones, A. (2016). 'Simulating marine current turbine wakes using advanced turbulence models.' In 'Proceedings of the third Asian Wave and Tidal Energy Conference,' .

Ebert, P.R. and Wood, D.H. (1997). 'The near wake of a model horizontal-axis wind turbine I: Experimental arrangements and initial results.' *Renewable Energy*, **12**(3): pp. 225–243.

Ebert, P.R. and Wood, D.H. (1999). 'The near wake of a model horizontal-axis wind turbine II: General features of the three-dimensional flowfield.' *Renewable Energy*, **18**(4): pp. 513–534.

Ebert, P.R. and Wood, D.H. (2001). 'The near wake of a model horizontal-axis wind turbine III: Properties of the tip and hub vortices.' *Renewable Energy*, **22**(4): pp. 461–472.

Fluent-Inc. (2003). *FLUENT Help Guide 6.2.2.*

Fraenkel, P. (2002). 'Power from marine currents.' *Proceedings of the Institution of Mechanical Engineers Part A: Journal of Power and Energy*, **216**.

Frandsen, S. and Thøgersen, M. (1999). 'Integrated fatigue loading for wind turbines in wind farms by combining ambient turbulence and wakes.' *Wind Eng.*, **23**: pp. 327–339.

Frost, C., Morris, C., Mason-Jones, A., O'Doherty, D. and O'Doherty, T. (2014). 'The effect of tidal flow directionality on tidal turbine performance characteristics.' In '3rd Oxford Tidal Energy Workshop,' .

George, W.K. (2013). 'Lectures in turbulence for the 21st century.' URL `www.turbulence-online.com`.

Giles, J., Myers, L., Bahaj, A., O'Nains, J. and Shelmerdine, B. (2011). 'Foundation-based flow acceleration structures for marine current energy converters.' *IET Renewable Power Generation*, **5**: pp. 287–298.

Good, A., Hamill, G., Whittaker, T. and Robinson, D. (2011). 'PIV analysis of the near wake of a tidal turbine.' In 'Proceedings of the Twenty-first International Offshore and Polar Engineering Conference,' .

Hand, M.M., Simms, D.A., Fingersh, L.J., Jager, D.W., Cotrell, J.R., Schreck, S. and Larwood, S.M. (2001). 'Unsteady aerodynamics experiment phase vi: Wind tunnel test configurations and available data campaigns.' Tech. rep., NREL.

Hansen, M.O.L. (2008). *Aerodynamics of Wind Turbines.* Earthscan, London; Sterling, VA, 2nd edn.

Harrison, M.E., Batten, W.M.J., Myers, L.E. and Bahaj, A.S. (2009). 'A comparison between CFD simulations and experiments for predicting the far wake of horizontal axis tidal turbines.' In 'Proceedings of the 8th European Wave and Tidal Energy Conference (EWTEC2009),' Uppsala, Sweden.

Henderson (1966). *Open Channel Flow.* Macmillan.

Kawahashi, H.H.N. (2007). 'The wake structure in a 2d grid installation of the horizontal axis micro wind turbines.' *Renewable Energy*, **13**: pp. 2247–2267.

Lartiga, C. and Crawford, C. (2010). 'Actuator disk modeling in support of tidal turbine rotor testing.' In '3rd International Conference on Ocean Energy,' .

Liu, P. (2010). 'A computational hydrodynamics method for horizontal axis turbine panel method modeling migration from propulsion to turbine energy.' *Energy*, **35**(7): pp. 2843 – 2851. ISSN 0360-5442.

Lohrmann, A., Cabrera, R. and Kraus, N.C. (1994). 'Acoustic-doppler velocimeter (ADV) for laboratory use.' In 'Fundementals and Advancements in Hydraulic Measurements and Experiments,' .

Luke, H.D. (1999). 'The origins of the sampling theorem.' *Institute of Electrical and Electronic Engineers Communications Magazine*.

Maganga, F., Germain, G., King, J., Pinon, G. and Rivoalen, E. (2010a). 'Experimental characterisation of flow effects on marine current turbine behaviour and on its wake properties.' *Renewable Power Generation*, **4**: pp. 498 – 509.

Maganga, F., Pinon, G., Germain, G. and Rivoalen, E. (2010b). 'Wake properties characterisation of marine current turbines.' In '3rd International Conference of Ocean Energy (ICOE),' .

Maganga, F., Pinon, G., Germain, G., Rivoalen, E. and King, J. (2009). 'Experimental study to determine flow characteristic effects on marine current turbine behaviour.' In 'EWTEC 2009,' .

Magnusson, M. (1999). 'Near-wake behaviour of wind turbines.' *Journal of Wind Engineering and Industrial Aerodynamics*, **80**(1-2): pp. 147–167.

Magnusson, M. and Smedman, A.S. (1996). 'Influence of atmospheric stability on wind turbine wakes.' *Wind Energy*, **18**: pp. 139–151.

Malki, R., Masters, I., Williams, A. and Croft, T. (2011). 'The influence of tidal stream turbine spacing on performance.' In 'Proceedings of the 9th European Wave and Tidal Energy Conference (EWTEC2011),' .

Mason-Jones, A., O'Doherty, D., Morris, C., O'Doherty, T., Byrne, C., Prickett, P., Grosvenor, R., Owen, I., Tedds, S. and Poole, R. (2012). 'Non-dimensional scaling of tidal stream turbines.' *Energy*, **44**: pp. 820–829.

Massouh, F. and Dobrev, I. (2007). 'Exploration of the vortex wake behind of wind turbine rotor.' *Journal of Physics: Conference Series*, **75**: p. 012,036 (9pp).

McCombes, T. (2014). *An Unsteady Hydrodynamic Model for Tidal Current Turbines*. Ph.D. thesis, University of Strathclyde.

McCombes, T., Johnstone, C. and Grant, A. (2009). 'Wake modelling for marine current turbines.' In 'Proceedings of the 8th European Wave and Tidal Energy Conference (EWTEC2009),' Uppsala, Sweden.

McCombes, T., Johnstone, C. and Grant, A. (2010). 'Wake modelling for marine current turbines.' In 'Proceedings of the 3rd International Conference on Ocean Energy (ICOE2010),' Bilbao, Spain.

Myers, L. and Bahaj, A. (2005). 'Simulated electrical power potential harnessed by marine current turbine arrays in the alderney race.' *Renewable Energy*, **30**(11): pp. 1713 – 1731. ISSN 0960-1481.

Myers, L. and Bahaj, A. (2006). 'Power output performance characteristics of a horizontal axis marine current turbine.' *Renewable Energy*, **31**(2): pp. 197 – 208. ISSN 0960-1481. Marine Energy.

Myers, L. and Bahaj, A. (2009a). 'Experimental analysis of the flow field around horizontal axis tidal turbines by use of scale mesh disk rotor simulators.' *Ocean Engineering*, **37**: pp. 218–227.

Myers, L. and Bahaj, A. (2009b). 'Near wake properties of horizontal axis marine current turbines.' In 'Proceedings of the 8th European Wave and Tidal Energy Conference (EWTEC2009),' .

Myers, L., Bahaj, A., Retzler, C., Ricci, C. and Dhedin, J.F. (2010). 'Inter-device spacing issues within wave and tidal energy converter arrays.' In '3rd International Conference on Ocean Energy,' .

Myers, L.E., Bahaj, A.S. and Germain, G. (2008). 'Flow boundary interaction effects for marine current energy conversion devices.' In '10th World Renewable Energy Congress,' .

Myers, L., Bahaj, A., Rawlinson-Smith, R. and Thomson, M. (2008). 'The effect of boundary proximity upon the wake structure of horizontal axis marine current turbines.' In 'Proceedings of the ASME 27th International Conference on Offshore Mechanics and Arctic Engineering,' .

Myers, L. (2005). *Operational Parameters of Horizontal Axis Marine Current Turbines*. Ph.D. thesis, University of Southampton.

Nautricity (2018). 'Cormat.' `http://nautricity.com/cormat/`. Accessed: 24-02-2018.

Nikora, V.I. and Goring, D.G. (1998). 'ADV measurements of turbulence: Can we improve their interpretation?' *Journal of Hydraulic Engineering*, pp. 630–634.

O'Doherty, D.M., Mason-Jones, A., O'Doherty, T. and Byrne, C.B. (2009). 'Considerations of improved tidal stream turbine performance using double rows of contra-rotating blades.' In 'Proceedings of the 8th European Wave and Tidal Energy Conference,' .

O'Doherty, D., Mason-Jones, A., Morris, C., O'Doherty, T., Byrne, C., Prickett, P.W. and Grosvenor, R.I. (2011). 'Interaction of marine turbines in close proximity.' In 'Proceedings of the 9th European Wave and Tidal Energy Conference (EWTEC2011),' Southampton, England.

O'Doherty, T., Mason-Jones, A., O'Doherty, D., Evans, P., Wooldridge, C. and

Fryett, I. (2010). ‘Considerations of a horizontal axis tidal turbine.’ *Energy*, **163**: pp. 119–130.

Open-Hydro (2018). ‘Open hydro.’ `http://www.openhydro.com/`. Accessed: 24-02-2018.

Polagye, B.L. (2009). *Hydrodynamic Effects of Kinetic Power Extraction by In-Stream Tidal Turbines*. Ph.D. thesis, University of Washington.

Rethore, P.E. (2009). *Wind Turbine Wake in Atmospheric Turbulence*. Ph.D. thesis, Aalborg University.

Roc, T., Conley, D.C. and Greaves, D. (2010). ‘Accounting for turbulence in a regional numerical model for tidal current turbine farm planning.’ In ‘Third International Conference and Exhibition on Ocean Energy, Bilbao,,’ .

Rose, S., Good, A., Atcheson, M., Hamill, G., Johnstone, C., MacKinnon, P., Robinson, D., Grant, A. and Whittaker, T. (2011). ‘Investigating experimental techniques for measurement of the downstream near wake of a tidal turbine.’ In ‘Proceedings of the 9th European Wave and Tidal Energy Conference,’ .

Sabersky, R.H. (1999). *Fluid flow: A first course in fluid mechanics*. Prentice Hall.

Sanderse, B. (2009). ‘Aerodynamics of wind turbine wakes.’ ECN-E–09-016.

Schenck, H. (1968). *Theories of Engineering Experimentation*. McGraw Hill, New York, 2nd edn.

Schepers, J.G. (2003). ‘Endow: Validation and improvement of ECN’s wake model.’ Tech. rep., ECN-C-03-034.

Schepers, J.G. and Snel, H. (2007). ‘Model experiments in controlled conditions - final report.’ Tech. rep., Energy research Centre of the Netherlands.

Schlichting, H. (1979). *Boundary Layer Theory.* McGraw Hill, New York, 7th edn.

Schreck, S. (2008). ‘IEA Wind Annex XX: HAWT aerodynamics and models from wind tunnel measurements.’ Tech. rep., IEA Wind, NREL.

Scott, A. (2005). *Encyclopedia of Nonlinear Science.* Routledge. ISBN 9781579583859.

Shames, I. (1962). *Mechanics of Fluids.* McGraw Hill.

Smeaton, M., Vennell, R., Harang, A. and Gerritsen, M. (2016). ‘Designing tec arrays in constricted channels.’ In ‘Proceedings of the third Asian Wave and Tidal Energy Conference,’ .

Stallard, T., Collings, R., Feng, T. and Whelan, J. (2013). ‘Interactions between tidal turbine wakes: experimental study of a group of three-bladed rotors.’ *Phil Trans R Soc A*, **371**(20120159).

Stallard, T., Collings, R., Feng, T. and Whelan, J. (2011). ‘Interactions between tidal turbine wakes: experimental study of a group of 3-bladed rotors.’ In ‘Proceedings of 9th European Wave and Tidal Energy Conference (EWTEC2011),’ .

Sun, X.; Bryden, I.J.H.F.D. (2008). ‘An experimental survey in the wake of a simulated tidal current turbine.’ *Journal of Marine Engineering and Technology*, **Vol A12**.

Sun, X., Chick, J. and Bryden, I. (2008). ‘Laboratory-scale simulation of energy extraction from tidal currents.’ *Renewable Energy*, **33**: pp. 1267–1274.

Tennekes, H. and Lumley, J.L. (1972). *A first course in turbulence.* MIT Press, Cambridge, MA. ISBN 9780262200196.

Troldborg, N. (2008). *Actuator Line Modeling of Wind Turbine Wakes.* Ph.D. thesis, DTU-MEK.

Vermeer, L.J., Soerensen, J.N. and Crespo, A. (2003). 'Wind turbine wake aerodynamics.' *Progress in Aerospace Sciences*, **39**(6-7): pp. 467–510.

Vermeulen PEJ, B.P. (1982). 'Turbulence measurements in simulated wind turbine clusters.' Report 82-03003, TNO Division of Technology for Society,.

Voulgaris, G. and Trowbridge, J.H. (1999). 'Evaluation of the acoustic doppler velocimeter (adv) for turbulence measurements.' *Journal of Atmospheric and Ocean Technology*, **15**: pp. 272–289.

Whale, J., Anderson, C.G., Bareiss, R. and Wagner, S. (2000). 'An experimental and numerical study of the vortex structure in the wake of a wind turbine.' *Journal of Wind Engineering and Industrial Aerodynamics*, **84**(1): pp. 1–21.

Whelan, J., Graham, J.M.R. and Peiro, J. (2009). 'A free-surface and blockage correction for tidal turbines.' *J. Fluid Mech.*, **624**: pp. 281–291.

White, F. (1994). *Fluid Mechanics.* Mcgraw-hill Series in Mechanical Engineering. McGraw Hill. ISBN 9780073529349.

Willis, M., Masters, I., Thomas, S., Gallie, R., Loman, J., Cook, A., Ahmadian, R., Falconer, R., Lin, B., Gao, G., Cross, M., Croft, N., Williams, A., Muhasilovic, M., Horsfall, I., Fidler, R., Wooldridge, C., Fryett, I., Evans, P., O'Doherty, T., O'Doherty, D. and Mason-Jones, A. (2010). 'Tidal turbine deployment in the bristol channel: a case study.' *Energy*, **163**: pp. 93–105.

Appendix A

V_Y and V_Z Statistical Plots

The following graphs show the V_Y and V_Z statistical plots for the contra rotating and 2 blade configuration. They correspond to Figures 6.23 and 6.24 found in Chapter 6.

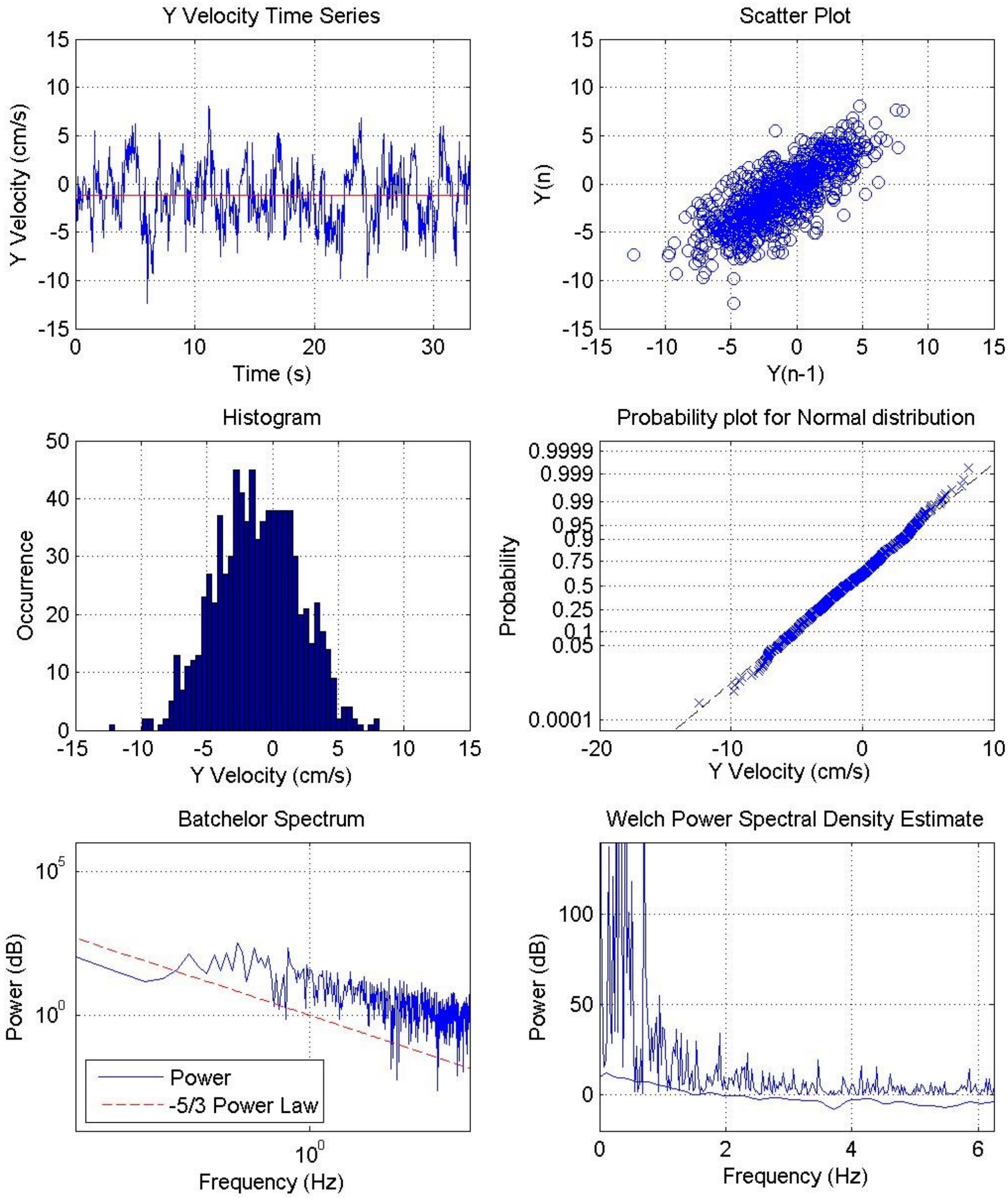

Figure A.1: Statistical plots for V_Y wake data spot reading 2 D downstream of the Contra Rotating configuration

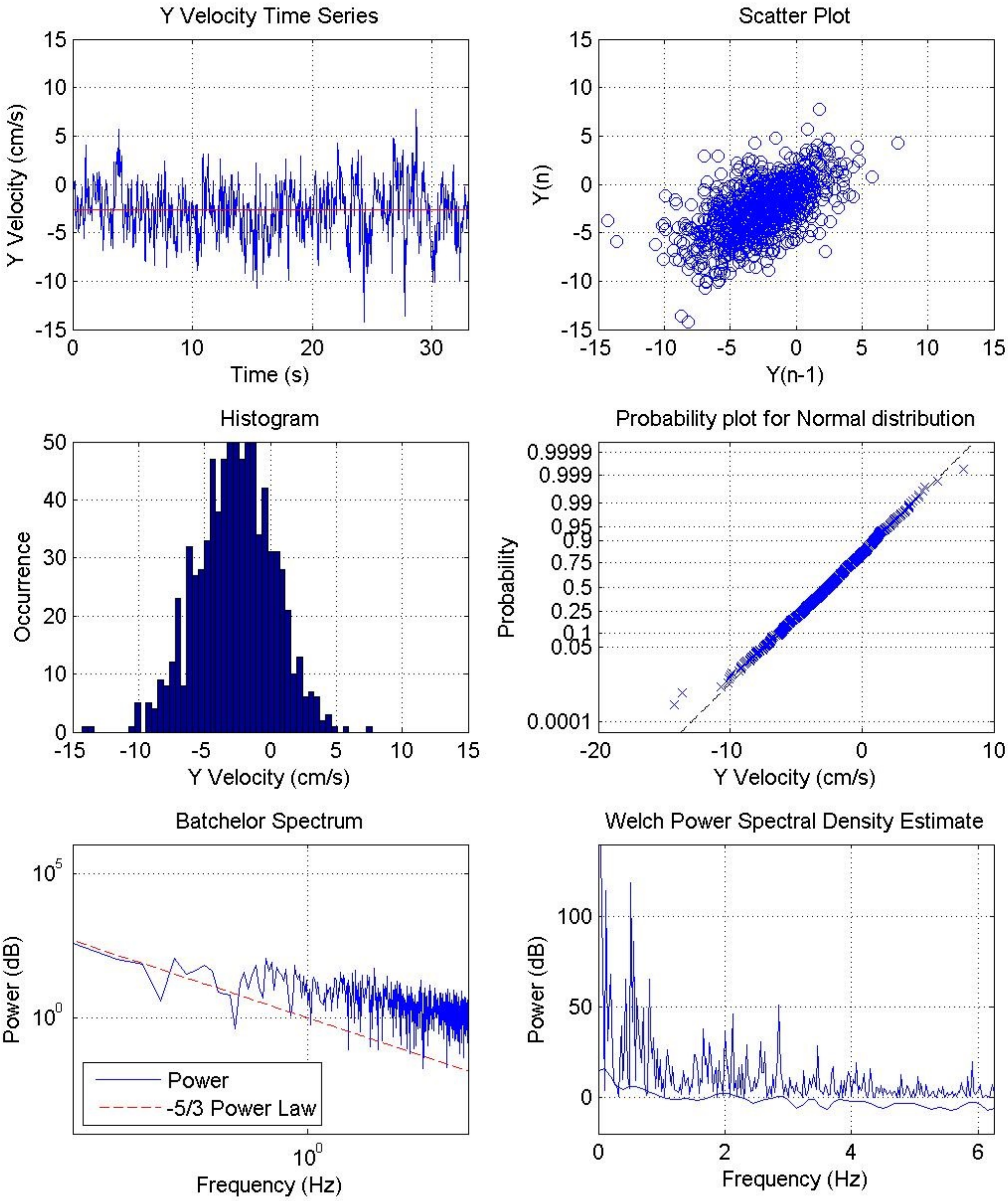

Figure A.2: Statistical plots for V_Y wake data spot reading 2 D downstream of the 2 Blade configuration

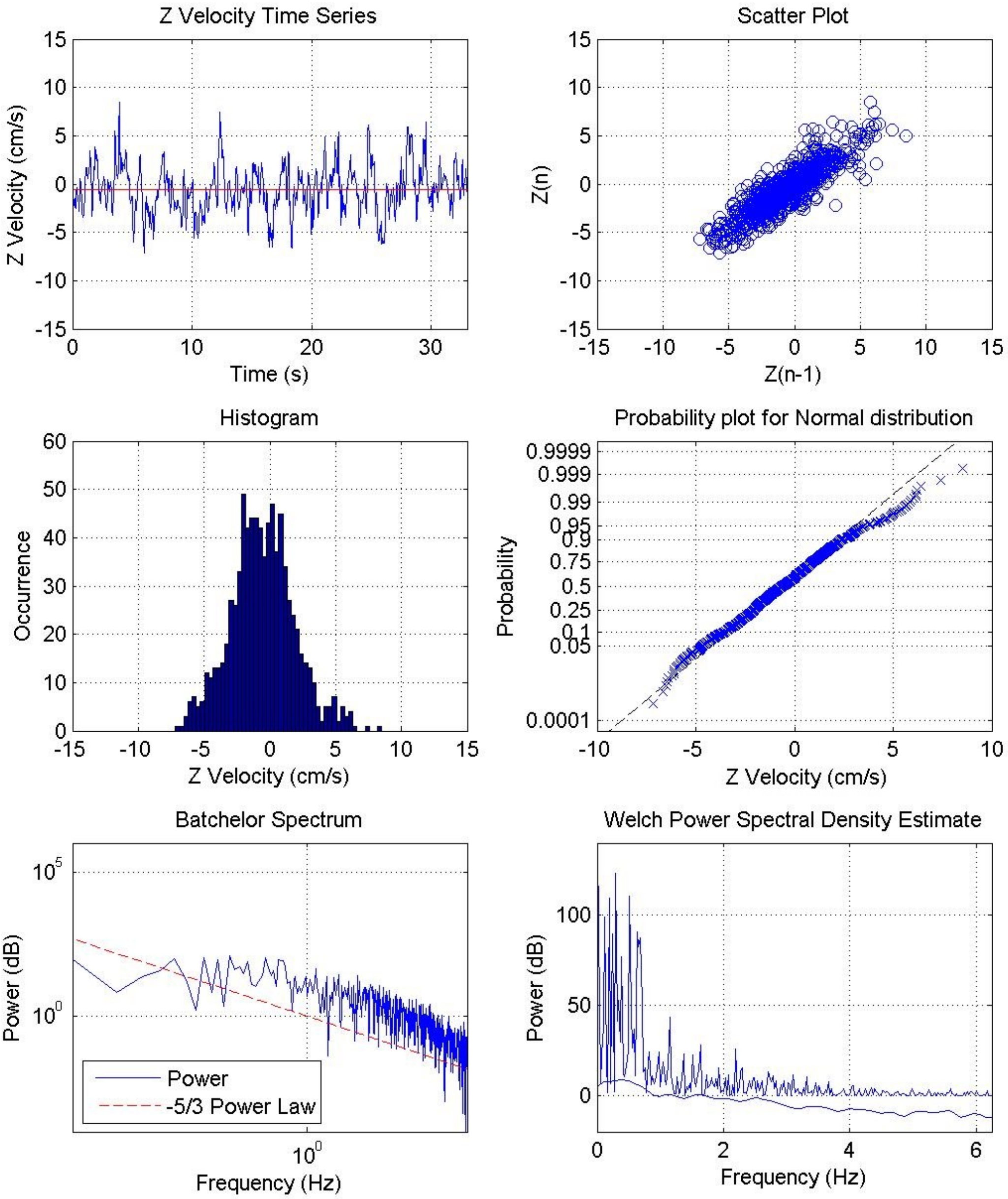

Figure A.3: Statistical plots for V_Z wake data spot reading 2 D downstream of the Contra Rotating configuration

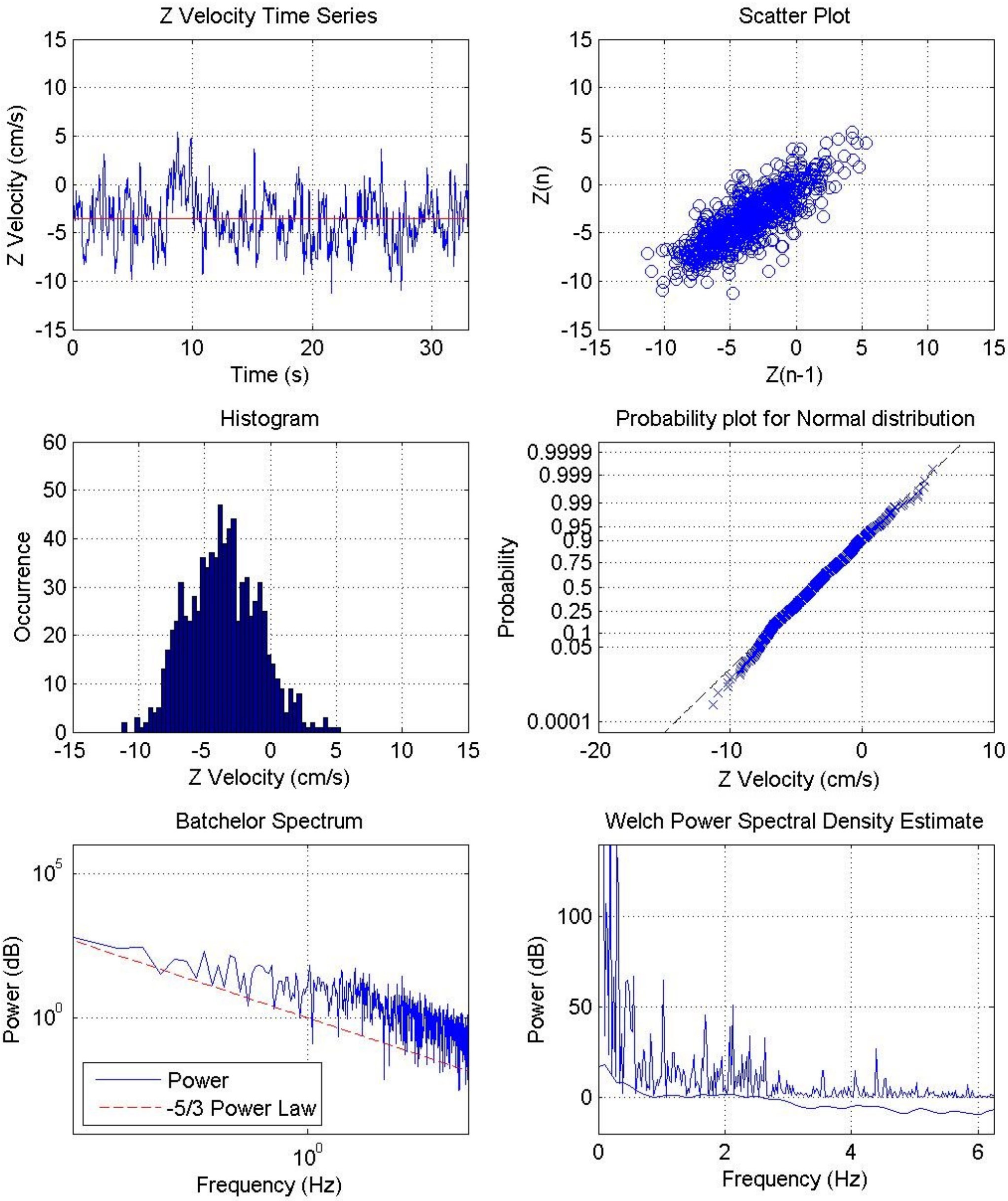

Figure A.4: Statistical plots for V_Z wake data spot reading 2 D downstream of the 2 Blade configuration